



DEPARTMENT OF PHYSICS

TECHNISCHE UNIVERSITÄT MÜNCHEN

Dissertation

**Molecular functionalization of
h-BN**

Domenik Matthias Zimmermann





DEPARTMENT OF PHYSICS

TECHNISCHE UNIVERSITÄT MÜNCHEN

Molecular functionalization of *h*-BN

Vollständiger Abdruck der von der Fakultät für Physik der Technischen Universität München zur Erlangung des akademischen Grades eines Doktors der Naturwissenschaften (Dr. rer. nat.) genehmigten Dissertation.

Author:	Domenik Matthias Zimmermann
Supervisor:	Prof. Dr. Wilhelm Auwärter
Submission Date:	TODO: Submission date
Chairman:	TODO: Chairman
1. Examiner:	TODO: 1. Examiner
2. Examiner:	TODO: 2. Examiner

I assure the single handed composition of this dissertation only supported by declared resources.

Munich, TODO: Submission date

Domenik Matthias Zimmermann

Acknowledgments

Abstract

Contents

Abstract	v
Preface	xvii
1 Introduction	1
2 Experimental methods	3
2.1 Scanning Tunneling Microscopy	3
2.2 Atomic Force Microscopy	9
2.3 X-ray Photoelectron Spectroscopy	12
3 Experimental setup and sample preparation	17
3.1 Experimental setup	17
3.2 Surfaces and ad-layers	19
3.3 Used molecules	32
4 Epitaxial hexagonal boron nitride on copper foils	39
4.1 Pre-treatment of Cu-foils: Polishing	39
4.2 Characterization: SEM & STM of <i>h</i> -BN on Cu-foil	43
4.3 Characterization: XPS of self-grown <i>h</i> -BN/Cu-foils	46
4.4 Characterization: XPS of bought <i>h</i> -BN/Cu-foils	48
4.5 Application: Molecular functionalization with TPCN	50
5 Tert-Butyl-Phenyl Porphine	53
5.1 Single leg functionalization	53
5.2 Double leg functionalization	59
6 Hexabenzocoronene - w/o central borazine core	65
6.1 Find a nice title!	65
7 Unsorted	67
7.1 measurements without clear interpretation	67
Appendix	85

List of Figures

2.1	Operating principles of an STM. (a) A macroscopic sketch shows the central piezo that controls the tip position above the sample. A microscopic sketch shows the tips movement in constant current mode while moving across a atomic step edge. The main piezo is divided in four parts to control movement in the x-y plane and tip-sample distance[142]. (b) The difference between constant current and constant height mode. While the tip follows the samples LDOS in constant current mode (top) the tip height remains constant in constant height mode (bottom)[47].	4
2.2	Energy diagram to visualize the tunneling process between sample (left) and tip (right) separated by a distance d . Work functions of sample and tip (Φ_s and Φ_t) separate the filled states (shaded regions) and the vacuum level (ϵ_{vac}). The sample is lifted by eV after a bias is applied and results in a net electron current from the sample into the tip. One tunneling process is indicated by a wave function in the sample. After overcoming the vacuum barrier its amplitude decreases and the corresponding electron occupies a free state (not shaded) in the tip material. Since sample (ρ_s) and tip DOS (ρ_t) may not be uniform, a fictional DOS is sketched in darker colors between both. Taken from [133]	5
2.3	Photograph (a) and sketch (b) of AFM cantilever as used in the used setup.	10
2.4	Basic function of a typical Q-plus AFM sensor. (a) Sketch of tip-sample interaction together with force-distance graph. The CO functionalization of the metallic AFM tip is shown in (b)	11
2.5	XPS and Auger processes present after irradiation of the sample with X-rays. Two simultaneous processes occur. 2.5(a) shows a scheme of an X-ray gun illuminating a sample area of about 0.4 mm x 0.6 mm. Excited electrons within the first 20 layer escape the sample and are analyzed for their kinetic energy. Core electrons and Auger electrons are excited at the same time resulting in a chemical fingerprint of the sample.	13
3.1	Typical setup for low temperature measurements. A vibration isolated UHV chamber is used to prepare samples and investigate them in a separable chamber with either STM or AFM. A liquid bath cryostat is used to maintain low temperatures. Images stem from diss-knud	18
3.2	Identical crystalline balls in fcc lattice configuration. The surface termination is determined by the direction of the intersecting plane (parallel to the paper plane) relative to the lattice.	20
3.3	Proposed bulk structure of a OFHC copper foil after abrasion with P1200 silicon carbide paper. Adopted from [146]	22
3.4	Experimental setup and voltage characteristic used for electrochemical polishing. 3.4(a) In the process the foil is connected as working electrode (+) and opposed by a counter electrode (-). Material is then transported from the working to the counter electrode resulting in a polished foil surface. 3.4(b) Choosing proper voltage and current values in the polishing plateau is important for good results.	24

3.5	Effect of adding PEG to the etching solution. Interferometric and AFM topography images before and after polishing.	26
3.6	Height profiles and SEM images before and after 1 min electro polishing with a solution reported in [11]. The linear striations, caused by mechanical processing of the copper foil, and the overall roughness of the surface decrease after polishing. Graphene coverage is increased under the same growth conditions, solely through better substrate conditions.	27
3.7	Precursor molecules for <i>h</i> -BN growth. (a) A mixture of ammonia and diborane, (b) ammonia borane, (c) borazine and (d) B-Trichloroborazine, (e) a mixture of decaborane and ammonia. Images reproduced from [1] . .	29
3.8	RT XPS spectra (B1s and Ir4f 7/2) of borazine adsorbed on a Iridium surface held at 170 K and after stepwise annealing to 1370 K. Adopted from [110]	30
3.10	DTF calculation and STM images of <i>h</i> -BN/Ir(111). While being aligned, a lattice mismatch creates a moiré superstructure. It is well visible in adsorption height calculations 3.10(a) and as apparent height differences in STM images 3.10(b).	31
3.9	Adopted from [63]	31
3.11	Work function variation along <i>h</i> -BN/Cu(111) moiré. (a) STM image showing the <i>h</i> -BN moiré with a periodicity of 8.4 nm. Scan parameter: $U_b = 4.0V, I_t = 40pA$. (b) Field emission resonances acquired along the black dotted line in a) revealing a variation of the peak positions. (c) Work function differences between bright (“hill”/pore) and dark (“valley”/wire) regions obtained from the dI/dV curves of the field emission resonances displayed in b). Adopted from [135]	32
3.12	Functionalized tert-butyl-phenyl-porphines. (a) shows a single functionalized porphine molecules. An additional function may be added in (c) cis- and (b) position.	34
3.13	Pyridyl-Pyrene molecules in trans- (b) and cis- (c) and tetra- (a) configuration	35
3.14	DCDB on copper surface. (a) Top view, (b) side view	35
3.15	(a) HBBNC and (b) HBC	36
3.16	Sketch of how to determine the distance between two molecules. As the molecule is square (with the exception of one direction, one can determine the center of the molecule by comparing two 90 degree rotated profiles. Profile 1 goes through the symmetry axis, while profile 2 and 3 intersect profile 1 at the center. As the profile 2 and 3 look the same when starting at the butyl groups, one can use the depression in profile 2 and 3 to determine the center of the molecule in profile 1.	37
4.1	SEM image of etched copper foil. Different contrast suggests different grain-orientation within the surface. a) Larger (570 μm x 380 μm) image showing the contrast of different grains in the copper-foil, b) zoom (18 μm x 12 μm)	41
4.2	SEM image that shows different surface morphologies (5.6 μm x3.7 μm) . .	42
4.3	AFM image of the 0.25 mm copper foil as bought from alfa aesar.	42
4.4	AFM image of a copper foil polished 5h (according to table 3.5)	43
4.5	Cu-foil after repeated sputtering and annealing cycles (a) and after CVD growth of a sub-ML <i>h</i> -BN (b). Imaging parameters: (a) 3.6 V, 0.1 nA, color scale 0 pm to 600 pm, Image width: 88.6 nm, (b) 1 V, 0.37 nA, color scale 0 pm to 900 pm, Image width: 44.3 nm.	44

4.6 STM image of 22L borazine dosed on a 800 °C hot copper-foil surface. Several large islands can be seen that grow over Cu-foil step edges. Inset shows coverage with <i>h</i> -BN ad layer in blue. Imaging parameters: 4.7 V, 0.2 nA, color scale 0 nm to 7 nm, Image width: 295 nm.	45
4.7 STM topographies of <i>h</i> -BN islands that overgrow Cu-foil facets. Imaging parameters: (a) 1 V, 0.37 nA, color scale 0 nm to 1.5 nm, Image width: 18 nm, (b) 3.5 V, 0.5 nA, color scale 0 nm to 4 nm, Image width: 73.8 nm.	45
4.8 funny surface structure - oxygen over layer (2x1)?- cu reconstruction? - maybe some very small (0.75 nm) linear moire on a Cu(100) facet? Noise can be excluded due to the fact that the stripes do not occur on the molecules, but only on the substrate. Many deformed molecular cores visible → strong substrate interaction → no <i>h</i> -BN! Line spectrum shown in ?? Imaging parameters: (a) 1.26 V, 0.04 nA, color scale 0 nm to 0.8 nm, Image width: 40 nm	46
4.9 REDO! Axis too small!! Check layout with other XPS measurements!! XPS spectra for ML <i>h</i> -BN/Cu-foil. The peaks are at their expected positions[78] and show no additional features. No remnants of sulfur or remaining oxygen could be found.	47
4.10 XPS spectra of as-bought <i>h</i> -BN/Cu-foil sample[52]. All spectra are taken at room temperature in as-bought state (black) and after annealing to 630 K (blue) and 970 K (red).	49
4.11 Position change of TPCN group members. Central molecule is manipulated, color indicates its initial (a, green hue in c) and final (b, red hue in c) position. Image (c) is created via an overlay of two sequential images. The upper and lower molecules do not shift thus sharing the same color.	50
4.12 There they form a motiv like in figure 4.11a).	51
4.13 Self-Assembled monolayer for TPCN on h-BN/Cu-foil. The cobald atoms sit right in between the molecules and faciliate a regular, ordered arrangement of the TPCN.	52
 5.1 TBP with three di-tert-butyl and a single nitro phenyl group added at the meso position.	53
5.2 RT adsorbed single nitro functionalized TBP on Cu(111) and their most abundant binding motifs. (a) Each of the binding motif can be found as well in the overview STM data, as well as in the enlarged images (b-d). All images recorded with -500 mV, 0.1 nA, color scale 0 pm to 300 pm. Image width: (a) 44 nm, (b) 3 nm, (c) & (d) 5 nm	55
5.3 Different appearances of TBP on Cu(111). While most of monomers (center in image above) show even heights with their tert-butyl functions, some (left) do posses an elevated tert-butyl group. The orientation of the tert-butyl groups is aligned with the high symmetry crystal direction (indicated by white lines) most often. Image recorded with -500 mV, 0.1 nA. Image width: 10 nm	56
5.4 Annealing after RT adsorption of molecules on Ag(100). (a) STM data of molecules adsorbed at RT (Scan parameters: $U_b = 1$ V, $I_t = 0.03$ nA), (b) After annealing for 10 min to 170 °C (Scan parameters: $U_b = 1$ V, $I_t = 0.1$ nA). Color scale 0 pm to 600 pm. Image width: 44 nm.	56

5.5	Different observed binding configurations of TBP adsorbed on Ag(100) at RT. (a) STM data of dimer configuration. Scan parameters: $U_b = 0.328\text{ V}$, $I_t = 0.035\text{ nA}$, Image width: 5 nm. (d) Model representation. (b) STM data of two coalescent dimers. Scan parameters: $U_b = 0.097\text{ V}$, $I_t = 0.035\text{ nA}$, Image width: 6 nm. (e) Model representation. (c) A cross consisting of four TBP molecules. Scan parameters: $U_b = 2.3\text{ V}$, $I_t = 0.035\text{ nA}$, Image width: 10 nm. (f) Model representation. Color scale in all STM images 0 pm to 300 pm	57
5.6	STM topographs of <i>h</i> -BN grown on copper with subsequent molecular adsorption. (a) shows a <i>h</i> -BN layer grown on Cu(111) by CVD. (b) shows the sample after evaporating TBP molecules at RT. (c) shows empty <i>h</i> -BN islands grown on the polycrystalline copper foil and molecules on a copper terrace. Scan parameters: (a) $U_b = 2.273\text{ V}$, $I_t = 0.048\text{ nA}$, color scale 0 pm to 100 pm. (b) $U_b = 1.074\text{ V}$, $I_t = 0.033\text{ nA}$, color scale 0 pm to 300 pm. (c) $U_b = 2.585\text{ V}$, $I_t = 0.032\text{ nA}$, color scale 0 pm to 1500 pm. All images are 40 nm wide.	58
5.7	Molecules adsorbed on Cu(111) at RT and subsequently annealed to different temperatures. (a) Adsorption at room temperature did not show extended long range order. (b) Adsorption at 70 °C and (c) annealing to 170 °C for 10 min improves the chain length slightly. All images are 40 nm wide. Scan parameters: (a) $U_b = 1.2\text{ V}$, $I_t = 0.041\text{ nA}$, (b) $U_b = 0.5\text{ V}$, $I_t = 0.038\text{ nA}$, (c) $U_b = 0.522\text{ V}$, $I_t = 0.021\text{ nA}$	59
5.8	All motifs exist at every temperature, although the chain length increases with temperature. It also looks like the chains are getting more offset- and kinked-like chains than at lower temperatures.	60
5.9	Straight chain binding motif on Cu(111). (a) shows an STM image together with the dense packed row indication of the substrate (white lines). Colored bars indicate the rotation of the di-tert-butyl-groups. Arrows point at places where ad-atoms are considered. (b) Top views (6 nm wide) showing the molecules geometry in gas-phase (left) and after adsorption and assembly (right). Although the exact adsorption site is not known, it is considered to be on a bridge site as for 2H-P/Cu(111). (c) Side views of above shown configurations.	61
5.10	Trans-TBP adsorbed on Ag(100) at room temperature. (a) shows a large overview of the assembled molecules. The unit cell constituents are enlarged in (b) where parts of (a) are shown with molecular models overlaid. (c) shows a single molecule crossing a horizontal plain to emphasize high lying part in the molecule that are marked with white circles and will appear brighter in STM. All images recorded with 437 mV, 0.1 nA, color scale 0 pm to 650 pm	63
5.11	Domain boundary of trans-TBP adsorbed on Ag(100) at RT. (a) shows an overview of the domain boundary together with its model representation in (b). The assembly close by is modeled in (c) where parts of (a) are shown and molecular models overlaid. All images recorded with 1.3 V, 0.1 nA, color scale 0 pm to 650 pm	64
1	TBP on Ag(100) showing some ordering	87

2	Symmetry relations between TBP molecule and Ag(100) crystal substrate. The same molecular model is highlighted in two different ways, emphasizing the two molecular axis (red/blue). Since the assembly is made up of three different orientations, the three rotated axis sets are shown. The assemblies derived unit cell is shown as shaded background with short and long symmetry axis highlighted in green. The crystal orientation from another preparation on the same single crystal is shown in grey.	88
3	EHT calculated molecular orbitals. HOMO and LUMO states together with five neighboring states (shown in the same column). Inner two columns show HOMO & LUMO states. Outer columns show integration of states as STM image estimation if all states to E_F were contributing equally. Images are 2.5 nm wide	89
4	EHT calculated molecular orbitals. HOMO and LUMO states together with five neighboring states (shown in the same column). Inner two columns show HOMO & LUMO states. Outer columns show integration of states as STM image estimation if all states to E_F were contributing equally. Images are 2.5 nm wide	90
5	EHT calculated molecular orbitals. HOMO and LUMO states together with five neighboring states (shown in the same column). Inner two columns show HOMO & LUMO states. Outer columns show integration of states as STM image estimation if all states to E_F were contributing equally. . .	91
6	EHT calculated molecular orbitals. HOMO and LUMO states together with five neighboring states (shown in the same column). Inner two columns show HOMO & LUMO states. Outer columns show integration of states as STM image estimation if all states to E_F were contributing equally. . .	92

List of Tables

2.1	Energy and line widths of available anode materials. Taken from	12
2.2	Element specific transitions and binding energies for some chosen elements as reported in [150]	14
2.3	Spin-orbit splitting parameters. Ratios are reproduced from [122]	14
2.4	Description of parameters used in equation 2.6	15
3.1	Inter atomic distances for Cu and Ag with respect to different surface termination. a denotes the lattice constant and $\beta = 60^\circ$ the angle within the (111) unit cell	19
3.2	Crystal properties from [92, 97, 121, 29ff]	20
3.3	Table with some of the found etching recipes.	25
3.4	Used etching solutions (compare [70, p. 130]). Note the change in the removal rate due to higher limiting currents in the solution after adding ethylene-glycol to the solution.	28
3.5	Volume and mass fractions for copper foil etching solution.	28
3.6	Lattice mismatches between <i>h</i> -BN and several transition metal surfaces. The mismatch is given to describe the relative size of the h-BN layer compared to the substrate, e.g. negative values indicate a larger lattice constant in the substrate bulk.	32
3.7	Evaporation and degas temperatures used for different molecules.	35
4.1	Determination of the full monolayer borazine dosage. First a certainly saturated sample was prepared (I) and measured in XPS/STM. A sub-monolayer (II) was grown and compared to the monolayer STM and XPS results.	47

Preface

- Science is a tool to increase knowledge
 - academic examples
- Science has made life easier in lots of areas
 - examples
- Without translation of fundamental science none of the above mentioned features would be implemented in every day life
 - examples of failed translations

1 Introduction

This is the introduction..... write some! :D

2 Experimental methods

Several experimental methods are used within this work to determine different physical properties. In this chapter we review the principles, benefits and limitations for each method. All of them are well known in surface science and used to analyze thin films on different substrates with respect to their geometric, electronic and chemical properties.

2.1 Scanning Tunneling Microscopy

A widely used surface sensitive method is the scanning tunneling microscopy (STM). It is used to investigate as well the topography of the sample, as its electronic configuration by utilizing the quantum mechanical tunneling effect. STM has a big advantage compared to space averaging, surface sensitive techniques like XPS and LEED because it offers information in the order of atomic radii. With the help of STM the reconstructed surface of Si(111) was first discovered [13] in 1983 and described on the atomic scale.

Because a wave function of an electron does not strictly end within the sample, parts of the electronic wave function spill into the surrounding vacuum. If another material (STM tip) is in close proximity, sample electrons can overcome the vacuum gap into the tip - a process known as tunneling. Two major factors determine the tunneling current: The voltage applied between tip (grounded) and sample (bias) and the tip-sample distance. Assuming the two materials are the same, the created, time averaged current is zero because the same amount of electrons tunnel in either direction. If a bias is applied across the vacuum gap, the current in one direction becomes non-zero. The bias may be changed and switched in polarity, causing electrons to originate from either the tip or the sample. This enables detection of occupied (negative bias) and unoccupied (positive bias) states in the sample. The distance between tip and sample influences the amount of electrons that are able to tunnel and gives rise to the resolution of geometric details in STM images. With a constant bias the current is related to the distance between tip and the (homogeneous) sample.

The position of the tip (x , y , z) is controlled with a set of piezos (see Figure 2.1(a)). In this work a tubular piezo stack is used to control the tips position with a central piezo element located on top of the tungsten tip. The piezo length can be controlled with the voltage applied to them, which is used to choose not only the tip-sample distance, but other parameters like image size and scan speed as well. All of these parameters are monitored with the STM software. A feedback loop controls the piezo voltages. For recording an image the area is raster scanned in consecutive lines, applying a sawtooth voltage to the fast scan direction. The next lines are chosen by slowly increasing the voltage along the slow scan direction. Depending on the operating mode the tip-sample distance is controlled by piezo elements, too.

There are two common ways to operate an STM as shown in Figure 2.1(b). The **constant current mode** is the most widely used one. The tip height is regulated with a feedback controller to achieve a constant tunneling current for the chosen bias. The recorded information is now the voltage applied to the z-piezo to maintain a plane with the same current. Sample features that increase the tunneling current cause the feedback to decrease it again by retracting the tip. In **constant height mode** the tip has always

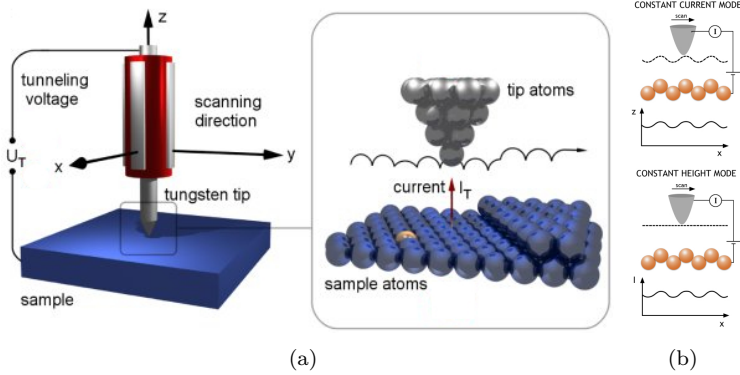


Figure 2.1: Operating principles of an STM. (a) A macroscopic sketch shows the central piezo that controls the tip position above the sample. A microscopic sketch shows the tips movement in constant current mode while moving across a atomic step edge. The main piezo is divided in four parts to control movement in the x - y plane and tip-sample distance[142]. (b) The difference between constant current and constant height mode. While the tip follows the samples LDOS in constant current mode (top) the tip height remains constant in constant height mode (bottom)[47].

the same absolute height (no feedback control), but as the tip-sample distance changes the tunneling current varies, which then is the measured quantity. To avoid crashes when the sample is very irregular, many STM's are operated in constant current mode. Typical tunneling currents are in the range of 0.01 nA to 100 nA where the applied voltage may range from 0.01 V to 10 V. All STM images in this work are recorded in constant current mode. The current recorded in a certain area of the sample is translated into a contrast variation on a color scale. While some images encourage the operator to interpret points with high intensity as elevated atoms it is not that trivial. Tunneling current between tip and sample depends on the LDOS of tip and surface and is therefore not implicitly maximized at the atomic positions. It may also vary with the bias voltage applied in a non-trivial manner. Investigation of this behavior led to the establishment of a new measurement technique, called scanning tunneling spectroscopy (see subsection 2.1.1).

Although sensible to electronic changes, STM may change the print of an adsorbed compound [127]. When laterally approaching an adsorbate this results in an additional tunneling current, because now electrons do not only tunnel directly into the substrate but through the adsorbate as well. Interferences between both tunneling processes depend on the adsorbate's orbital-symmetry and tip-shape. Local density of states calculations [42, 85, 141] is not adapted to grasp this effect since the tip is considered far away from the surface. Moreover, the tip radius or the tip-substrate distance is optimized to fit the lateral size of the adsorbate print with the experimental image [eigler_imaging_1991 , 141].

While the tip (metal) is far away from the sample, their vacuum levels are supposed to be the same. The corresponding Fermi energies of sample and tip lie below the vacuum level by the amount of their work functions (Φ_s and Φ_t for sample and tip respectively). Wave functions of electrons within the solids decay exponentially in vacuum, depended on their energy with respect to the Fermi level. If sample and tip are in thermodynamic equilibrium, their Fermi levels are the same. Electrons now face a potential barrier

(approximately rectangular) which can be overcome if their energy is high enough and the barrier sufficiently narrow. When a voltage is applied across the tunneling barrier, the energy of the tip-electrons is shifted by eV as illustrated in Figure 2.2. When a positive bias voltage is applied, electrons tunnel from the tip into unoccupied states in the sample - a negative bias results in a tunneling current in opposite direction.

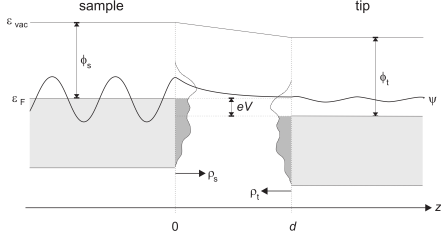


Figure 2.2: Energy diagram to visualize the tunneling process between sample (left) and tip (right) separated by a distance d . Work functions of sample and tip (Φ_s and Φ_t) separate the filled states (shaded regions) and the vacuum level (ϵ_{vac}). The sample is lifted by eV after a bias is applied and results in a net electron current from the sample into the tip. One tunneling process is indicated by a wave function in the sample. After overcoming the vacuum barrier its amplitude decreases and the corresponding electron occupies a free state (not shaded) in the tip material. Since sample (ρ_s) and tip DOS (ρ_t) may not be uniform, a fictional DOS is sketched in darker colors between both. Taken from [133]

Following the model of Tersoff-Hamann¹((1) uniform density of states in the tip, (2) temperature is low, (3) small bias voltage of some mV, (4) waveform of electrons in tip are s-waves) the tunneling current results to

$$I = 32\pi^3 \hbar^{-1} e^2 V \Phi^2 R^2 \kappa^{-4} e^{2\pi R} D_1(E_F) \rho_s(r_o, E_F)$$

where D_1 is the density of states per unit volume of the tip, R the tip radius and $\rho_s(r_o, E_F)$ the Fermi level density of states in the sample[14]. The distance between tip and sample is denoted as Z and the inverse decay length of the electrons wave function is κ . If I is held constant one can see that the tip in principle follows a contour of constant Fermi level density of states at the sample surface, measured at the center of the curvature of the s-wave like tip. While its a good first approximation of the system, in many cases the bias is much higher than 10mV (1 V to 5 V) so more than just the electrons near Fermi contribute. Also a uniform ρ_t may not be accurate in all cases.

Using WKB theory[17, 82, 151] the tunneling current is given by

$$I = \int_0^{eV} \rho_s(r, E) \rho_t(r, eV + E) T(E, eV, r) dE \quad (2.1)$$

where $\rho_s(\rho_t)$ is the density of states of the sample (tip) and T is the tunneling transmission probability

$$T(E, eV) = \exp \left(-\frac{2Z\sqrt{2m}}{\hbar} \sqrt{\frac{\Phi_s + \Phi_t}{2} + \frac{eV}{2} - E} \right) \quad (2.2)$$

¹Please note that there are more models and corrections to them. An evolution from Bardeen's approach to the one done by Tersoff-Hamann can be found here [wortmann_interpretation_200, 94] including Chen's expansion.

If $eV < 0$ the tunneling current is largest for $E = 0$ (electrons on the Fermi-level of the sample), if $eV > 0$ the tunneling current is largest for $E = eV$ (electrons of Fermi level in tip).

Due to the fact that the tunneling current is proportional the density of states in the tip AND the molecule one can deduce the band structure within a range of several volts in the vicinity of the Fermi energy.

Since states with highest energy have the largest decay lengths in vacuum, most of the tunneling current is determined by electrons within close proximity to the Fermi level.²

The accuracy of a STM is very high with spatial resolution down to the atomic scale. Due to the fact that the tips motion is controlled with different piezos, one has to take different elongations in different directions into account. For example, if the STM scans the fast scanning direction just a bit further than the slow scan direction, the resulting image (although pixel wise square) is no longer physically square anymore. Imagine a square (1:1 side ratio, diagonal angle 45°) where one side is elongated by 5%. The resulting square (1:1.05 side ratio, diagonal angle 43.6°) looks square because it has the equal number of pixels in both directions, but it is physically rectangular. The expression used to calculate the uncertainty with known calibration parameters is

$$\Delta\Theta = 45 - \frac{180}{\pi} \cdot \arctan\left(\frac{1}{1+x}\right)$$

where x is the percentage of one side being longer. This results in an uncertainty of 0.3°(1%), 1.4°(5%, see example above), 2.7°(10%). For moderate shear, conformity is almost conserved and the uncertainty below 2°.

2.1.1 Scanning Tunneling Spectroscopy

First changes of the tunneling current with the bias voltage were observed by Tromp et al. in 1986 [145]. They discovered a change in contrast when scanning a Si(111) surface with either positive or negative bias. The change in contrast is most apparent in semiconductors and semi metals[14], but adsorbates and charged areas of the sample change the DOS locally and therefore the contrast in STM. While simple results may be already obtained when comparing two images recorded at different voltages, more detailed information can be achieved. At low temperatures the vanishing lateral movement of molecules makes them also accessible to tunneling spectroscopy. It is possible to deduce the electronic configuration on with atomic spatial resolution.

Spectroscopic information (information on the DOS) can be obtained by either changing the bias voltage ($I(V,z)$ -spectroscopy) or the tip-sample distance ($V(z)$ -spectroscopy).

Therefore the bias is modulated with a sinus like waveform. The frequency of the low amplitude modulation of the DC bias is much larger than the feedback loop frequency (1 kHz to 2 kHz). The AC part of the tunneling signal is than recorded with a lock in amplifier. The in-phase component is directly the $dI/dV|_{V=V_{bias}}$, recorded simultaneously with the topography.³

First let us consider small biases. If tunneling conditions are such that $eV \leq \Phi$, observed features in dI/dV are associated with the surface DOS. Critical points in the surface projected DOS give rise to features in dI/dV . Interpretation of these features with the

²More information related to tunneling processes can be found here [14].

³If the modulation frequency is too low, the feedback tries to compensate the modulation by changing the distance to the sample. If the modulation frequency is too high, the capacitance between tip and sample leads to an 90 deg phase shifted current which increases with modulation frequency. One usually chooses the modulation frequency slightly above the cutoff frequency for the feedback loop.

WKB theory (i.e. differentiating equation (2.1)) gives

$$dI/dV = \rho_s(r, eV)\rho_t(r, 0)T(eV, eV, r) + \int_0^{eV} \rho_s(eV)\rho_t(r, E - eV) \frac{dT(E, eV, r)}{dV} dE$$

The first term contains the DOS of the sample and tip and the transmission function. While it is usually unknown, a closer look to (2.2) indicates a smooth, monotonically increasing function in V. This mannered dependence on V gives a smooth background described by the second term $\int_0^{eV} \rho_s(eV)\rho_t(r, E - eV) \frac{dT(E, eV, r)}{dV} dE$. Because T is smooth and monotonic the first term $\rho_s(r, eV)\rho_t(r, 0)T(eV, eV, r)$ introduces the dependence on the DOS in the sample for energies eV - our desired spectrum.

If dI/dV is recorded simultaneously with the topography, another contribution arises. One usually observes an decrease in atomic corrugation when the distance between tip and sample is increased. The surface looks flat. To have the same tunneling current on atom positions and in between, the decay length in the valleys κ_v must be larger than on the atom positions κ_a . The Z-depended corrugation given by Tersoff-Hamann is

$$\Delta(Z) \approx \frac{2}{\kappa} e^{-\frac{\pi^2 Z}{a^2 \kappa}}$$

where a is the lattice constant and κ the inverse decay length. To make both a flat looking surface one gets the expression

$$\kappa_v = \kappa_a - \frac{2\pi^2}{\kappa a^2} e^{-\frac{\pi^2 Z}{a^2 \kappa}}$$

As the transmission factor changes with the decay length, the tunneling current and with it the dI/dV changes. This is the origin of topographic features in dI/dV maps when recorded at constant current.

The origin of the strongly voltage depended background can be found in WKB theory as well. When writing the tunneling current as

$$I = \int_0^{eV} \rho_s(r, E)\rho_t(r, eV + E) \exp\left(-\frac{2Z\sqrt{2m}}{\hbar} \sqrt{\frac{\Phi_s + \Phi_t}{2} + \frac{eV}{2} - E}\right) dE$$

the tunneling current reduces to

$$\bar{I} = \rho_s \rho_t \bar{V} \exp\left(-\frac{2\sqrt{2m}}{\hbar} \sqrt{\Phi} Z\right) \quad (2.3)$$

Assuming that DOS of tip and sample ρ_t/ρ_s are constant, as well as discarding the change of the tunneling barrier with the bias voltage(an assumption only valid for very small voltages with $eV \ll \Phi$) the derivative of (2.3) is given by

$$\frac{dI}{dV} = e\rho_s \rho_t \exp\left(-\frac{2\sqrt{2m}}{\hbar} \sqrt{\Phi - \frac{eV}{2}} Z\right)$$

Substituting Z with the one obtained by (2.3) leads to $dI/dV = \bar{I}/\bar{V}$ - which diverges as $1/V$ when going to very low bias voltages and gives another contribution to the background. This makes it hard to observe features in close proximity to the fermi level ($V_{bias} = 0$ V). This background can be reduced when operating at constant tunneling

resistance and not at constant current. When doing this, features usually obscured by the $1/V$ diverging background can be observed.⁴

If the bias voltage is higher than the work function of the sample dI/dV reflects mainly states that arise from interaction of electrons at the surface with the polarization they induce in the bulk. Electrons are trapped by this interaction in a region near the surface leaving their lateral movement undistorted. These waves either do interfere con- or deconstructively at the surface. Which type of interference occurs is determined by the applied bias voltage that alternates the bounding condition. The transmission alternates when going from constructive to destructive interference and therefore the tunneling current changes when changing V. As an interesting fact, Becker et al.[10] found that that numerical integration of Schrödinger's equation could be used together with dI/dV spectra to calculate the absolute distance between tip and sample - a value hard to come by with other methods.

Further information can be drawn from the tunneling system when the barrier height may be determined. Taking the limit of the transmission function (2.2) for low bias voltage ($eV \approx 0$, $E = E_F$) results in

$$T = \exp\left(-\frac{2Z\sqrt{2m}}{\hbar}\sqrt{\frac{\Phi_s + \Phi_t}{2}}\right)$$

Using this in the WKB approximation (2.1), one gets

$$\frac{dI/dZ}{I} = \frac{2\sqrt{2m}}{\hbar}\sqrt{\Phi_s + \Phi_t}$$

As the work function of the tip usually stays constant, lateral variations in the barrier height can be boiled down to local changes in the work function. This is done by [68].

Determining the barrier height in this way often results in too low values for the work function. Discussion of this is found in [14, p. 96].

Up to now only rectangular tunneling barriers were considered. Already in 1966 Gundlach was the first who calculated transmission currents for trapezoidal potential barriers [54]. The oscillations named after him are due to standing wave states in the potential tip-sample potential barrier [10, 12]

"When the Fermi level of the tip is close to the vacuum level of the sample, the contribution of the image potential is significant. The superposition of the image potential and the electrostatic potential forms a specific potential well, and the lowest-order peak is a Gundlach oscillation related to a standing-wave state in this well. When the Fermi level of the tip is higher than the vacuum level of the sample, the image potential becomes negligible, and the potential well can be approximated by a triangular shape. Those peaks beyond the lowest-order peak are the Gundlach oscillations related to the standing-wave states in the triangular well. Derivation based on quantum mechanics shows that the energy difference of the standing-wave states in the triangular well is proportional to $F^{2/3}$, where F is the electric field in the tip-sample gap"[91]

The resolution of STS is determined by the range of energies electrons have when contributing to the tunneling process. When $T > 0$ the DOS is smeared out and described by the Fermi-Dirac statistic[36, 46]

$$f(E) = \frac{1}{1 + \exp\left(\frac{E-E_F}{k_B T}\right)}$$

⁴A comprehensive overview on measurement technique and analysis can be found in [14]. For information on normalization of STS and to reduce the background close to E_F , see [44].

Since electrons from occupied states (DOS is Fermi distributed) tunnel into unoccupied states the transmission function has the structure

$$T(E, eV, T) = T(E, eV)f(E)[1 - f(eV - E)]$$

When looking at the shape of the Fermi-Dirac distribution one can see that most of the electrons participating in the tunneling process arise from a rather narrow area around the Fermi level of the negatively biased electrode (broadening of fermi edge at $T = 300K \hat{=} 0.026\text{ eV}$). Electron distribution of tip and sample are broadened by $2k_bT = 0.054\text{ eV}$ thus the energetic range where electrons may come from is 0.1 eV . From the uncertainty relation $\Delta x \Delta k \geq 1/2$ and the dispersion relation for metals follows

$$\Delta E \geq \frac{\hbar^2 k_F}{2M^* \Delta x} = 0.47 \frac{E_F - E_0}{r k_F}$$

[24]. “The asymmetric form of $T(E, eV)$, with the sharp increase at E_F , helps to make the effective resolution of the STM somewhat higher when probing empty states of the sample than when probing filled states.” The resolution at room temperature is estimated to be 140 m eV [57]. As the tunneling transmission is always a factor of the tip and sample DOS, STS is always limited to the unknown electronic structure of the tip. While geometry at the tip apex is successfully enhanced with field evaporation techniques its electronic structure may differ greatly from the bulk one due to unusual bonding geometry and small size.⁵

2.2 Atomic Force Microscopy

Introducing STM as a electronically sensitive method to investigate surfaces, the atomic force microscopy interacts in a different way with the sample. To scan the surface of the sample, one uses a small tip (cantilever) to interact with it. Due to its small distance different kinds of forces occur. The force induced movement of the tip is then interpreted and information about the surface may be derived. The layout of a typical consists of the cantilever itself and some kind of tip-position measurement. Earlier are made of the position-sensitive detector (PSD) consisting of two closely spaced photo diodes whose output signal is collected by a differential amplifier. Todays AFMs feature a Q-Plus sensor, as shown in Figure 2.3(b). Here the tip is positioned on top of an oscillating fork that is operated close to its resonance frequency. If the tip interacts with the sample, its oscillations is hindered and the frequency of the oscillation shifts. From this shift in frequency one can estimate the strength of the acting force. Since every type of adsorbate atom acts in different ways with the tip, AFM is element specific. A magnetic tip can be used to scan for magnetic forces on the sample surface. With an added wire to the AFM tip, simultaneous AFM and STM measurements are possible.

Types of forces are typically:

- Van-der-waals interaction (always attractive)
- Mechanical contact force (always repulsive)
- Capillary forces, chemical bonding, electrostatic forces, Casimir forces, solvation forces and others

⁵ Some[26, 81, 86, 140] groups have calculated band structures for different tip geometries and their influence on the tunneling process.

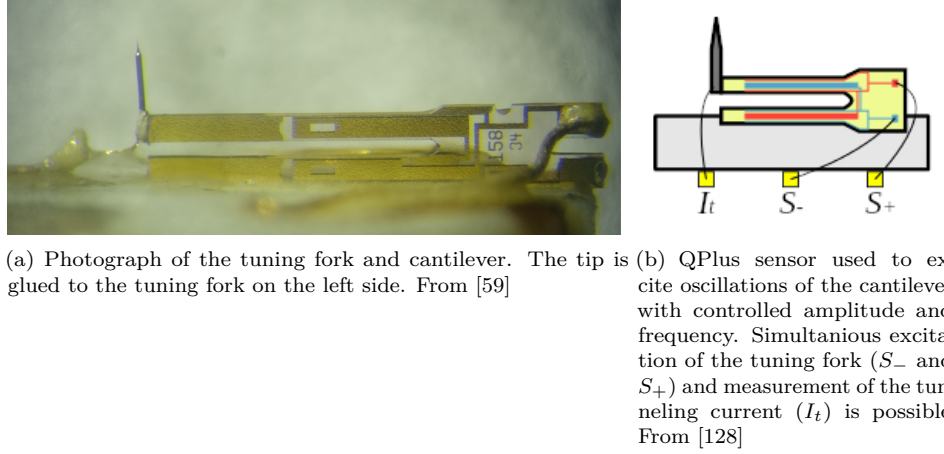
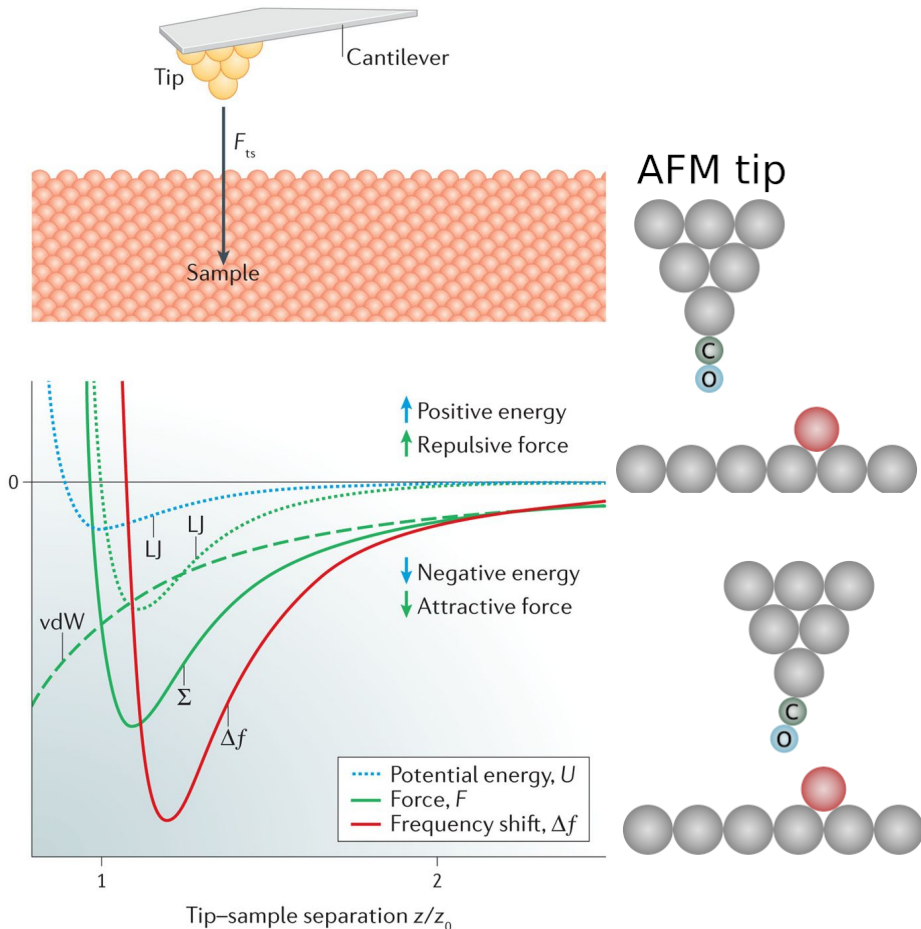


Figure 2.3: Photograph (a) and sketch (b) of AFM cantilever as used in the used setup.

The typical resulting force between tip and sample is artistically shown in Figure 2.4(a). On the top part a cantilever with an atomic tip is shown on top of the sample surface. The interaction forces F_{ts} act between tip and sample and are indicated by an arrow. In the lower part a representation of the resulting force in dependence of the tip-sample distance is shown. Although many different forces may act, the resulting potential is often modeled with a Lennard-Jones-Potential LJ [71]. Two of these are plotted with green and blue dots. The acting vdW force is plotted in dashed green. The sum of the acting forces is labeled \sum . A typical frequency shift Δf is given as red graph. One can distinguish different regimes as indicated by the arrows. When tip and sample are in considerable distance to each other, the attractive vdW forces are the dominant part in the sum. While the tip approaches the sample, more and more interactions with the surface and adsorbate add to this force, strengthening F_{ts} . When the separation reaches z_0 , the distance becomes so small that repulsive forces overcome the attractive one - entering the repulsive regime shortly afterwards. The best images were recorded close to the onset where F_{ts}

There are several operational modes to drive an AFM:

1. **Contact (static) mode:** The cantilever is operated in contact with the sample surface. At very close proximity, repulsive forces are stronger than the attracting ones. The signal used to gain information on the sample is either the feedback loop to keep the tip at the same absolute position or directly the deflection of the cantilever.
2. **Intermittent contact mode (tapping) mode:** While the contact mode has some disadvantages when scanning samples with an adsorbat layer (tip sticks to surface when close enough to measure short-range forces) another mode has established. Hereby the tip oscillates with amplitudes in the 100 nm to 200 nm regime and is not dragged the whole way across the sample. The intermittent forces acting on the tip when reaching the sample are measured. The change in amplitude when in close vicinity to the surface is a sign of the actual height.
3. **Non-contact mode:** The cantilever is driven at its resonance frequency with amplitudes smaller than 10 nm and at a certain distance to the sample. Long-range



(a) Schematic representation of cantilever tip and atomically flat sample surface. The force between both F_{TS} is indicated with an arrow. The attractive/repulsive force regimes are shown for varying tip-sample distances. From [113]

(b) Enlarged scheme of AFM tip and top most sample layer with single adsorbate atom. CO functionalization of the tip leads to an decreased tip apex that increases resolution. Modified from [128].

Figure 2.4: Basic function of a typical Q-plus AFM sensor. (a) Sketch of tip-sample interaction together with force-distance graph. The CO functionalization of the metallic AFM tip is shown in (b)

forces like van-der-waals and others change the resonance frequency of the cantilever. This change is a indication of the acting force between cantilever and sample. This mode is used within the scope of this work.

- AFM produces a true height-profile of the sample (and not a mix of electronic and geometric information projected onto a 2D-map like in STM)
- It has limited resolution especially when scanning features steeper than the tip apex

Its advantages are the comparable large image size of many hundred nm compared to only some dozen nm in the case of STM. Scan speeds are typically some orders of magnitude larger than those in STM so that image acquisition is much faster.

To increase the resolution the tip can be functionalized with CO (see figure 2.4(b)). This method is widely used⁶ to investigate not only geometric features that are not accessible in STM, but also chemical differences on the sample[wang_exploration_20170].

2.3 X-ray Photoelectron Spectroscopy

XPS is a tool to achieve information of the samples chemical structure. Most of the information given here is taken from [122] in [16]. When X-rays with sufficient energy hit metals, electrons are emitted. This effect is called photoelectric effect and was first discovered by Heinrich Hertz in 1887 through the fact that electrodes illuminated with ultraviolet light create electric sparks more easily[64]. 18 years later Albert Einstein received the Nobel Price for his discovery of the law of the photoelectric effect[143] and a scientific explanation which Hertz was missing.

The standard X-ray source is supplied with aluminum and magnesium anodes. Other materials are available that produce various X-ray energies and line widths [154].

As the X-rays hit and penetrate the sample surface they excite electrons and initiate different processes. The meajor two are discussed in the following.

For the **simple core-level excitation** the X-ray removes a single electron next to the core which is then detected. Energy conservation due to elastic scattering of the electron out of the bulk results in the relation

$$E_{kin} = h\nu_{X\text{-ray}} - E_B - \Phi_{bulk} \quad (2.4)$$

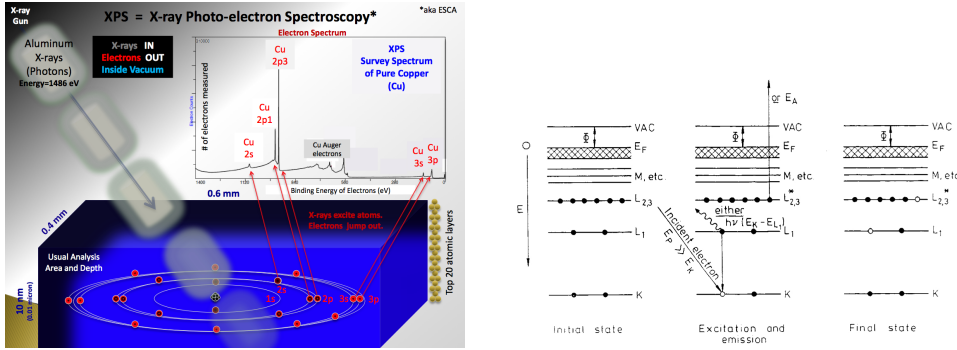
$$E_B = h\nu_{X\text{-ray}} - E_{kin} - \Phi_{bulk} \quad (2.5)$$

$h\nu_{X\text{-ray}}$ is the energy of the incident X-ray beam, E_B the binding energy of the excited electron and Φ_{bulk} the work function of the analyzer.

⁶Only a few examples from the recent years can be found here [2, 53, 75, 76, 113, 131, 135]

Table 2.1: Energy and line widths of available anode materials. Taken from

Anode	Radiation	Photon Energy (eV)	Line Width (eV)
Mg	K α	1253.6	0.7
Al	K α	1486.6	0.85
Zr	L α	2042.4	1.6
Ag	L α	2984.3	2.6
Ti	K α	4510.9	2.0
Cr	K α	5417	2.1



(a) Representation of XPS process. X-rays are used to excite core level electrons. After leaving the sample these show element specific signatures in their kinetic energies. A detailed analysis of the peak shape and shift allows for identification of the chemical environment.

(b) Two step Auger process. In contrast to a direct emission of a core electron, the Auger emission involves more electrons from less bound states. Here an (L_1) electron fills the hole in the K shell created by the initial X-ray. The resulting hole in the L_1 shell is then filled with an $L_{2,3}$ electron resulting in a typical Auger emission feature. Adopted from [15].

Figure 2.5: XPS and Auger processes present after irradiation of the sample with X-rays.

Two simultaneous processes occur. 2.5(a) shows a scheme of an X-ray gun illuminating a sample area of about $0.4 \text{ mm} \times 0.6 \text{ mm}$. Excited electrons within the first 20 layer escape the sample and are analyzed for their kinetic energy. Core electrons and Auger electrons are excited at the same time resulting in a chemical fingerprint of the sample.

In the **Auger process** on the other hand the created core level (lets say at level K) vacancy is filled with a energetically higher lying electron (at for example level L_1). The excess energy can either be radiated away (X-ray fluorescence) or given to an electron in the same or in a more shallow level (lets say $L_{2,3}$). This electron then can leave the sample as Auger electron. Figure 2.5(b) shows the mentioned process.

Due to the fact that this process has two stages these electrons are referred to as secondary electrons. The notation for this process is $KL_1L_{2,3}$. The electron taking part in the Auger process can also originate from within the valence band ($KL_{2,3}V$) or even both electrons may stem from the valence band (KVV). For every element there is a unique series of Auger excitations. This holds even if one or even both electrons come from a valence band, as the dominating term will always be the binding energy E_K . As the Auger energy

$$E_{KL_1L_{2,3}} = E_K - E_{L_1} - E_{L_{2,3}}$$

is not a function of the excitation energy it will not shift when changing the X-ray energy. Even very heavy elements (as the number of atomic levels the possible Auger transitions increases) do not exhibit a very large number of Auger emission lines due to the fact that the transition probability favors only a few of this many. [15]

[156] The chemical surrounding of atoms changes their binding energy, making XPS an ideal tool to detect changes in chemical surrounding. Although the analysis is averaged over the area of the incident X-rays (typically profiliate of microns up to several mm) its results are very precise. This makes it possible to distinguish differently bound atoms within single atomic species and therefore gives rise to otherwise not directly observable processes like growth, intercalation, etching and binding of for example graphene islands

Table 2.2: Element specific transitions and binding energies for some chosen elements as reported in [150]

Element	excited state	E_B [eV]
O	1s	531
N	1s	398.1
C	1s	285
B	1s	189.4
Cu	2p $\frac{1}{2}$ ($\frac{3}{2}$)	953 (933)
Cu	LMM	560-580
Cu	3s	123
Cu	3p $\frac{1}{2}$ ($\frac{3}{2}$)	77 (75)

Table 2.3: Spin-orbit splitting parameters. Ratios are reproduced from [122]

Subshell	j values	Area ratio
s	$\frac{1}{2}$	—
p	$\frac{1}{2}, \frac{3}{2}$	1:2
d	$\frac{3}{2}, \frac{5}{2}$	2:3
f	$\frac{5}{2}, \frac{7}{2}$	3:4

on Ir(111)[19, 51]. XPS is used to identify oxidation processes of copper surfaces as the interaction of oxygen with the copper surface changes the Cu core level. [33].

With the use of aluminum X-ray sources, electrons are accelerated with typically 15 keV onto the target. Most of the created radiation goes into the principal characteristic line ($K\alpha_{1,2}$). Higher ones ($K\alpha_{3,4}$, $K\beta$) are also observed but with much lower intensities. In addition there is a continuous background called Bremsstrahlung extending up to the energy of the incident electron energy. This background is of no use for the XPS measurement and has to be subtracted in a more or less artificial way.

For the ease of analysis, many spectra are recorded with monochromatic radiation. This selects a certain energy for the following illumination of the sample. This technique relies on the dispersion of X-rays within a crystal. It is described by the Bragg relation $n\lambda = 2d \sin(\theta)$ where n is the diffraction order, λ the wavelength of monochromatic radiation, d the distance between two crystal layers and θ is the so called Bragg angle. The first order peak for Al $K\alpha$ radiation ($\lambda = 0.83$ nm, $E = 1486.6$ eV) is at $\theta = 78.5^\circ$ (using the $10\bar{1}0$ planes of a quartz crystal with $d = 0.425$ nm). Therefore the angle between incident and reflected beam is about 23° .[122]

The spectra used in this work are recorded without monochromatic radiation as not stated otherwise. This is because the electron intensity is attenuated when using a monochromatic source.

The binding energies of some often observed peaks are given in table 2.2

Peak shapes The shape of the peaks typically resembles the line shape of the used X-rays (Gauss width ≈ 1 eV). In case of s-states ($l = 0$) (B1s, N1s, C1s) the peaks are singlets. With increasing $j = l + s$, the spin-orbit ($j-j$) coupling introduces a 'parallel' and 'anti-parallel' nature of the spin, resulting in two different $j = 1/2(3/2)$ and therefore two different energies. The split in energy is expected to increase as Z increases (for constant n,l) or as l decreases (n constant). This makes the splitting of 3p orbitals larger than that of the 3d's. The ratio of the two peaks is given by their degeneracy ($2j + 1$).[122, p. 113]

The more atoms of a specific kind are present, the larger the signal gets. Therefore the signal intensity resembles the amount of atoms on the topmost surface layers($\approx 10\text{ nm}$).

As each irradiated atomic species has a different cross section for adsorption of X-rays with a certain energy they emit auger and core level spectra with a different intensity. Comparing the cross section of e.g. N with B's, one can see that it is roughly 3 times to 4 times as large (B: $6.87 \times 10^3 \text{ b/atom}$, N: $25.82 \times 10^3 \text{ b/atom}$ for $\text{Al}K_{\alpha}$)[62]. Meaning that the signal from the N is much stronger than that of the B, although their number of atoms is equal.

A calibrated XPS is capable of measuring the surface coverage of an ad-layer (e.g. BN) compared to the bulk of the sample. Calibration works as follows:

- A perfect, full layer of a known material (e.g. C) is prepared (graphene)
- The known cross section for C ($6.87 \times 10^3 \text{ b/atom}$)[62] relates the signal to the number of atoms in the full layer.
- One then has to divide the signal of the unknown coverage (of known material) by the cross section (of C) and directly receives the coverage. Keep in mind that the X-ray penetration depth (and with it the signal of the substrate) stays only constant if the illumination angle stays constant. Even small angular variations may change the signal.

Referring to [43] the fraction θ_A of an adsorbate A on a surface B can be calculated via

$$\theta_A = \frac{I_A I_B^0 \cdot \exp(\frac{a_A}{\lambda_A} \cos(\Theta))}{I_A I_B^0 (\exp(\frac{a_A}{\lambda_A} \cos(\Theta)) - 1) + I_B I_A^0 \cdot \exp(\frac{a_A}{\lambda_A} \cos(\Theta))} \quad (2.6)$$

where the parameters are given in table 2.4.

Table 2.4: Description of parameters used in equation 2.6

Parameter	Annotation
I_A	integrated intensity of the adsorbate peak
I_A^0	cross section of element A
λ_A	mean free path of electrons in material A
a_A	thickness of adlayer

The mean free path of electrons with energy E in a solid is given by $\lambda_M = 0.41 \cdot a_M^{0.41} \cdot E_M^{0.5}$ where a_M is the atomic size of M.

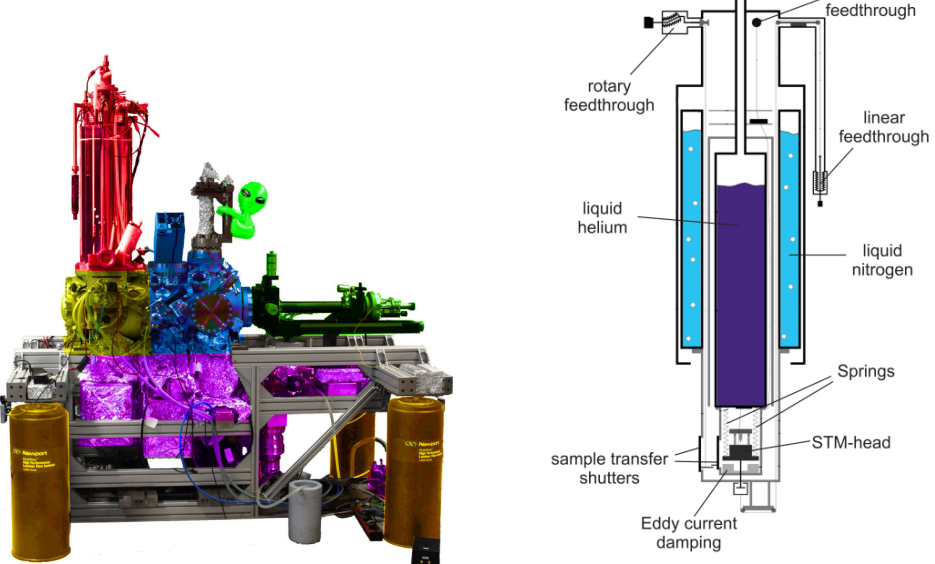
3 Experimental setup and sample preparation

To conduct experiments in the most controlled environment possible, sample preparation is done in ultrahigh vacuum (UHV) chambers. With a base pressure of $\approx 1 \times 10^{-10}$ mbar these stainless steel chambers are virtually free of contaminants. After cleaning the metallic substrates, ad-layers and molecular species are deposited and investigated without contaminations of residual gases. Experiments were done at three different experimental chambers: (1) A LT-STM chamber. The technical aspects of the preparation and experimental chamber are discussed elsewhere [134, 147, 152] and shortly summarized here. (2) A RT-STM with XPS capabilities. The technical aspects and build details are given in [134]. (3) The NIM-XPS chamber. This chamber is chosen because of it is possible to investigate chemical properties and coverage with XPS while an UV-Vis spectrometer is used to access the electronic structure of the occupied states. (4) A LT-AFM machine offers a complementary investigation method for geometric information. Its setup details can be found in [59].

3.1 Experimental setup

STMs may be operated at very different temperatures. The lowest temperature is only limited by the availability of sufficient cooling. While low temperature (LT) STMs may be operated with solely helium, it is more resource-saving to cool the direct proximity of the sample and the STM with He, but to suppress the heat flow out of the He-cryostat with a second surrounding nitrogen cryostat (boiling point: 77 K, compare figure 3.1(b)). This diminishes consumption of globally limited and rather expensive He. To maintain a temperature of 5 K to 7 K, one to two liters of liquid helium are required a day, plus an additional amount of three to four liters liquid nitrogen. Evaporated helium is reclaimed in a closed circuit with a system of purifying and storage/cooling steps so that only a small amount of helium escapes the circuit and is lost.

Sample temperatures down to 5 K to 7 K allow for observations not possible at elevated (room) temperature. Cooling not only reduces thermal drift in the piezo elements that are used to control the tip's position on the sample. Thermal energy at low temperature is not high enough for atoms or molecules to move on most substrates. Species mobile at room temperature (and therefore not representable at room temperature) become immobile and accessible for ST microscopy and spectroscopy. STS spectra resolution is better at low temperatures as discussed in 5.



(a) LT-STM setup mainly used in this work. Different functional groups are colored in different colors. A low base pressure is achieved with a combined pumping system comprised of ion pumps and turbo molecular pumps (cyan). The liquid helium/nitrogen bath cryostat (red) is used to maintain low temperatures. Sample holders are operated with a rote able, variable temperature manipulator. Sample preparation is done in a chamber (blue). After transfer to the LT-STM chamber (yellow) a gate valve is used to seal the LT-STM from remaining residual gas that may be present in the preparation chamber. Vibration isolation of the frame is achieved with legs floating on pressurized cylinders.

(b) Scheme of a STM liquid bath cryostat. While in the inner measurement stage a temperature of $\approx 5 \text{ K}$ to 7 K is achieved with a liquid helium reservoir, an outer liquid nitrogen cryostat is used to isolate the evacuated inner cryostat from the surrounding room temperature.

Figure 3.1: Typical setup for low temperature measurements. A vibration isolated UHV chamber is used to prepare samples and investigate them in a separable chamber with either STM or AFM. A liquid bath cryostat is used to maintain low temperatures. Images stem from diss-knud

3.2 Surfaces and ad-layers

Single crystals of copper and silver (terminated for (111) and (100) surfaces) are used as substrates as well as polycrystalline copper foils. All of them are used to deposit molecules. Some experiments are done to investigate molecules on *h*-BN/Cu(111) and *h*-BN/Cu(foil). The following sections will describe the relevant physical properties of the various substrates and will introduce a method to prepare polycrystalline copper foils to grow *h*-BN on.

3.2.1 Crystal facets

Single crystals show a nicely ordered, clean surface - two properties important for reliable and reproducible experiments. We have chosen both silver and copper as substrates. They form fcc lattices and their surface termination can be chosen by precise cutting along a symmetry plane of choice. For the course of this thesis, experiments are conducted mainly on (111) and (100) terminated surfaces.¹ Commercially available, single crystals guarantee a high precision in facet orientation and purity (99.999 %) [99]. Remaining contaminations in copper (Ag: 0.8 ppm, Pb: 0.3 ppm, Bi: 0.8 ppm) and silver (Cu: 2 ppm, Fe: 2 ppm, Au: 0.8 ppm, Ni: 0.8 ppm) are removed by repeated sputter and anneal cycles in UHV. Typical cool down temperatures $\leq 2\frac{K}{s}$ result in a smooth, atomically flat surface with large terrace size.

Dense packed rows are for fcc(111) the following directions: $<\bar{1}01>$, $<01\bar{1}>$, $<1\bar{1}0>$. The diagonals are found in the $<\bar{1}\bar{1}2>$ and $<\bar{1}2\bar{1}>$ directions. ADD INFO FOR 100!!!

Some experiments are done on polycrystalline surfaces of a copper foil. Here the surface termination is not homogeneous and is made of several domains with different facet orientation thus showing different step heights as indicated in table 3.2

The surface free energy increases from the (111) surface with increasing angle of the (hkl) planes of interest with

$$\cos(\phi) = \frac{h + k + l}{\sqrt{3(h^2 + k^2 + l^2)}}$$

[69]. Thus, the (111) surface is the one with lowest energy, followed by (110) and (100).

¹See [121] for another examples of vicinal metal surfaces (531), (532), (221), (311), (211).

Table 3.1: Inter atomic distances for Cu and Ag with respect to different surface termination. a denotes the lattice constant and $\beta = 60^\circ$ the angle within the (111) unit cell

	Lattice constant a [\AA]	Nearest neighbors [\AA]	diagonal [\AA]
Cu	fcc(100)	$\frac{\sqrt{2}a}{2}$	a
	3.61	2.55 2.55	3.61
Ag	4.09	2.89 2.89	4.09
	fcc(111)	$\frac{\sqrt{2}a}{2} < 110 >$	$\sqrt{2}a \sin(\frac{\beta}{2}) \sqrt{2}a \cos(\frac{\beta}{2})$
Cu	3.61	2.55 2.55	2.55 4.42
	4.09	2.89 2.89	2.89 5.01

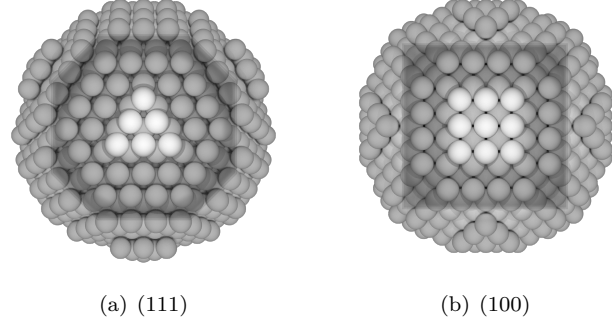


Figure 3.2: Identical crystalline balls in fcc lattice configuration. The surface termination is determined by the direction of the intersecting plane (parallel to the paper plane) relative to the lattice.

Table 3.2: Crystal properties from [92, 97, 121, 29ff]

		Copper	Silver
Lattice constant		3.61 Å	4.08 Å
Nearest neighbor		2.55 Å	2.89 Å
Step height	(311)	4.23 Å	4.78 Å
	(211)	6.25 Å	7.07 Å
	(221)	7.66 Å	8.65 Å
	(110)	1.38 Å	
	(111)	1 Å	
	(100)	1.8 Å	

3.2.2 Dislocation lines and crystal orientation

Due to the fact, that dislocation lines move within the crystal in a well defined manner, one can determine the crystals orientation when the orientation of a dislocation is known. For fcc crystals the orientation of dislocation lines occurs in the 111 plane in $\langle 110 \rangle$ direction. Its Burgers vector is $\frac{a}{2}[110]$ [37]. ADD INFO FOR 100!!!

3.2.3 Surface states

In the discussion of surface states, one generally distinguishes between Shockley states[5] and Tamm states,[6] named after the American physicist William Shockley and the Russian physicist Igor Tamm. However there is no real physical distinction between the two terms, only the mathematical approach in describing surface states is different.

Shockley states - Electron gas approximation from wikipedia article

Historically, surface states that arise as solutions to the Schrödinger equation in the framework of the nearly free electron approximation for clean and ideal surfaces, are called Shockley states. Shockley states are thus states that arise due to the change in the electron potential associated solely with the crystal termination. This approach is suited to describe normal metals and some narrow gap semiconductors. Figures 1 and 2 are examples of Shockley states, derived using the nearly free electron approximation.”

Tamm states - Tight binding approximation (LCAO) from wikipedia article

Surface states that are calculated in the framework of a tight-binding model are often called Tamm states. In the tight binding approach, the electronic wave functions are usually expressed as linear combinations of atomic orbitals (LCAO). In contrast to the nearly free electron model used to describe the Shockley states, the Tamm states are suitable to describe also transition metals and wide gap semiconductors.

Extrinsic surface states from wikipedia article

Surface states originating from clean and well ordered surfaces are usually called intrinsic. These states include states originating from reconstructed surfaces, where the two-dimensional translational symmetry gives rise to the band structure in the k space of the surface.

Extrinsic surface states are usually defined as states not originating from a clean and well ordered surface. Surfaces that match the category extrinsic are :

- Surfaces with defects, where the translational symmetry of the surface is broken.
- Surfaces with adsorbates
- Interfaces between solid and liquid phases.
- Interfaces between two material such as a semiconductor-oxide or semiconductor-metal interfaces

Generally, extrinsic surface states cannot easily be characterized in terms of their chemical, physical or structural properties.

3.2.4 Electro polishing

As was mentioned before, clean, highly ordered surfaces are desirable to perform experiments on. Effort is done to clean the surfaces before every experiment to ensure a reproducible environment and interpretable results. This lead to a detailed understanding of the physics and chemistry behind a lot of systems. In case a systems order and functionality does not heavily depend on the substrates symmetry, single crystals loose most of their unique selling point. Instead of choosing a expensive bulk single crystal, thin copper foils can catch up in production environments. The mass produced foils still show some inconvenient properties. Although pure copper foils ($\geq 99.999\%$) are available, their surface was never meant to be atomically flat. A representation of a copper surface before electro polishing can be seen in figure 3.3. Here the layered structure of the (mechanically polished) foil is apparent and shows different sizes of grains and annealing twins at the surface. Small subgrains constitute the uppermost layers, while deeper lying layers consist of larger grains with grain boundaries becoming more and more diffuse with increasing distance to the surface.

But growing high quality ad-layers on polycrystalline copper foils requires a smooth surface. As-ordered Cu foils exhibit a root-mean-square (RMS) surface roughness of about 218 nm[11]. Striations - a fabrication remnant due to the cold rolled foils - are observed on the surface[80]. Also some manufacturers apply a thin layer of chromium oxide for corrosion protection[11]. A common procedure to reduce the roughness of a material is to electrochemical polish the surface.

A comprehensive overview of electrochemical polishing of Cu surfaces with different etchants can be found in [70]. The following gives a short introduction in chemical polishing as used for preparation of thin copper foils.²

solution of anode atoms in aqueous cell medium

Electrons and atoms at the solid surface have higher energy states. Thus some of the atoms on the metal surface may lose electrons to form ions. These ions may also recombine with electrons and become atoms at another moment. Depending on the electronic structures, some metals (such as sodium) are easier than others (such as platinum) to ionize. Copper is relatively stable. Still, some of the surface atoms may be expected to ionize at a moment. The ionization process may be promoted when the metal is in touch with aqueous solution because:

- Metal ions can not move in the metal electrode but can move through the solution, producing electric current in solution with an applied potential
- Electrons can move freely in metal solid (electric current in a metal) but can not survive in solution and will quickly recombine with positive ions
- Water dipoles and negative ions in solution may drag the surface metal ions into the solution

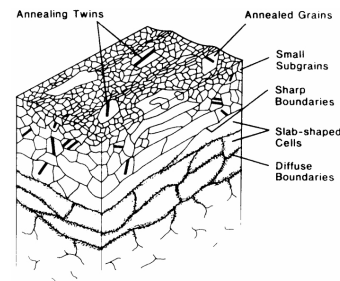


Figure 3.3: Proposed bulk structure of a OFHC copper foil after abrasion with P1200 silicon carbide paper. Adopted from [146]

²For a broader view on the topic, the reader is pointed to references [3, 90, 130].

chemical reaction “The electrode connected to the positive pole of the power supply is called anode. And the one connected to the negative pole of the power supply is called cathode. When the applied voltage is high enough, electrons in the anode may be pumped out and the metal atoms on the anode surface will be oxidized (e.g., $Cu - 2e = Cu^{2+}$) and dissolved into the electrolyte solution. Under electrical field, the positive ions (cations) move towards cathode and negative ions (anions) move towards anode. The cations may get electrons and be reduced to neutral atoms (e.g., $Cu^{2+} + 2e = Cu$) again at the cathode surface. Therefore, charge transfer between the two electrodes is carried out via the ion drift in the electrolyte and electron conduction in metal wire. When the working electrode is set to be anode, dissolution is processed at certain potential. Likewise, when the working electrode is set to be cathode, it can result in deposition. For electropolishing of copper, the copper part to be polished is set to be anode while the cathode can be any conductive material (e.g., copper).

The critical potential at which the oxidation / reduction starts to occur is related to the standard redox potential for a specific anode material. The redox potential E_O is a measure (in volts) of the affinity of a substance for electrons - its electronegativity - compared with hydrogen (which is set at 0). Substances more strongly electronegative (i.e., capable of oxidizing or accepting electrons) than hydrogen have positive redox potentials (e.g., Cu/CU^{2+} : $E_O = 0.34$ V). Substances less electronegative (i.e., capable of reducing or giving up electrons) than hydrogen have negative redox potentials (e.g., Cr^{3+}/Cr^{2+} : $E_O = -1.07$ V)[70]

Removed mass from working electrode “The current flow of every two electrons results in one copper atom dissolved on the anode and deposited on the cathode. Since $1\text{ A} = 1\text{ C s}$, the charge of one electron $e = 1.60218 \times 10^{16}\text{ C}$, so the number of electrons (per second) in 1 A current is $N_e = \frac{I}{e}$; the number of copper atoms being oxidized or reduced $N_a = \frac{1}{2}N_e = \frac{I}{2e}$; the number of moles $N_m = \frac{N_a}{N_A} = \frac{I}{2eN_A} = \frac{I}{2F}$ where Avogadro's number $N_A = 6.02214 \times 10^{23}\text{ mol}^{-1}$. The weight of N_m mole copper $W = N_m M = \frac{IM}{2F}$ where M is the molecular weight of copper. Thats a volume, $V = W/d = \frac{IM}{2Fd}$ where d is the density of copper. Thus a current I produces a dissolution/deposition rate in thickness (cm s^{-1})

$$R_d = \frac{M}{2FdA} I \quad (3.1)$$

where A is the area of the electrode surface. [70, p. 34]

Voltage-current-characteristic or polarization curve

- On a polycrystalline metal surface there are sites, such as defects and grain boundaries, where atoms are at higher energy states. In addition, due to arbitrary crystal orientation, there are different crystalline planes with different energy states of atoms on the electrode surface. Therefore, atoms at all these different sites and planes have different standard redox potential E_O , and as a result, have different dissolution rate according to eq. 3.1. Such an anodic dissolution will not lead to polishing. Instead, a crystallographic etching is produced (reference [9, 33-35] within [70]). This is true at lower current (or applied potential). This refers to the "etching" regime in figure 3.4(b) with $U < 1.5$ V.
- The plateau where the current remains almost constant with increasing voltage is referred to as "**polishing plateau**". Overall, the values of i_L and E_L of the limiting current plateau and the shape of a polarization curve depends on electrolyte

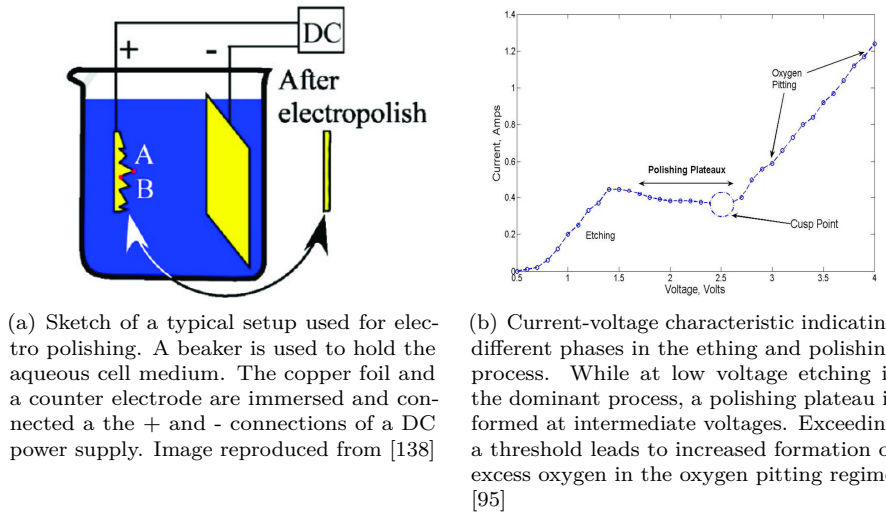


Figure 3.4: Experimental setup and voltage characteristic used for electrochemical polishing. 3.4(a) In the process the foil is connected as working electrode (+) and opposed by a counter electrode (-). Material is then transported from the working to the counter electrode resulting in a polished foil surface. 3.4(b) Choosing proper voltage and current values in the polishing plateau is important for good results.

solution, anode material, disk rotating speed, solution circulation, temperature, and the distance between anode and cathode. Of all the factors, electrolyte is the most important one determining the polarization curve.

- With continuing increase of applied potential, other reactions than Cu oxidation and reduction may occur and contribute to the increasing current. These reactions produce H_2 and O_2 bubbles, which occur at or reach the anode surface. This is known as "**oxygen pitting**".

gas bubbling Gas (oxygen or hydrogen) bubbles may block Cu^{2+} ion transport and therefore terminate the electrochemical dissolution process on the area inside the bubbles. However, the residual solution on the surface area inside the bubbles may react with Cu atom and result in chemical etching. Depending on the chemical property of the electrolyte solution and the value of current density at which the electrochemical dissolution is occurring, the etching speed can be higher than the rate of electrochemical dissolution. In this case, pits will be produced on the anode and produce a rough surface. If etching does not occur inside the bubbles, or if its speed is slower than that of electrochemical dissolution process, the area inside the bubbles will remain and appears as protruding particles after the electrochemical dissolution process. In either case, a rough surface is produced. Approaches to reduce the effect of oxygen bubbling are done by altering the etching solution with different additives.

Etching solutions in literature To find the most adequate polishing recipe, the most common ones have been reviewed and will be shown in the following. Many etching

Table 3.3: Table with some of the found etching recipes.

	unit	[95]	[138]	[11]
H_3PO_4	[mL]	300	100	50
H_2O	[mL]	—	—	100
2-Propanol	[mL]	—	—	10
Ethanol	[mL]	—	—	50
Butanol	[mL]	—	—	—
Urea	[g]	—	—	1
(P)EG	[mL]	100	0.1	—

processes of Cu foils base of phosphoric acid that is referred to as ortho-phosphoric-acid, too. Liquid phosphoric acid is an 85% aqueous solution. [20]

Here (table 3.3), some of the etching recipes are given as reported in literature. They all have been used to electrochemically polish the Cu foil prior to graphene or boron nitride growth. We will discuss the used recipes in the following with focus on the additives used.

Different additives to the acid are used to gain a better control of the etching process. A typical one is PEG.³

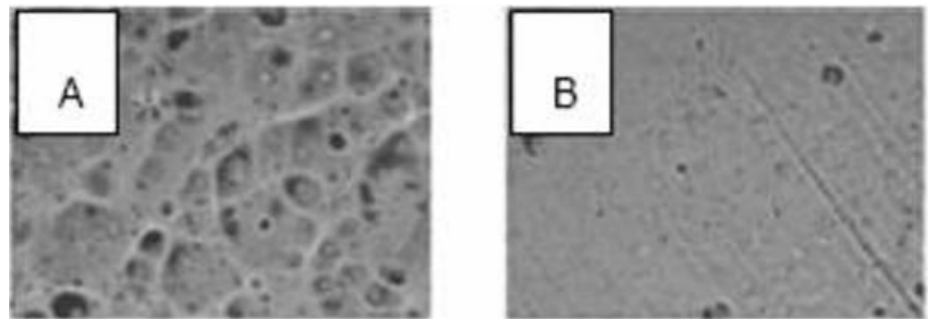
One may add PEG for reduced oxygen bubbling during the process (compare fig. 3.4(b))[22, 138]. It was shown that a concentration of 1000 ppm PEG decreases the amount of oxygen pits. A comparison between electro polished foils with and without PEG are shown in figure 3.5. After etching with purely phosphoric acid the surface remains rough and covered with pits. After adding PEG to the polishing solution the resulting foil shows a smoothed surface with little oxygen pits left.

A detailed investigation on polishing solutions based on phosphoric acid can be found in [70]. It was found that adding EG into phosphoric acid solutions decreases the limiting current. The more EG added the lower the limiting current. This is true for both undiluted and diluted (with deionized water) phosphoric acid solution. Diluting phosphoric acid - EG solutions with water (25%, curve 2 in Fig. 3-10 within [70]) increases limiting current as shown in table 3.4. Further diluting phosphoric acid - EG solutions with water (50%, curve 3 in Fig. 3-10 (within [70])) decreases limiting current. Limiting current plateau disappears at 12.5% phosphoric acid + 37.5%EG + 50% water. As the etching times are quite long, efforts have been made to reduce the polishing time by varying the polishing solution. Results with a more complicated etching recipe [11] are depicted in figure 3.6. Here the etching was performed with a large copper plate used as cathode. Alligator clamps are used to apply a voltage of 3 V to 6 V between the foil and the plate. The foil is used as anode (+). After 1 min the foil is taken out and rinsed with deionized water, further washed with ethanol, and then dried with compressed nitrogen gas.

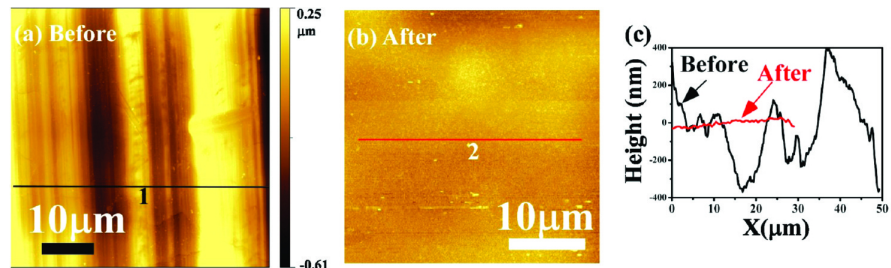
The height profile of the copper foil surface before and after treatment indicate diminishing striation height and overall roughness from $\approx 218\text{ nm}$ to 64 nm within a very short period of time. Although the surface is still rather irregular, a dominant orientation of the remaining grains is observed in the (001) direction and helps the subsequent growth of graphene with toluene to form rectangular flakes.

Experimental setup

³Further additives are used in etching solutions. Isopropanol and Ethanol are introduced for a more stable current density. HEDP increases the critical current density in phosphoric acid solutions[70] and therefore the reaction rate. Citric acid is also used at low concentrations 1000 ppm [22]

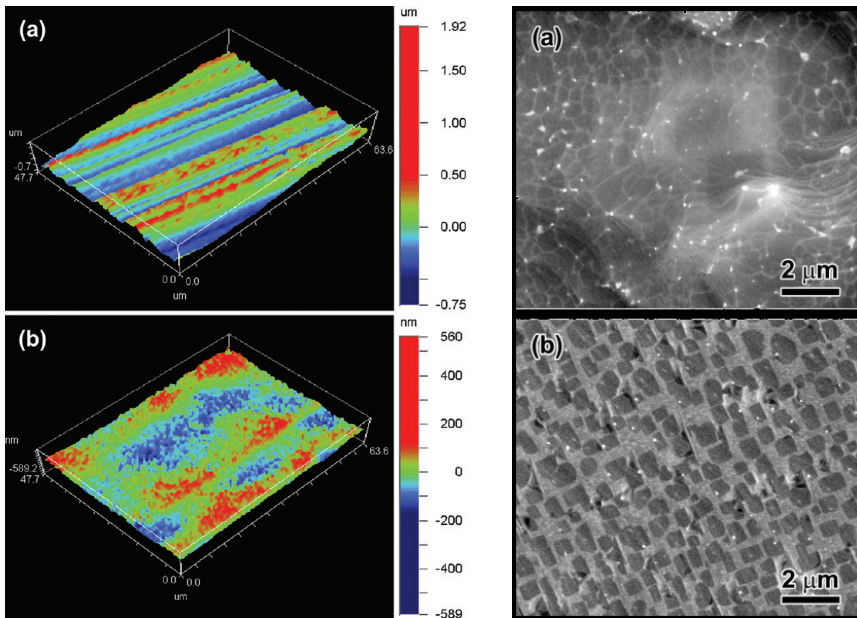


(a) Surface characterization with an interferometer. Oxygen pits are clearly visible in (A) while after adding 1000 ppm PEG to the polishing solution greatly reduced their amount and smoothes the surface (B). See [138]



(b) (a-b) Copper foil before and after etching with 1V to 2V for 0.5 h following recipe [95]. Corresponding height profiles are shown in (c). Adopted from [95]

Figure 3.5: Effect of adding PEG to the etching solution. Interferometric and AFM topography images before and after polishing.



(a) Noncontact optical profilometer scans in VSI mode of unpolished (top) and polished (bottom) Cu-foil surface.
 (b) SEM images after graphene growth with a toluene precursor at 550 °C

Figure 3.6: Height profiles and SEM images before and after 1 min electro polishing with a solution reported in [11]. The linear striations, caused by mechanical processing of the copper foil, and the overall roughness of the surface decrease after polishing. Graphene coverage is increased under the same growth conditions, solely through better substrate conditions.

Table 3.4: Used etching solutions (compare [70, p. 130]). Note the change in the removal rate due to higher limiting currents in the solution after adding ethylene-glycol to the solution.

	I	II
85 % H_3PO_4	70	100
Ethylene-glycol	5	0
Deionized water	25	0
Potential [V]		1.2
Current [mA]	46	12
Roughness [nm]		5
Removal rate [$\mu\text{m min}^{-1}$]	1.0	0.26

Table 3.5: Volume and mass fractions for copper foil etching solution.

	unit	H_3PO_4 (85%)	EG	H_2O
Dichte ρ	[g/cm^3]	1.87	1.11	1.00
$1/\rho$	[cm^3/g]	0.54	0.90	1.00
Anteil	%	70	5	25
Menge gesamt	[cm^3]		150	
Menge anteilig	[cm^3]	105.00	7.50	37.50
Gewicht	[g]	196.35	8.33	37.50

Used solution Within this work, Cu-foil polishing will be done with recipe I broken down in Table 3.5. It has several advantages. Since the main goal is the achieve a virtually flat surface, the resulting roughness of the surface is the most important parameter. In contrast to etching recipes without PEG (where oxygen pitting is an issue) and more complex etching recipes (to reduce etching time on exchange on surface roughness) a simple etching solution is chosen.

The etching process The etching process relies on the fact that the current density (and thus the etching rate) is higher in protruding regions of the copper foil (Ohmic leveling). As a result the surface of the copper foil will be smoothened [95]. Compare with migration smoothing and diffusion smoothing[70].

3.2.5 Growing atomically thin ad layers with Chemical Vapor Deposition

There are many ways to grow ad layers with controlled stoichiometry in UHV. Here we will only focus on the most used method for sub mono layer and mono layer growth - the chemical vapor deposition (CVD).

When a gaseous precursor comes on contact with a hot transition metal surface, the precursor is split by pyrolysis into fragments. These then distribute across the surface and form new structures in a self-organized process. Choosing the right growth parameters like temperature, precursor partial pressure and time, high quality layers can be grown, whose stoichiometry is determined by the chemical structure of the precursor. Using carbon rich gases like ethylene (C_2H_4) [27, 107] and coronene ($C_{24}H_{12}$) [27] as precursor and a transition metal as substrate results in a graphene layer to be formed. Using boron

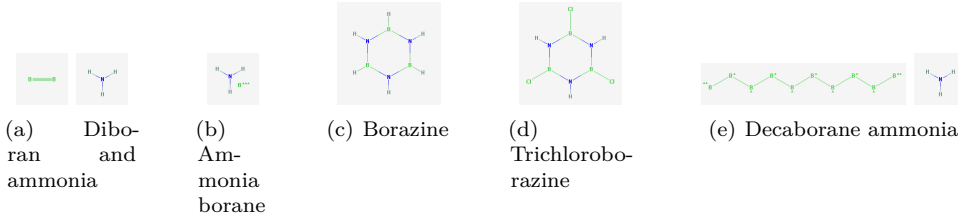


Figure 3.7: Precursor molecules for *h*-BN growth. (a) A mixture of ammonia and diborane, (b) ammonia borane, (c) borazine and (d) B-Trichloroborazine, (e) a mixture of decaborane and ammonia. Images reproduced from [1]

and nitrogen containing molecules (see Figure 3.7)⁴ as precursor will result in *h*-BN to be formed. Hereby either single crystals⁵ or polycrystalline foils⁶ are used as substrates. These play a key role in interaction strength with the ad layer. Their lattice constant determines the mismatch with the ad layer. For some of these systems, DFT calculation back up experimental results [48].

self-limitation The precursors decomposes on contact with the hot substrate surface and its fragments form the ad layer. As time goes by, the ad layer grows in coverage and less free hot surface area is available for decomposing new “building blocks” for mono layer formation. If a mono layer is formed, no additional second layer is formed because of missing building blocks which only arise on contact with the uncovered substrate surface. Therefore this process is called self-limited. It is observed [21, 28, 106] for various substrates in combination with a borazine precursor.

The growth by itself is well investigated on transition metal surfaces [48, 103], on the copper and nickel surfaces [73, 119]. Even more complicated samples can be created with this technique [126] and the following gives a short introduction in the occurring growth processes.

Some growth mechanics can be seen best in figure 3.8 that shows a XPS spectrum of borazine adsorbed on a Iridium surface held at 170K and after several annealing steps.

At the graphics’ bottom one can see the clean Ir surface with no borazine adsorbed (no B1s signal). There are two contributions in the Ir-peak. While the low energy (Ir_s) peak stems from the surface atoms of the substrate, Ir_b denotes the contribution from the atoms in the bulk. Upon borazine adsorption (1) a broad $B1s$ emerges accompanied with a new contribution in the Ir-peak (Ir_i) which is a result of borazine-Ir interaction decreasing the area of I_b and I_s . Upon annealing ((2)-(6))

⁴*h*-BN CVD precursor:

- Borazine [5, 29, 50, 73, 78, 79, 89, 103, 106, 118, 119, 135]
- B-Trichloroborazine ($ClBNH_3$) [8, 105]
- Ammonia borane (borazane) [55, 80, 87]
- Diborane and ammonia [67]
- Reaction of ammonia with decaborane [23]
- Triethylborane and ammonia [136]

⁵Single crystals used as growth substrate for *h*-BN:

- (111): Ag [106], Cu [73, 89, 119, 135, 136], Ni [5, 8, 108, 119], Rh [29, 118], Pd [103, 108], Pt [105, 108, 118], others: Cu(100) [55], Ru(0001) [50, 118]

⁶Polycrystalline foils used as substrate:

- Cu: [23, 55, 67, 78–80, 87]
- Ni: [23, 67]

Ir_i loses in intensity while the I_b and I_s recover to their initial position. Interesting changes happen to the $B1s$ peak. While at lower temperatures, several peak contributions can be distinguished, denoted as B_{mol} for entire molecules and B_{ad} for molecular fragments. With increasing temperature, B_{mol} decreases for a increase in the B_0 peaks. At lower temperature (1), B_{mol} decreases and B_{ad} slightly increases.

When exceeding 620K ($\approx 350^{\circ}\text{C}$, (3)) a new peak emerges and develops into B_1 when increasing temperatures. When temperature is high enough the only peaks left are B_0 and B_1 - the two contributions of boron atoms stem from boron atoms interact with the Iridium substrate with different strength due to different registry to the substrate.

While the growth temperature and partial pressures used to grow defect free $h\text{-BN}$ layers varies, the basic principle remains the same on all substrates.

The exact growth of mono- and multi layers [67] is prone to discussion and may involve

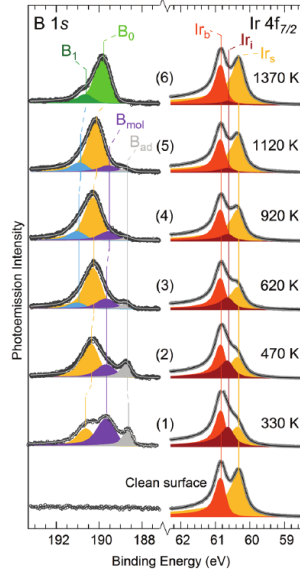


Figure 3.8: RT XPS spectra ($B1s$ and $Ir4f\ 7/2$) of borazine adsorbed on a Iridium surface held at 170 K and after step-wise annealing to 1370 K. Adopted from [110]

The properties of various moiré superstructure are well described in literature and Hermann gives a comprehensive overview in his paper [63]. One can conclude the following:

If lattice constants are equal like in the case of a graphene bilayer, the needed lattice mismatch occurs due to a rotation of the two layers. A moiré is always present if an over layer shows a lattice mismatch with respect to the substrate.

For **isotropically scaled over layers** (refer to figure 3.9(a)) one can calculate the scaling factor

$$p = \frac{R'_{O1}}{R_{O1}}$$

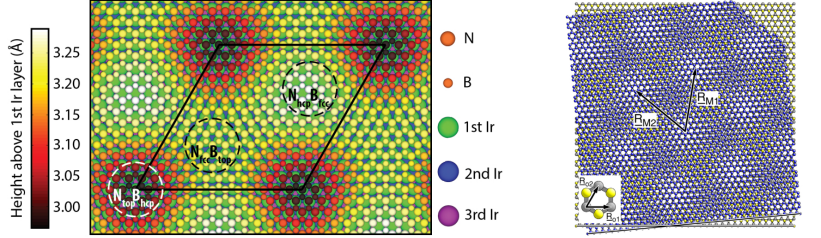
which gives the size of the over layer lattice in units of the substrate lattice. The moiré pattern shows the same Bravais lattice type than the substrate[63, p. 10]. If moiré and ad layer lattice are aligned ($\alpha = 0^{\circ}$) the direction of moiré and substrate is aligned. If the over layer is isotropically scaled and not rotated, the period of the moiré calculates to

$$a_{\text{moiré}} = \underbrace{\frac{p}{|p-1|}}_{\kappa} a_{\text{substrate}}$$

. With $a_{\text{moiré}}$ and $a_{\text{substrate}}$ are experimentally available, the ad layer lattice can be calculated with high precision (usually one order of magnitude more accurate than direction measurement of its period).

For a **scaled and rotated over layer** (figure 3.9(b)), the angle between substrate and moiré ($\gamma[\text{rad}]$) scales with the angle between over layer and substrate ($\alpha[\text{rad}]$) as $\alpha = (1-p)\gamma$.

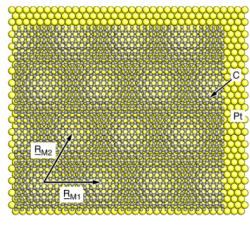
For rotated and isotropically scaled over layers, one can determine the α and p from experimental observables γ (moiré angle to substrate) and κ (scaling factor) through relations $\tan(\alpha) = \frac{\sin(\gamma)}{\cos(\gamma)+\kappa}$ $p = \frac{\kappa}{\sqrt{1+\kappa^2+2\kappa\cos(\gamma)}}$



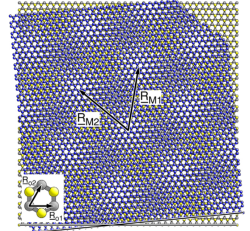
(a) DFT simulation of *h*-BN on Ir(111). The moiré unit cell as well as regions where B and N atoms occupy high-symmetry positions w.r.t. the Ir lattice are indicated. The change in adsorption height is caused by the changing registry of substrate (Ir) and ad layer atoms (B,N). Adopted from [132]

(b) STM image of *h*-BN grown with CVD on Ir(111)

Figure 3.10: DFT calculation and STM images of *h*-BN/Ir(111). While being aligned, a lattice mismatch creates a moiré superstructure. It is well visible in adsorption height calculations 3.10(a) and as apparent height differences in STM images 3.10(b).



(a) Isotropically scaled and aligned overlayer (gr/Pt(111): $p = 0.89$)



(b) Isotropically scaled overlayer with rotation of 5.4° (gr/h-BN: $p = 0.98$)

Figure 3.9: Adopted from [63]

When a scaled over layers over grows a step edge, the moiré pattern is altered. While period and orientation remain the same, a lateral shift in the superstructure is observed that interrupts the regular pattern and shifts subsequent moiré features by a vector \vec{V} .

Periodic change in work function A direct result of the lattice mismatch between *h*-BN and substrate is the alternating registry of ad layer atoms and substrate. The periodic modulation of B/N registry to the substrate atoms results in regions of stronger and weaker interaction between *h*-BN and substrate and is the reason for the nano templating effect of *h*-BN on many substrates. In the following some resulting effects are discussed that lay the foundation for a nano patterning effect of *h*-BN and its influence on the electronic structure of adsorbates.

After growth of *h*-BN the substrates work function is reduced [Rh: 5.01 eV to 3.07 eV [48]. Therefor a dipole moment μ pointing from the bulk to the surface is necessary [125], rather likely created by a negative charge transfer from the bulk into the ad layer.

Free standing *h*-BN is investigated with *ab-initio* calculations [56, 104, 114, 144]. Together with experiments [112] a crystal lattice constant of $a_{h-BN,RT} = 2.504 \text{ \AA}$ is derived. Depending on the substrates used, different lattice mismatches can be achieved as listed in Table 3.6. While substrates exist where the lattice constant are virtually identical ($\Delta \approx \leq 1\%$), other substrates like Ag(111) show considerable deviations.

While a first report in 2004 [29], pointed to the formation of a complicated two layer structure, later experiments [89, 126] including ours [73, 135] and others *h*-BN/Cu(111)

Table 3.6: Lattice mismatches between *h*-BN and several transition metal surfaces. The mismatch is given to describe the relative size of the h-BN layer compared to the substrate, e.g. negative values indicate a larger lattice constant in the substrate bulk.

Substrate	Mismatch [%]
Ni(111)	0.4 %
Cu(111)	-1.9 %
Rh(111)	-7 %
Pd(111)	-9 %
Ag(111)	-13 %

proposed a single layer of B & N atoms in a regular hexagonal lattice. It evolved as well investigated system to perform experiments on. It could be shown that after CVD growth it adsorbs on Cu(111) as a flat layer. Due to its lattice mismatch, "hill" regions (corresponding to a $N_{top}B_{fcc}$ registry) and "valleys" (corresponding to a $N_{fcc}B_{hcp}$ registry) are formed. In these regions the work function is altered in opposite directions. While larger at the hill/pore regions, the work function reduces continuously to its lowest value in the valley/wire regions⁷.

With changing work function, a lateral electronic field emerges, pointing from _____. It can be used to trap adsorbates with dipole moment along the field lines. This was shown for FePc and pentacene molecules on a graphene/Ru(0001) substrate. Here FePc molecules adsorb first on regions with high lateral dipole along top-fcc direction, followed by regions with lower lateral dipole. Pentacene molecules are trapped along the top-fcc direction [157]. This general adsorption mechanism is applicable for other systems with periodic modulation of the work function. ?? depicts the work function change measured with STM (Field emission resonances) indicating a similar modulation of the work function. In this thesis TPB molecules (?? and helicene molecules in ?? are used as sample molecules for specific adsorption site or orientation alignment.

As mentioned in subsection 3.2.6 the orientation of the moiré superstructure is determined by its rotation alone, while its period is determined by lattice mismatch, too. This results in a variety of moiré superstructure orientations and periods.

3.3 Used molecules

The following molecules have been used to conduct experiments. Images show the molecules in a $4\text{ nm} \times 4\text{ nm}$ area in an orthographic projection. Since all of them feature distinct properties, all of them are introduced in the following subsections. We will utilize porphyrine derivatives (subsection 3.3.1), functionalized pyrene molecules (subsection 3.3.2), helicene species (subsection 3.3.3) and coronene (wo central borazine functionalization, see subsection 3.3.4).

⁷Please note that the notation is not uniform throughout the literature. Sometimes hills are referred to as pores and valley regions are denoted as wire regions.

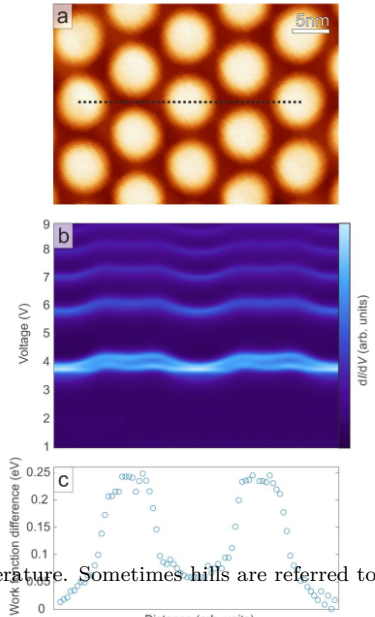


Figure 3.11: Work function variation along *h*-BN/Cu(111) moiré.
 (a) STM image showing the *h*-BN moiré with a periodicity of 8.4 nm. Scan parameter: $U_b = 4.0\text{ V}$, $I_t = 40\text{ pA}$. (b) Field emission resonances (FER) plot showing the variation of the work function difference (V) versus distance (arb. units). The plot shows a periodic modulation of the work function difference, corresponding to the moiré periodicity. (c) A scatter plot of work function difference (eV) versus distance (arb. units), showing the discrete nature of the work function variation across the moiré superstructure.

All the depicted molecules are modeled in Hyperchem[65] and calculated for optimized geometry with the AM1+ method. Afterwards their positions are exported and remodeled in blender. Note that this does not change their geometry. It is only for better control of the output (faster and more accurate model building especially in 3D) and for some aesthetic reasons.

3.3.1 Porphine: [di-[tert-butyl]-phenyl)]-porphyrin derivatives

Tetrapyrroles like porphyrins and phthalocyanines play important roles in biological systems [9]. Both species are able to incorporate metal atoms that control the function. Not only are they interesting model systems to study interaction towards a (metallic) substrate[6, 7, 35]. Their use in metal-organic frameworks highlights the use of scientific knowledge to design "real world" sensor applications[96].

Tert-butyl functionals have been used in a variety of molecules [102]. Due to their bulky nature, they electronically decouple the porphyrin's de-localized p-orbital system from the metallic surface just by lifting the molecule. They may undergo heavy conformational deformation when outer influences (like metalization of the central porphine core) act on the molecule [139]. Switching capabilities are well investigated [93] and it is possible to switch them with the STM tip [39]. Experiments with similar molecules investigate the heat-induced formation of 1D and 2D conglomerates on a Au(111) surface.[116]

- Free base nitrophenyl - 5,10,15 Tri [di-[tert-butyl]-phenyl)]-porphyrin has 3(2) di-tert-butyl-phenyl groups attached to the porphine macrocycle at the meso-positions of the molecule. The free meso-positions are occupied with nitrophenyl groups as shown in Figure 3.12(a). If more than one functional group is present, one can distinguish between trans (Figure 3.12(b)) and cis configuration (Figure 3.12(c)), whether the two functional groups are opposite or neighboring.
- The appearance of STM data is correlated to the molecular configuration according to [101] meaning that the lobes consisting of (3,5-di-tert-butylphenyl) are imaged as bright protrusions, while the functional nitro group is imaged fainter. This holds true for cis- and trans-substituted molecules[155].
- Tert-butyl groups can rotate and form flexible

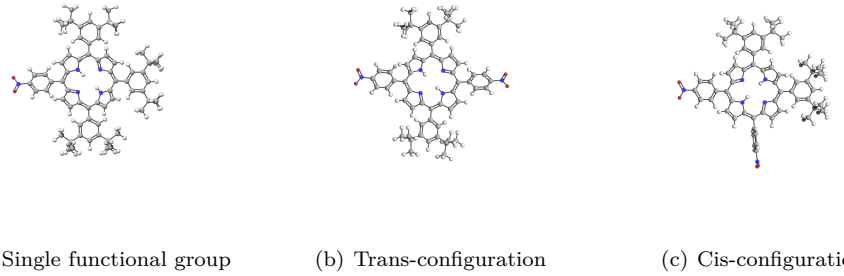


Figure 3.12: Functionalized tert-butyl-phenyl-porphines. (a) shows a single functionalized porphine molecules. An additional function may be added in (c) cis- and (b) position.

legs. Interaction with the substrate results in adsorption-induced conformational changes.[41]

Drawings for various functional groups and molecules can be found in [72]

one-leg: 5,10,15-Tri(3,5-di-tert-butylphenyl)- 20-(Nitrophenyl)porphyrine

two-leg cis: 5,10-Bis(3,5-di-tert-butylphenyl)-15,20-Bis(Nitrophenyl)porphyrine

two-leg trans: 5,15-Bis(3,5-di-tert-butylphenyl)-10,20-Bis(Nitrophenyl)porphyrine

3.3.2 Pyrene: Pyridylethynyl functionalized pyrenes

tetra-pyrene: 1,3,6,8-Tetra(4-Pyridylethynyl)pyrene

cis-pyrene: 1,8-Bis(4-Pyridylethynyl)pyrene

trans-pyrene: 1,6-Bis(4-Pyridylethynyl)pyrene

Pyrene molecules, first investigated in 1973 [77], are 4 ortho-fused carbon rings to result in a rhombic structure. As many other π conjugated systems they show interesting optoelectronic properties like [30, 45, 84, 88, 98] and assembly was investigated [32, 100, 115, 117]. Here they are used to investigate the influence of the number and position of functional groups on these properties. The very same species have been investigated on Cu(111) albeit data adsorbed on *h*-BN/Cu(111) was lacking up to this point. The nano-patterning effect of the *h*-BN substrate is used here to modulate the wide band gap of the species and therefor their optical properties.

3.3.3 Helicene: Cyano functionalization of helicenes

Dicyano-dibenzo-[5 helicene]: 7,8-Bis(cyano)-Dibenzo-helicene

Helicenes were first synthesized 1950's [109]. They consist of ortho condensed carbon rings that form a spiral due to overcrowding in their center. While they first drew attention due to their fluorescence properties [149], helicenes are interesting molecules

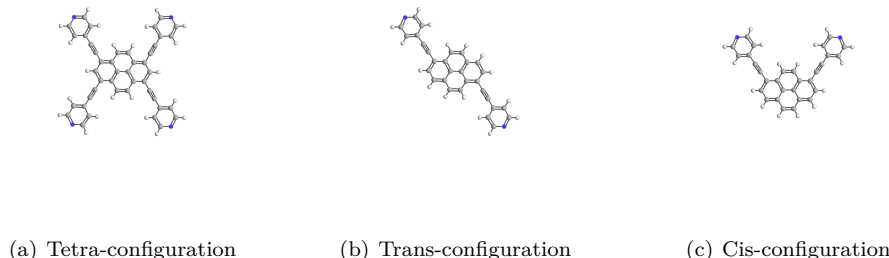


Figure 3.13: Pyridyl-Pyrene molecules in trans- (b) and cis- (c) and tetra- (a) configuration

Table 3.7: Evaporation and degas temperatures used for different molecules.

Name	Configuration	Degas [°C]	Evaporate [°C]
TPCN	—	—	490
TBP	single	4 h @ 200 °C	390
	cis	—	400 °C
	trans	4 h @ 200 °C + 1 h @ 270 °C	370 °C
pyrene	cis	2 h @ 180 °C	
		+ 1 h @ 200 °C + 10 min @ 235 °C + 1 h @ 220 °C	250
	trans	1 h @ 230 °C	265 °C
DCDB	—	1 h @ 100 °C to 150 °C	
	—	+10 min @ 170 °C + 25 min @ 200 °C + 40 min @ 220 °C	220 °C to 240 °C



Figure 3.14: DCDB on copper surface. (a) Top view, (b) side view

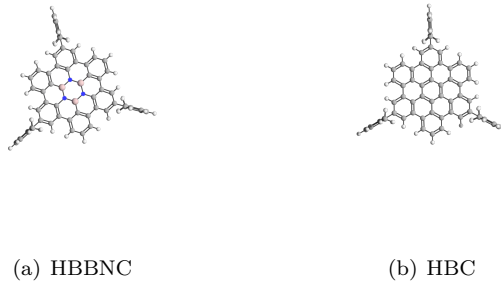


Figure 3.15: (a) HBBNC and (b) HBC

because of their chiral feature. Two different turn directions exist, left and right. The molecules investigated in this work are functionalized with two benzene rings at positions ____ and two cyano groups at positions seven and eight. For more information, please refer to ??.

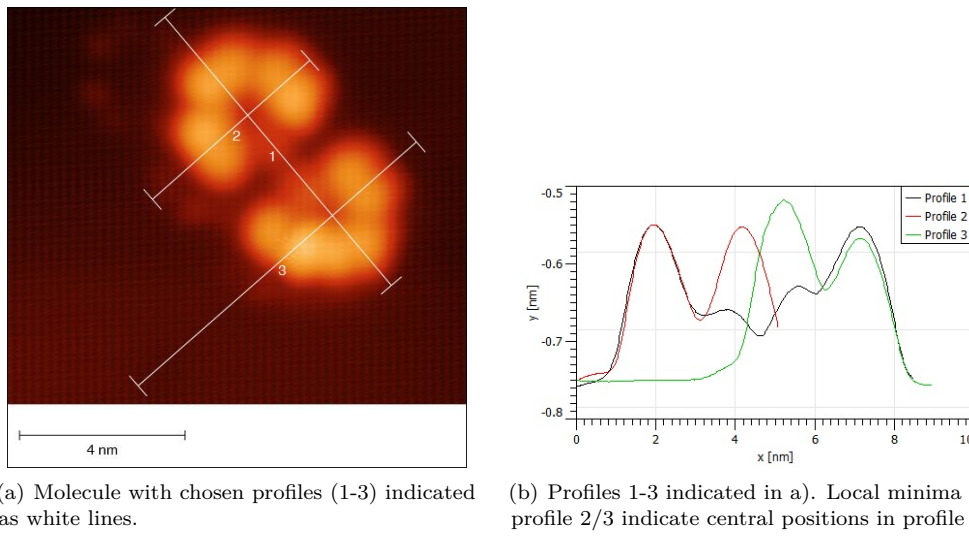
3.3.4 Coronene: HBBNC and HBC

HBBNC: 2,8,14-triptyl-hexaphenyl borazinocoronene

HBC: 2,8,14-triptyl-hexabenzocoronene

While in 2015[83] and 2016 [25] hexy-peri-Hexabenzoborazino coronene (HBBNC) was synthesized, its bad solubility prohibited experiments. In 2017 the synthesis [40] of a soluble, BN-doped coronene derivative by substitution of the central carbon ring was successful. By using HBBNC the HOMO-LUMO band gap could be widened and shows blue-shifted emission properties[40] compared to its all-carbon counterpart. Investigations with STM are performed on Au(111) [83]. Here the central $(BN)_3$ core is oriented to point all nitrogen atoms towards the leg functionalization. Due to the different electro negativity of the atomic species adsorption of gases in the central part can be interesting effects to look out for. In this thesis we focused on the geometric properties of this molecule first. Please refer to ?? for detailed information.

How to determine molecules' distance To determine the distance between molecules, one has to carefully choose the points of interest. As a problem of STM imaging the contour of the molecules sometimes appears as more or less fuzzy shape. There is no sharp edge that one could take as start or end point of the profile. Therefore the center of the molecule is often used as reference point to measure the distance between two molecules (compare fig. 3.16). As the molecule has a square footprint, one can use the center in one direction (along profile 2/3) to determine the center in the other direction (profile 1). As one can see the three profiles match leading to a consistent center of the dimer. This is also shown as depression in profile 1.



(a) Molecule with chosen profiles (1-3) indicated as white lines.

(b) Profiles 1-3 indicated in a). Local minima in profile 2/3 indicate central positions in profile 1.

Figure 3.16: Sketch of how to determine the distance between two molecules. As the molecule is square (with the exception of one direction, one can determine the center of the molecule by comparing two 90 degree rotated profiles. Profile 1 goes through the symmetry axis, while profile 2 and 3 intersect profile 1 at the center. As the profile 2 and 3 look the same when starting at the butyl groups, one can use the depression in profile 2 and 3 to determine the center of the molecule in profile 1.

4 Epitaxial hexagonal boron nitride on copper foils

- Challenges in mass production (example)

Ease of use

Costs

How to overcome (example)

For this reason, we focused on the use of cheap substrates to achieve the very same functionality as on expensive single crystals. In this chapter the foils are first etched and prepared for investigation in AFM (4.1), SEM (4.1) and STM (4.1).

4.1 Pre-treatment of Cu-foils: Polishing

Experiment realization The first attempt to etch the Cu-foil was performed with the 5%_{vol} EG, 25%_{vol} H₂O filled up with phosphoric acid. The etching was performed in a 200 ml beaker, filled with 150 ml etching solution. The setup is as depicted in Figure 3.4(a). The potential was adjusted to be 1.2 V after some minutes. The current through the solution changes and is typically highest when the etching process started.

After some minutes, the foil starts to change. The reflectivity changes, making the foil - shiny before etching - a little dull. After some additional time the foil begins to reflect light better again. This is the moment where the etching process is interrupted. The time inside the etching solution depends on the handling (like shaking the beaker or moving the foil in the solution - but was usually $\geq 2\text{ h}$).¹

ADD IMAGE from acutal setup

One has to be careful if reproducible results are needed. During the etching process (as more and more copper settles on the counter electrode), the current and therefore the etching rate decrease continuously. When the beaker is moved, some of the debris on the electrode changes (the electrode's) surrounding and the etching rate (limiting current) increases again. Front- and backside of the foil are suspect to different etching rates. The back side is generally more flat, the side facing the counter-electrode always shows some additional protrusions.

ADD IMAGE from polished foils

After etching treatment The foil is taken out and cleaned from remaining etchants with purified water first and isopropanol afterwards. Foils are stored in isopropanol to avoid oxidation.²

¹Since the perfect voltage/current to perform polishing varies in time a automated etching process has been developed [111]

²To further improve the quality of the foil, one can follow the documented recipe for annealing the foil in a H₂ atmosphere (10 sccm, 1000 °C, 30min)[79] to increase the copper grain size and further smoothen the surface. We decided to further prepare the foils within the UHV chamber and skipped this step.

So prepared foils are investigated in XPS (compare figure 4.9) - (discussion of peaks can be found inside the text. Comparable experiments are performed by [138, p. 8]). After the etching process one foil is investigated in SEM. It was stored for one day in isopropanol and blown dry with nitrogen.

SEM Invented in the 1930's by Manfred von Ardenne[4], Scanning electron microscopy (SEM) is another versatile tool for the experimentalist. In contrast to (LT-)STM and AFM, SEM is capable of imaging huge areas of the sample within a very short time, which allows for a vast overview as well as good statistics. Magnifications reach up to 500k and above, illustrating even features in the order of 1 nm.

As the name already discloses, SEM scans the surface with electrons. Their interaction with the material are diverse and some of them are explained in the following. While all effects are present in every measurement, not every microscope features detectors for all of these. While detectors for secondary electrons are standard equipment others may be not.

The primary electrons are created with a filament. These often consist of tungsten (metal, high melting point, low work function). Alternatives are lanthanum hexaboride (LB_6) - often used in LEED setups, too - or zirconium oxide. Electrons are accelerated (typical energies are within 1 keV to 40 keV) and focused on the specimen surface in a spot with few nm diameter with condenser lenses. Scanning the surface is achieved with coils that deflect the electron beam and therefore the actual scanning spot.

When the electrons hit the surface, they interact with the specimen in a small volume. The volume depends on the electron's energy, the atomic number Z of the specimen and the specimen's density. It is typically in the order of 0.1 μm to 5 μm .

Drawbacks:

- Sample has to be mounted → no in-situ measurement, surface alteration in between
- Rather "dirty" vacuum → surface alteration while measuring
- Measurement destroys sample → adsorbate build-up due to chemical reaction below e-beam

One can see (Figure 4.1) that the surface imaged in different intensities which correspond to the different orientation of the copper grains within the foil[153]. The grain size may range from just a few μm to several hundred μm and in some cases even mm. The grains are separated by grain boundaries. Large grains are preferred for growing graphene on copper foils because grain boundaries are subject to inhomogeneities within the graphene layer and provide a route for unwanted surface chemistry (copper oxidation for example). These effect can be also be used to highlight grain boundaries as shown in [153].

Although not very rough, the copper foil shows surface variation. While some areas of the sample show some wavy surface, whereas other are much flatter and appear in a different intensity (Figure 4.2).

Neither estimation on the grainsize nor guesses for their absolute orientation have been done due to the lack of EBSD-data in the SEM setup.

AFM Figure 4.3 shows the striations that stem from the production process (from top to bottom). After etching ($U = 1.2\text{V}, I=120\text{ mA}$ to 250 mA) for 5 h in a solution (shown in table 3.5) the striations have gone and the RMS value decreased by 30 % to 45 % and an increase in foil quality is obvious even with bare eyes. Figure 4.3 and 4.4 show AFM images in the same size and contrast - before and after etching. The circular hole is an

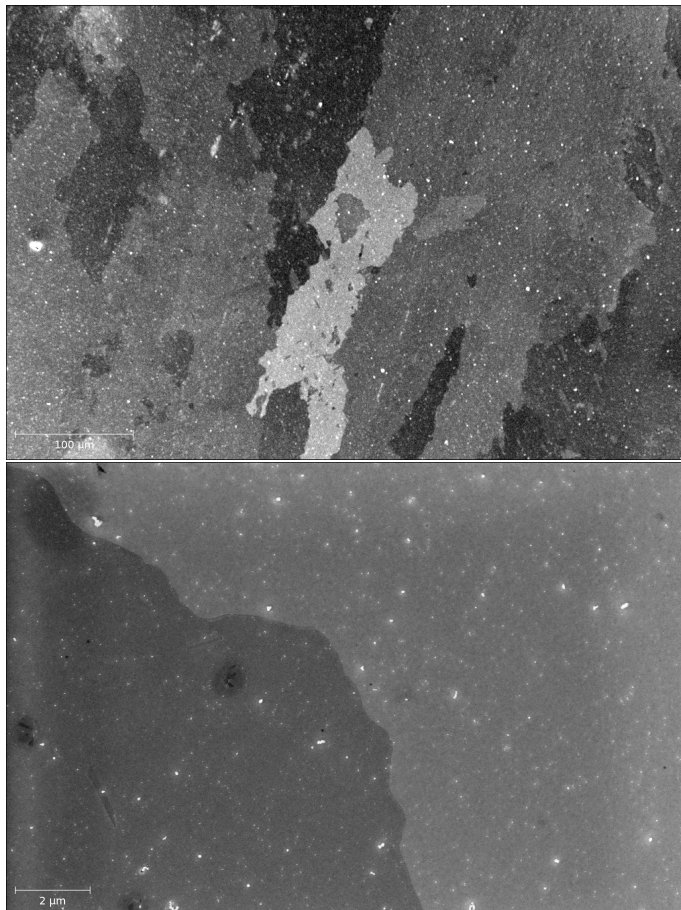
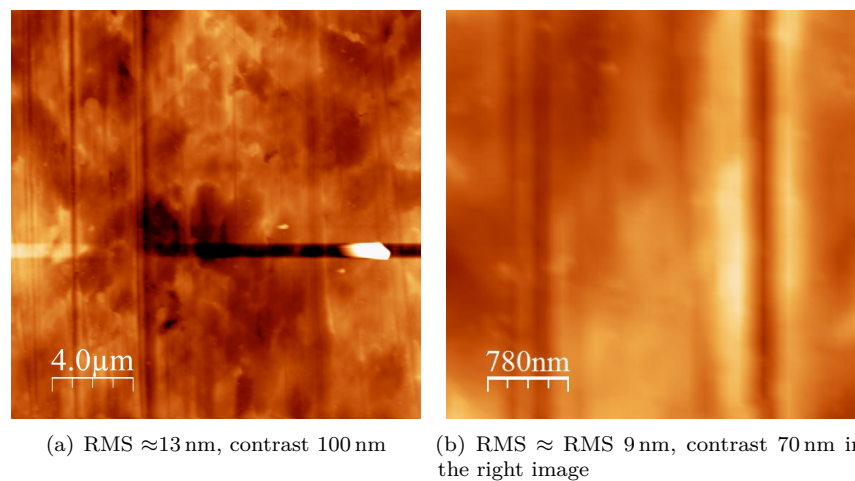


Figure 4.1: SEM image of etched copper foil. Different contrast suggests different grain-orientation within the surface. a) Larger ($570 \mu\text{m} \times 380 \mu\text{m}$) image showing the contrast of different grains in the copper-foil, b) zoom ($18 \mu\text{m} \times 12 \mu\text{m}$) to a area with two different contrasts and their border.



Figure 4.2: SEM image that shows different surface morphologies (5.6 μm x3.7 μm)



(a) RMS \approx 13 nm, contrast 100 nm

(b) RMS \approx RMS 9 nm, contrast 70 nm in the right image

Figure 4.3: AFM image of the 0.25 mm copper foil as bought from alfa aesar.

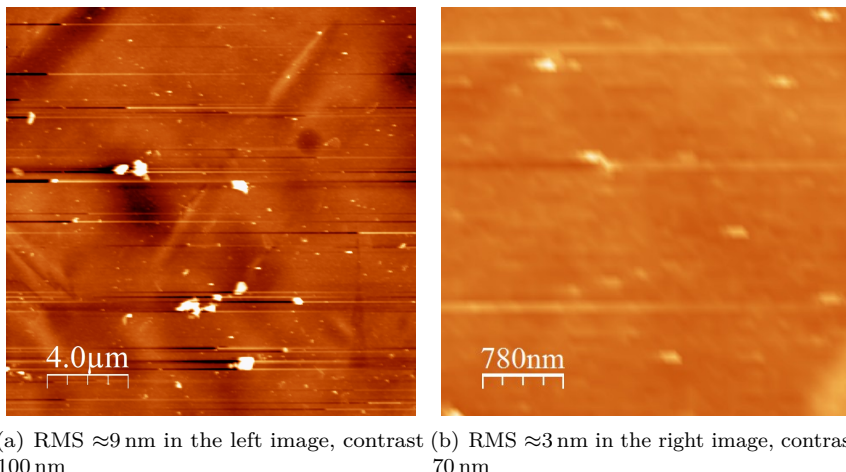


Figure 4.4: AFM image of a copper foil polished 5h (according to table 3.5)

effect of bubbles in the etching process where the bubble affects the rate of etching. The over all structure changes from a heterogenous sample height to a flat height contribution with only a little amount of defects. Those are sufficiently seperated in space to exhibit flat regions where the h-BN may grow unperturbated.

not done yet - maybe future? Some foil has been mechanically polished with 4k paper and several hours of Syton polishing. The roughness of these samples has been investigated also in AFM. These are comparable to the chemically polished ones, but are always slightly higher by \approx 10%. Sometimes unwanted new scratches appear after mechanical polish.

STM The bought and chemically polished foils are mounted on a sample holder and loaded into the load lock. It is evacuated for 2 h to 3 h, afterwards the valve is opened to the chamber. During transfer, no noteable increase in the base pressure is noted. The sample is put on the parking slot.

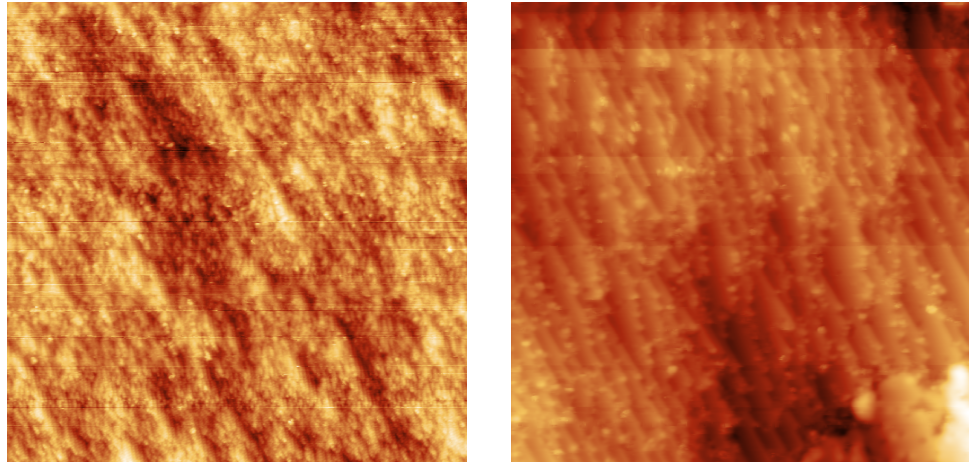
The sample was initially degassed with slowly increasing temperatures to remove adsorbates like CO , CO_2 and H_2O .

After some time of degassing, the sample was prepared with repeated sputter and anneal cycles. The annealing temperatures were increased up to 800 °C. After that procedure, the sample was cooled down and observed in STM.

4.2 Characterization: SEM & STM of *h*-BN on Cu-foil

Further experiments were carried out to increase the cleanliness of the *h*-BN on the polycrystalline copper foil. To reduce the amount of elements coming from the body of the foil, it is repeatedly sputtered and annealed to temperatures as high as 800 °C. This may have also an improving influence on the grain size and amount of corrugation. Several attempts have been made which are described in summary below.

- After cleaning, the sample is investigated in STM. The foil shows a inhomogeneous topography, with parts of the sample showing very flat regions while others still remain heavily corrugated and not scan able in STM. A first look onto the quite



(a) A flat area of the cleaned copper foil with no larger corrugation is shown before *h*-BN growth. The roughness is 70 pm.

(b) STM image after 4 L of borazine dosage on a 800 °C hot copper foil surface. A small *h*-BN island can be seen (lower right) on a largely uncovered copper foil background.

Figure 4.5: Cu-foil after repeated sputtering and annealing cycles (a) and after CVD growth of a sub-ML *h*-BN (b). Imaging parameters: (a) 3.6 V, 0.1 nA, color scale 0 pm to 600 pm, Image width: 88.6 nm, (b) 1 V, 0.37 nA, color scale 0 pm to 900 pm, Image width: 44.3 nm.

heterogeneous surface reveals flat areas with a typical roughness of ≈ 70 pm exist (Figure 4.5(a)). Areas with very large corrugations ≥ 100 nm are hard to scan in STM and bad places for *h*-BN growth. Although being flat, the polycrystalline foil shows a lot of unordered substrate steps and a dirty surface, covered with adsorbates imaged as small bright dots.

- Before dosage the sample was kept at 800 °C for 10 min. Borazine was dosed for 5 minutes with a pressure of 1×10^{-7} mbar with the sample kept at temperatures of 850 °C. Afterwards the sample was kept at this temperature for another minute.
- The sample was sputtered and annealed several times to temperatures of 800 °C. Before the dosage it was held 5 minutes at 750 °C. Borazine was dosed with the same pressure as before (1×10^{-7} mbar) but for 1min and at a lower temperature of 750 °C. After the preparation the sample was kept at 750 °C for another 1 minute. It was cooled down slowly (shown in figure 4.7(a)).
- The foil was sputtered and annealed 4 times with temperatures of 800 °C. Borazine was dosed at 2×10^{-7} mbar for 2.5 min. The sample was kept at this temperature for another 5 minutes after dosing. The sample was cooled down slowly. Figure 4.7(a) shows some of the grown islands. The copper surface changes upon *h*-BN growth and the terrace width increases below the *h*-BN flakes. The typical faceting of the surface vanishes or can at least not be depicted because of the overgrowing *h*-BN (Figure 4.7(b)). Due to nearby tip forming, the right side of the image is decorated with adsorbate, most likely from the tip itself - they appear as bright white spots in the image.

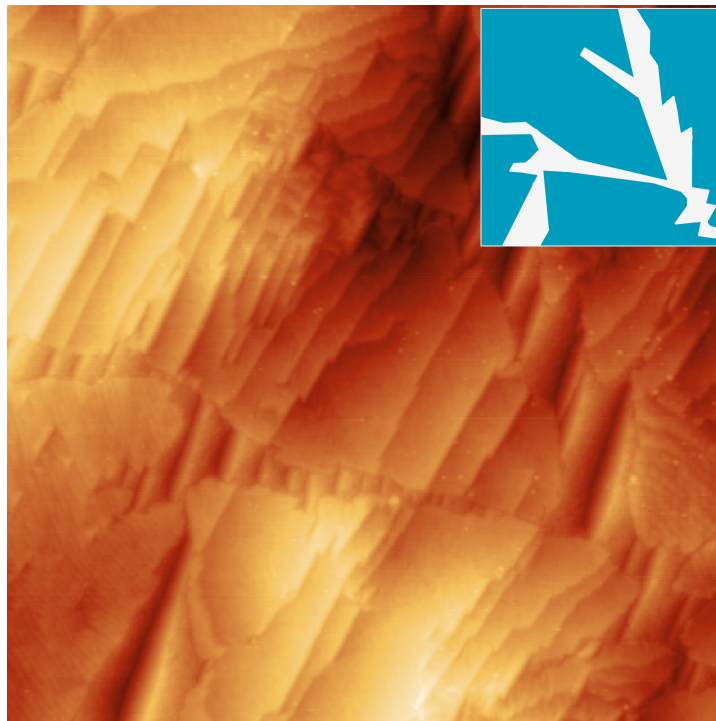


Figure 4.6: STM image of 22 L borazine dosed on a 800 °C hot copper-foil surface. Several large islands can be seen that grow over Cu-foil step edges. Inset shows coverage with *h*-BN ad layer in blue. Imaging parameters: 4.7 V, 0.2 nA, color scale 0 nm to 7 nm, Image width: 295 nm.

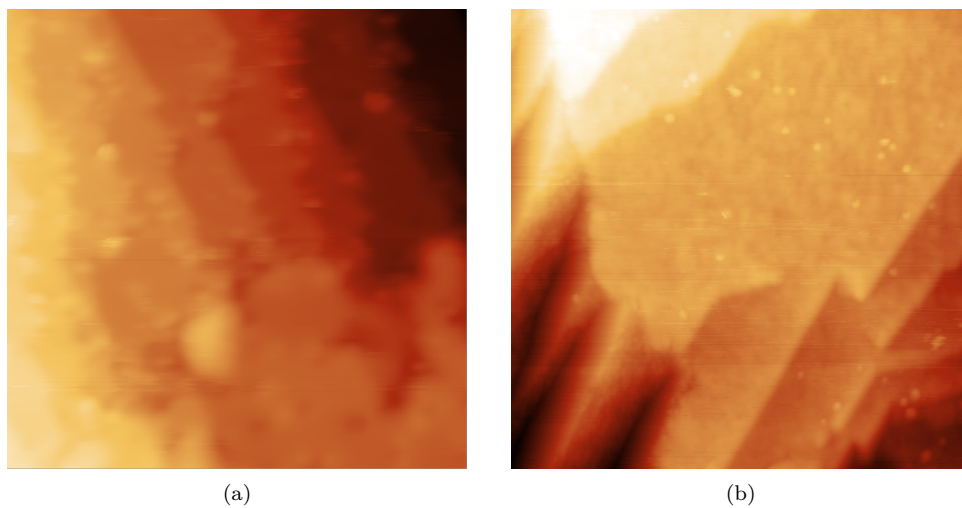
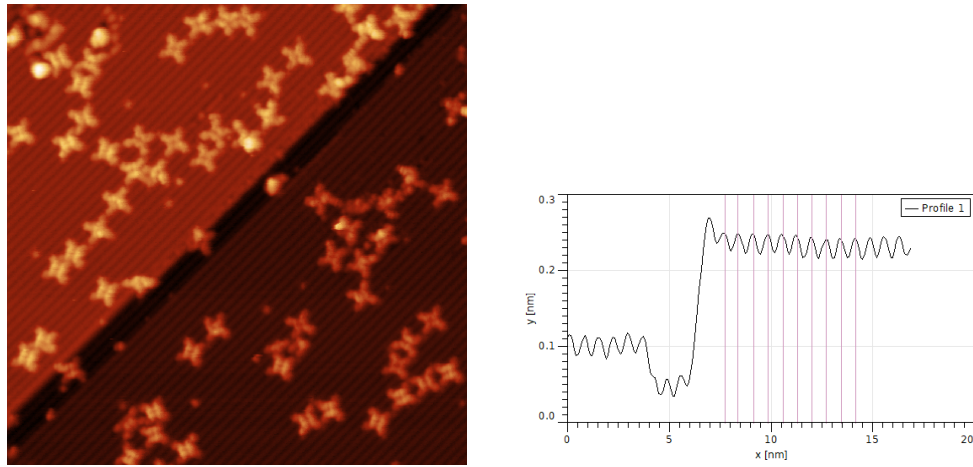


Figure 4.7: STM topographies of *h*-BN islands that overgrow Cu-foil facets. Imaging parameters: (a) 1 V, 0.37 nA, color scale 0 nm to 1.5 nm, Image width: 18 nm, (b) 3.5 V, 0.5 nA, color scale 0 nm to 4 nm, Image width: 73.8 nm.



(a) Molecules on copper foil surface - supposed to be covered with h-BN, maybe just free (maybe faceted) copper

(b) Line spectrum across the step shown in ?? perpendicular to the trench. No molecules were crossed.

Figure 4.8: funny surface structure - oxygen over layer (2x1)? - cu reconstruction? - maybe some very small (0.75 nm) linear moire on a Cu(100) facet? Noise can be excluded due to the fact that the stripes do not occur on the molecules, but only on the substrate. Many deformed molecular cores visible → strong substrate interaction → no h-BN! Line spectrum shown in ?? Imaging parameters: (a) 1.26 V, 0.04 nA, color scale 0 nm to 0.8 nm, Image width: 40 nm

points to point out:

- Look at Messzeit-April.ppt power point presentation
- Stufenhöhe
- Beschaffenheit der stufen/facetts → material transport mechanism/strength differs under the h-BN compared to the bare cu-foil surface.
- Wechselwirkung BN-Wachstum und Facettenbildung

surface structure of h-BN on Cu-foil During experiments some “new” structure appeared (compare figure 4.8). The apparent height change between the both terraces is 130 pm separated by a slim trench that is slightly lower than the right terrace (50 pm). The parallel stripes have an apparent corrugation of 25 pm and are separated 70 pm from each other and covering the whole image.

The adsorbed TPCN molecules show different apparent heights in their molecular center.

insert graphics!

4.3 Characterization: XPS of self-grown h-BN/Cu-foils

Copper foils with 0.25 mm were bought and repeatedly sputtered/annealed. Several growth cycles of h-BN via CVD of borazine were done. The sample is transferred to the XPS-STM chamber and again sputtered/annealed several times to clean it properly.

The needed dosage of borazine to assemble a full monolayer of *h*-BN is derived via a combined STM/XPS measurement. Several preparations were done to understand the growth behaviour of *h*-BN on the copper foil. Coverages are measured in STM while the chemical composition of the sample was assessed with XPS.

Table 4.1: Determination of the full monolayer borazine dosage. First a certainly saturated sample was prepared (I) and measured in XPS/STM. A sub-monolayer (II) was grown and compared to the monolayer STM and XPS results.

Prep.	Position	Area [arb.u.] [eV]	FWHM (XPS)	Anode Element	Dosage [L]	Coverage (STM)
B1s	I	191.1	3776	1.35	Mg	4736 100 %
	II	191.1	1994	1.35	Mg	789 53 %
N1s	I	398.7	5875	1.45	Al	4736 100 %
	II	398.6	3183	1.43	Al	789 54 %

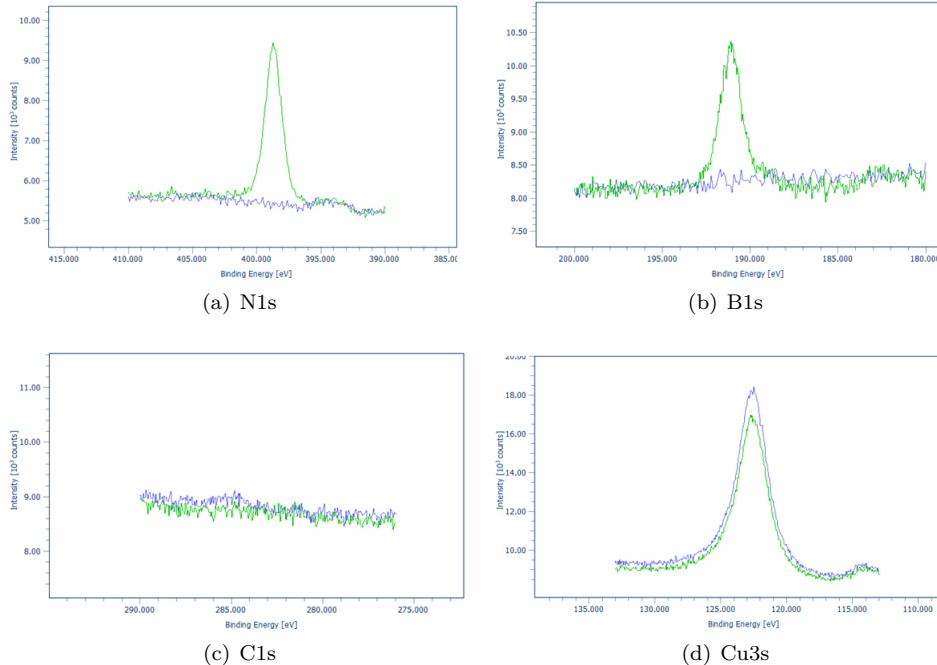


Figure 4.9: **REDO! Axis too small!! Check layout with other XPS measurements!!** XPS spectra for ML *h*-BN/Cu-foil. The peaks are at their expected positions[78] and show no additional features. No remnants of sulfur or remaining oxygen could be found.

When comparing the resulting coverage (STM coverage/XPS signal) (II) to the (saturated) monolayer (I) one can derive the minimal amount of borazine needed to process a monolayer of *h*-BN on the copper foil. Comparing the coverages of a sample grown with CVD, 7×10^{-6} mbar for 15min (I) and one grown with CVD, 3.5×10^{-6} mbar for 5min (II), shows that reducing the dosage by a factor of 6 does not reduce the coverage by a factor of 6, but just by a factor of 2. Therefore (I) features a full monolayer and (II) only

half of it. It follows that a full monolayer may be achieved by dosing 1500 L borazine on a 800 °C hot copper foil surface. Because the growth rate may certainly not be linear (less and less free copper surface to decompose borazine into building fragments while the layer assembles) the given dosage is a minimum estimation to achieve the monolayer.

Even though a much larger amount for borazine (4736 L) than needed for a monolayer (1500 L) has been dosed, the maximum coverage did not exceed the XPS signal of a monolayer. So the growth of *h*-BN on copper foil is self-limited (as in the case of many h-BN/metal systems) to a full monolayer. It is not possible to achieve layer growth with this type of preparation.

T and t dependence is not subject to investigation because the growth is supposed to follow the same mechanisms as on the single-crystal case. Quite some investigation has been done, [110, 118] to understand this process and literature has matured.

4.4 Characterization: XPS of bought *h*-BN/Cu-foils

The quality of the as-bought *h*-BN on copper foils[52] is examined in XPS. The XPS spectra shows contribution of different atomic species. There are peaks for the O-atoms (1s: 529 eV to 535 eV)), C-atoms (1s \approx 285 eV), N-atoms (1s \approx 398 eV), B-atoms (1s \approx 190 eV) and Cu-atoms ($3p_{1/2,3/2}$: 70 eV to 80 eV)). One would expect the shape of the 1s-peaks to be singlet-like (one peak, gauss shaped) and the 3p-peak to be a doublet (two close lying peaks with area-ratio 1/2:3/2=1:2).

O1s Position varies with temperature. The signal at room temperature(black) stems from adsorbed water and CO. These desorp with increasing temperature(blue). When going to higher temperatures(red) this peak increases again and shifts to higher binding energies. Not present in self-grown *h*-BN (figure 4.9)

C1s The C1s Peak decreases with increasing temperature and retains its position. This has the same reason as for the O1s peak (desorption of CO due to the heating). Some of the carbon remains on the surface - even at temperatures as high as 970 K.

N1s/B1s The nitrogen/boron peaks show some temperature related changes. There is little change upon annealing to 630 K, both peaks shrink, but stay almost constant in their position in binding energy (slightly shifted to lower binding energies by about 0.2 eV). Position is [N1s: 398.1 eV | B1s: 190.2 eV]

Cu3p The copper peak exhibits an increase in area when increasing the temperature. This is because some of the water and CO adsorb and more and more copper is contributing to the signal. This peak is a doublet, so both signals come from the same chemical copper surrounding.

The $Cu(OH)_2$ O1s peak is expected to be at 531.3 eV to 531.7 eV[33] which may explain the shoulder of the O1s peak to higher binding energies (O1s metal: 531 eV). Nitrates (NO_3) have binding energies in the range from 532.5 eV to 533.5 eV[150, p. 45]. This would imply either an replacement of nitrogen with oxygen, or some kind of oxygen on top or below the nitrogen in the BN. As proven by Simonov et al. in [137] the (!atomic!) oxygen tends to replace the nitrogen in the *h*-BN/Ir(111) system when it is annealed to 600 °C (compare figure eight therein). Thus it forms $B_xN_yO_{1-x-y}$ over-layers. The longer the oxidation time the higher the amount of replaced nitrogen (figure two therein). If this effect is responsible for the O1s peak at high temperatures is questionable, since

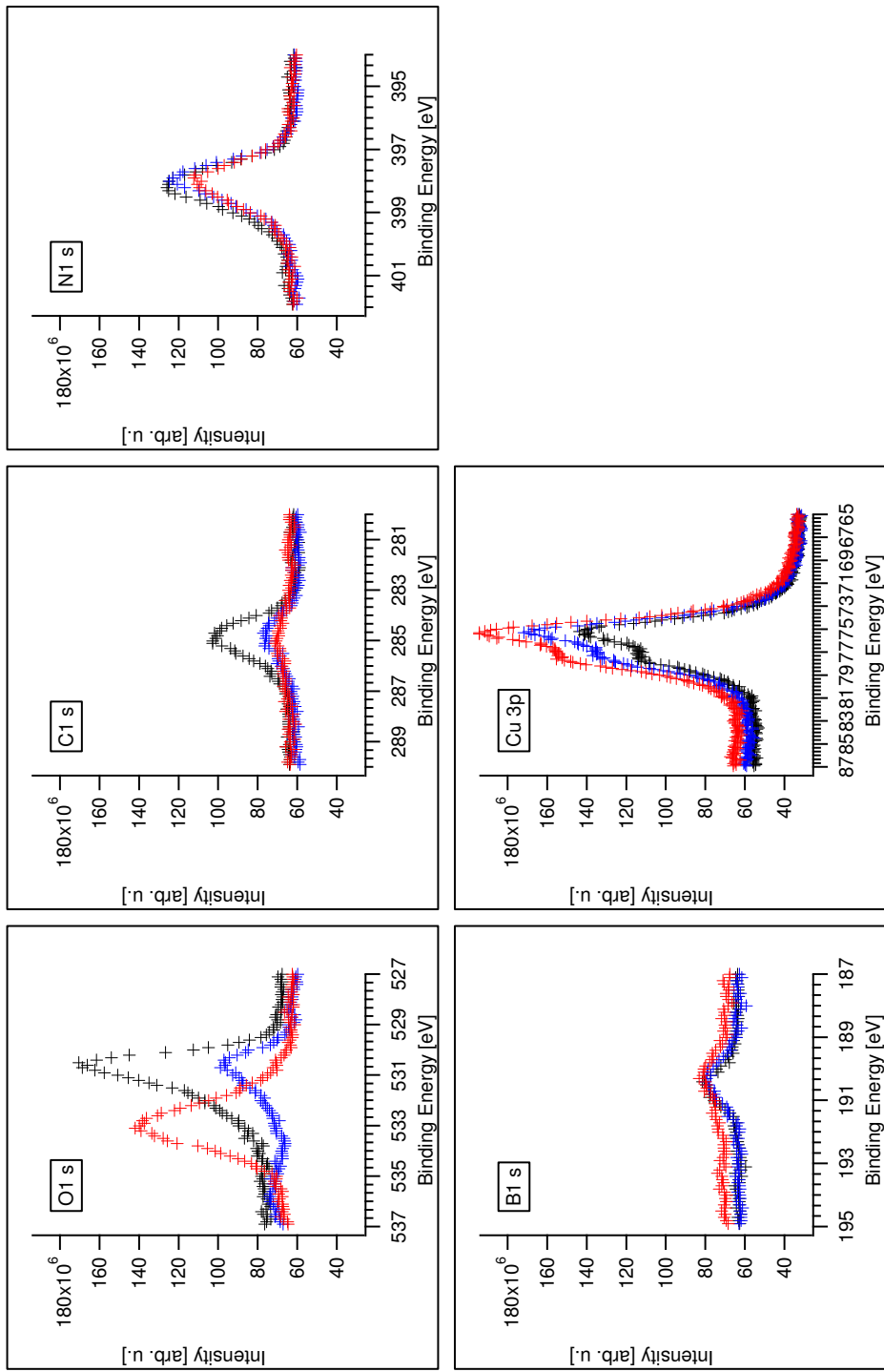


Figure 4.10: XPS spectra of as-bought *h*-BN/Cu-foil sample[52]. All spectra are taken at room temperature in as-bought state (black) and after annealing to 630 K (blue) and 970 K (red).

the oxygen has to be cracked somehow - where no process can be thought of (no catalytic cracking at metal surface possible - full ML, thermal energy to low to reach binding energies of O_2 (no citation here, nothing found - just a guess)).

An exchange of O with B or N would be easily visible in XPS (due to changed N/B surroundings. Not sure if the signal of oxygen is large enough for that. Check DATA - confirm maybe

4.5 Application: Molecular functionalization with TPCN

The Cu(111) support for the h-BN growth is replaced by a polycrystalline copper foil. The goal is to achieve the same ordering of molecules on the h-BN surface. The h-BN layer has been prepared by a dose of 5×10^{-7} mbar borazine for 20min (4500L). During dosage the foil has been kept at 820 °C.

When a h-BN spacer layer is introduced, the molecules decouple from the substrate, lowering their interaction with the afore-mentioned. This can be seen in a change of the molecules' footprint (rectangular → square).

They do not form ordered networks (like chains or squares) and lie rather loosely on the h-BN layer (compare 150807.142226.dat). They can easily be moved with the STM tip (1V, 10nA). In some areas, denser TPCN islands form. Here they lie right next to each other, each slightly shifted to match the neighbouring molecules and to achieve the dense packed regions. The same motif was already investigated in the same system [148].

During scanning ($I=0.1\text{ nA}$, $0.9\text{ V} < U < 1.3\text{ V}$) of a group of molecules, a single molecule could be pushed out of the group (compare figure 4.11). While the chain initially consisted of 3 molecules in a row, after scanning one of the molecular units moved to the left while the remaining two stay at their positions. A closer look to the moved molecule's geometry reveals deformation of the legs.

It was shown that the imminic nitrogen species within a 2H-TPP molecule strongly interact a Cu(111) surface, thus orient along high symmetry directions. [18, 34, 38, 49, 58, 123] Rotation and diffusion are limited.

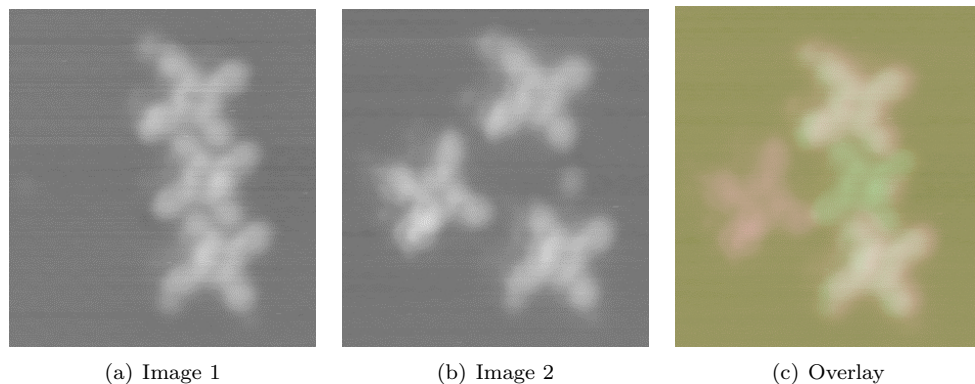
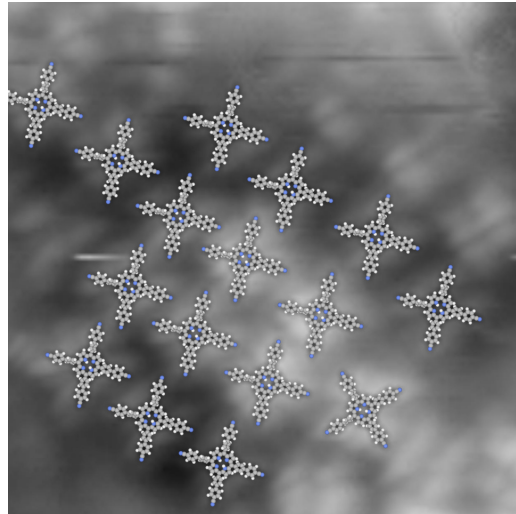
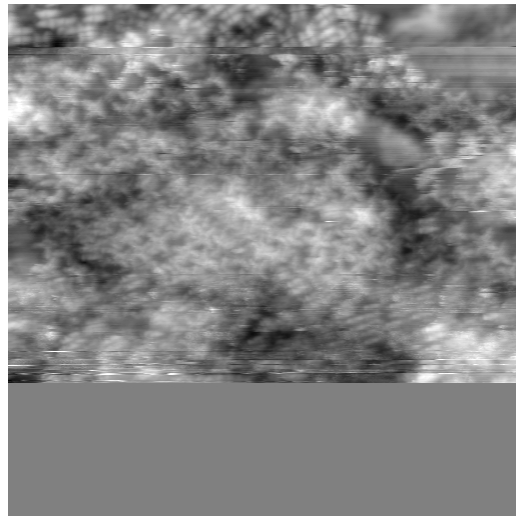


Figure 4.11: Position change of TPCN group members. Central molecule is manipulated, color indicates its initial (a, green hue in c) and final (b, red hue in c) position. Image (c) is created via an overlay of two sequential images. The upper and lower molecules do not shift thus sharing the same color.



(a) Loosely ordered molecules on the h-BN/Cu-foil surface.



(b) Molecules do not always show ordering but in dense areas they do.

Figure 4.12: There they form a motif like in figure 4.11a).

TPCN without added cobald form similar pattern on the h-BN/Cu-foil system (compare fig. 2b in [148]). Although the ordered areas were quite rare, an ordered region has been found. Here the molecules are not strictly equi-distant or -rotated which makes it difficult to give an accurate unit cell for this type of motif.

Adding Co Introducing some cobald (15min, 90 °C) in the system, this self-assembly changes. The molecules now form a 2D network, too, but are further apart. Their only connection point to the other molecules is the tip of their legs pointing to the adjacent leg of the neighbouring molecule.

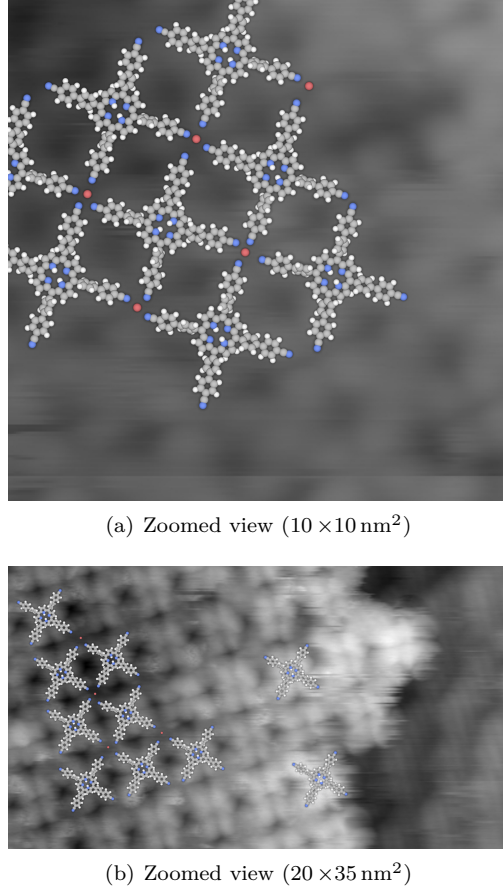


Figure 4.13: Self-Assembled monolayer for TPCN on h-BN/Cu-foil. The cobald atoms sit right in between the molecules and faciliate a regular, ordered arrangement of the TPCN.

No sign for metallation (brighter center of porphine core) or cobald adatoms (bright spots in between the molecules) is observed. Because this type of binding is already reported [148], similar binding mechanisms are derived for this system.

Molecules arrange periodically with center-center distances of about 2.3 nm. This leaves a little void space in between 4 TPCN molecule's legs, space where a Co atom may be located. This would result in a distance of 1.5 Å between the end of a TPCN leg (its N-center) and the center of the cobald atom. Typical binding distances for Co-NC are reported [120, 129] and in good agreement.

5 Tert-Butyl-Phenyl Porphine

Within this section, TBP molecules with are investigated. The number (1-2) and position (single-, cis-, trans-configuration) of the very same functional group is changed. Although first the results on metal surfaces are presented, one of the ideas of the following experiments is to use the dipole moment of the single functionalized molecule to orient it along the work function change of a *h*-BN/Cu(111) sample. Please refer to section 3.3 for detailed information on these molecules.

Preparations with the single nitro functionalized species are done at RT on Cu(111), *h*-BN/Cu-foil and Ag(100). The Ag(100) preparation was heated to 170 °C.

Preparations with the trans functionalization are performed at RT on Ag(100) and Cu(111) where the last was heated to 120 °C.

Evaporation of the cis functionalization were not performed, although tried intensively no molecules were sublimated in the OMSE and found on the sample. This indicates strong intermolecular interaction within the crucible like cluster formation or polymerization, which have to happen before the molecules sublimate.

5.1 Single leg functionalization

5.1.1 on Cu(111)

When adsorbed at room temperature, TBP distributes equally on the surface, forms unordered islands and decorates step edges. Molecules orient their main axis (connecting line from one di-tert-butyl-phenyl ring across the center to the nitrophenyl ring) along the dense packed substrate rows most often, less are 15° of ((Refer to image?)). Several binding motifs (as shown in Figure 5.2) are observed, namely

- A dimer, where molecules lie “head-to-head”, functional groups (NO_2) pointing at each other
- A “triangle”, where molecules are rotated 120° and functional groups point towards a shared center. Although this motif does not occur very often (or at least under very flexible angles), it is given as an example where the functional groups point to each other. Similar motifs (like 3 molecules in 90° are observed together with other orientations.
- Chains with different length appear, where the nitro group of molecule 1 points to the di-tert-butyl group of molecule 2 (“head-to-tail”). At the connection points, molecules appear brighter, promoting a physical overlap of the two molecules.

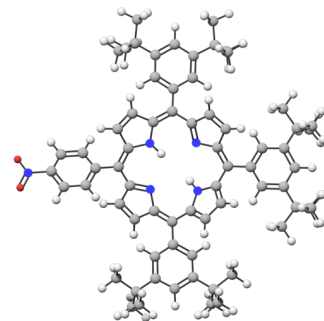


Figure 5.1: TBP with three di-tert-butyl and a single nitro phenyl group added at the meso position.

Center-center distances are typically 1.78 nm (for the head-to-tail) and 1.5 nm for the head-to-head connection.

“head-to-head” To model the occurring binding motifs, deformations of the molecules have to be taken into account. Because nitro groups face each other in the “head-to-head” connection, their distance would be too small to facilitate a similar binding mechanism like for the TPCN on copper (where copper surface ad atoms promote binding between nitrogens), so no free space between the facing nitro groups is observed. Because the distance is so small, the phenyl ring (with attached nitro group) rotates by 45°, to make the phenyl ring stand upright. When the second molecule does the same, both match each other with negligible lateral shift, reproducing the STM images best. Similar binding motifs are reported in [74] for non-covalent cross linking of dicarboxylic acids in hydrogels. Although the situation on a metal-surface may change considerably (only 2D - no 3D, metal present - will change chemistry), the observed binding motif matches very well.

“head-to-tail” The chain motif “head-to-tail” is reconstructed using the unique contrast of the TBP molecule. When the center-center distance is measured, molecules are modeled that distance away from each other. These models show a physical overlap between molecules, which is not possible because of steric hindrance. To solve the problem, the nitro-group (head) of one molecule is rotated by 35° out of the plane (like pulling the nitro-group upwards, not rotating the group left/right).

Flexible tert-butyl-groups Another interesting fact is that butyl groups of TBP seem to orient themselves (as far as steric hindrance allows for) along the dense packed rows of the copper substrate. Again, one has to be careful when reconstructing geometrical information from STM images. Like the distortion of legs in the TPCN molecule, this rotation can be explained by a rotation of single butyl groups. Although the phenyl ring remains at the same position/rotation, tert-butyl groups are allowed to rotate such that they appear in different heights. Because STM (constant current) follows equipotential lines, the whole phenyl-di-tert-butyl-complex looks rotated in plane, although it may not be. This is confirmed in literature[60, 61].

5.1.2 on Ag(100)

Molecules are adsorbed on Ag(100) at RT. The resulting conglomerates are shown in Figure 5.4(a). The very most surface area is covered with unregular patterns. The step edges are covered, assuming a sufficient large mobility at RT to move from the terrace to the nearest step edge. The only free step edges observed are due to tip formings on the sample surface since these are created after the molecules are stuck on the surface because of the low temperatures during measurement.

Annealing The RT adsorption is annealed to 170 °C for 10 min and investigated in LT-STM again (Figure 5.4(b)). No big changes are visible, neither in the formation of new assemblies nor in the distribution of molecules at terraces or at step edges. No chain formation could be observed.

Assembly Since no regular self-assembled islands are present on the surface, more detail is put on the only repeating binding motifs on this surface. One of this configurations resembles a cross (??), while the second one is a variation of the dimer motif (Figure 5.5).

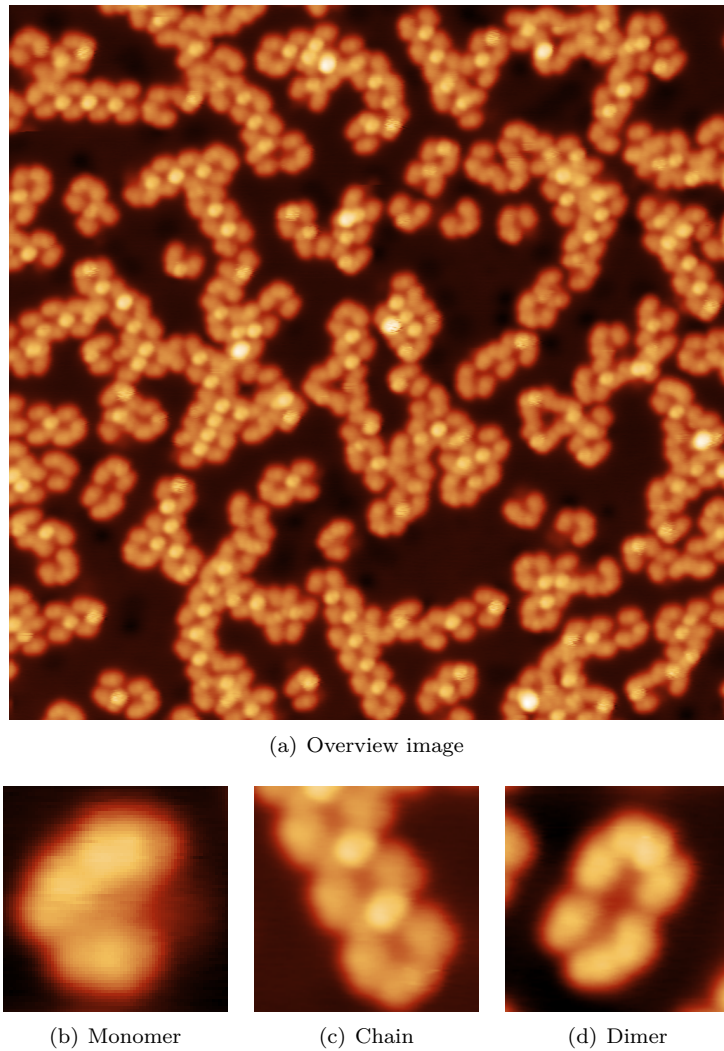


Figure 5.2: RT adsorbed single nitro functionalized TBP on Cu(111) and their most abundant binding motifs. (a) Each of the binding motif can be found as well in the overview STM data, as well as in the enlarged images (b-d). All images recorded with -500 mV , 0.1 nA , color scale 0 pm to 300 pm . Image width: (a) 44 nm , (b) 3 nm , (c) & (d) 5 nm

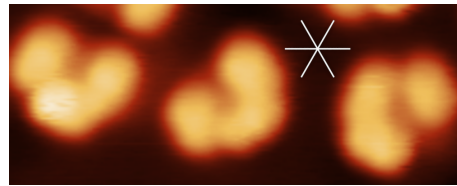


Figure 5.3: Different appearances of TBP on Cu(111). While most of monomers (center in image above) show even heights with their tert-butyl functions, some (left) do possess an elevated tert-butyl group. The orientation of the tert-butyl groups is aligned with the high symmetry crystal direction (indicated by white lines) most often. Image recorded with -500 mV , 0.1 nA . Image width: 10 nm

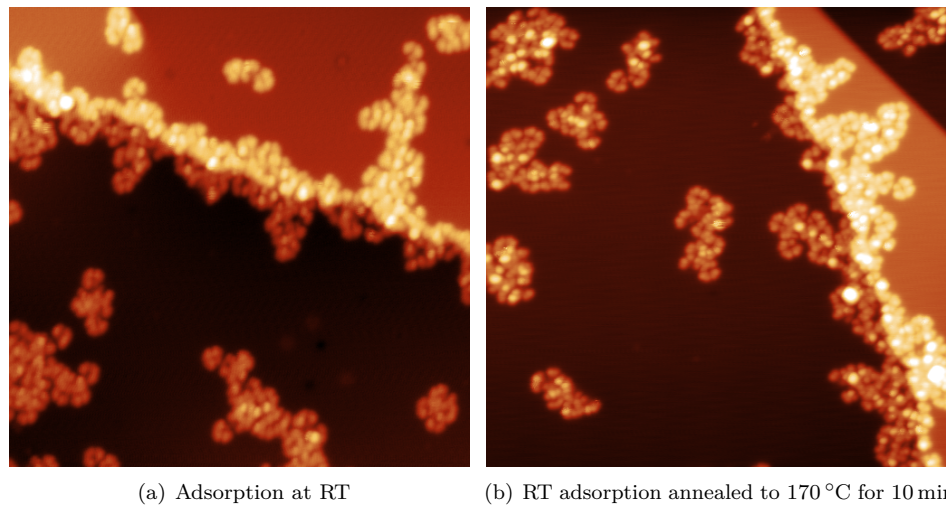


Figure 3.4. Annealing after RT adsorption of molecules on Ag(100). (a) STM data of molecules adsorbed at RT (Scan parameters: $U_b = 1$ V, $I_t = 0.03$ nA), (b) After annealing for 10 min to 170 °C (Scan parameters: $U_b = 1$ V, $I_t = 0.1$ nA). Color scale 0 pm to 600 pm. Image width: 44 nm.

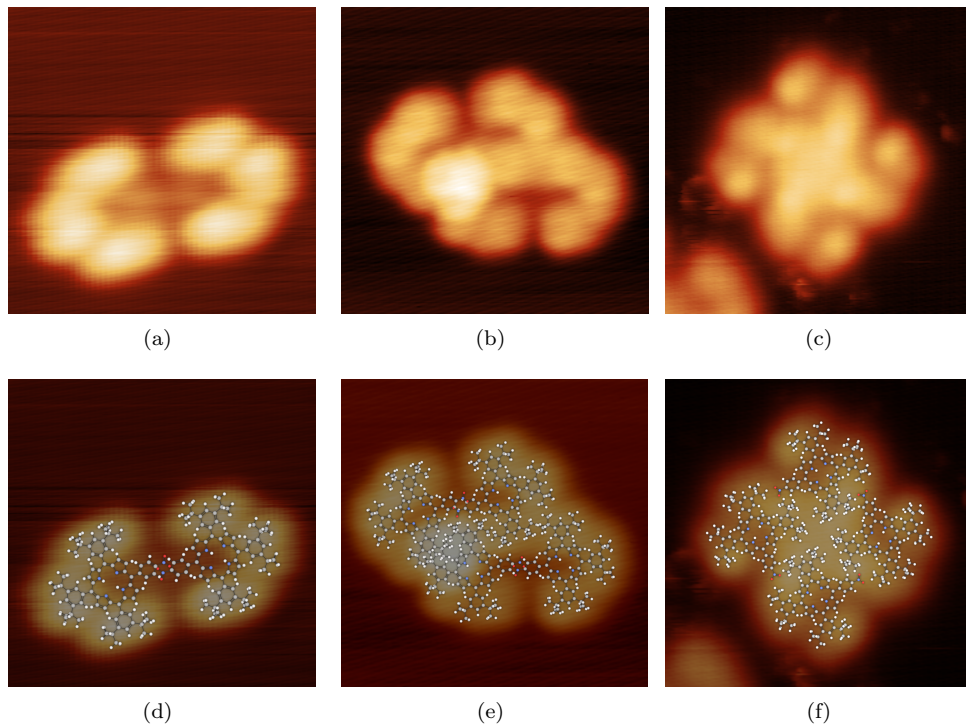


Figure 5.5: Different observed binding configurations of TBP adsorbed on Ag(100) at RT.

(a) STM data of dimer configuration. Scan parameters: $U_b = 0.328$ V, $I_t = 0.035$ nA, Image width: 5 nm. (d) Model representation. (b) STM data of two coalescent dimers. Scan parameters: $U_b = 0.097$ V, $I_t = 0.035$ nA, Image width: 6 nm. (e) Model representation. (c) A cross consisting of four TBP molecules. Scan parameters: $U_b = 2.3$ V, $I_t = 0.035$ nA, Image width: 10 nm. (f) Model representation. Color scale in all STM images 0 pm to 300 pm

While on copper, two molecules may form a dimer in head-to-head or head-to-tail configuration, on silver some form tetramers from two parallel merged dimers. While one dimer looks like two “U”’s with facing open ends ($\in \ni$), the other dimer is shifted to closely match the first dimer best and lies parallel.

Another motif looks like a cross and shown in ???. Build out of four molecules, where each is rotated by 90° with respect to its preliminary neighbor. One can distinguish four di-tert-butyl groups from the central cross. Although there is no atom directly in the center, the cross looks bright in its center (in STM), which is somehow counterintuitive.

Flexible Tert-Butyl-Functions Figure 5.5(b) shows an interesting feature of the tert-butyl functions.

- Butyl groups within TBP feature different contrasts (look rotated), while the orientation of the butyl-groups doesn’t follow the close packed substrate rows.
————— find image and explain
- TBP molecules have been heated on silver substrate for 10 min at 170 °C. The resulting sample did not feature chain-formation or improved ordering.

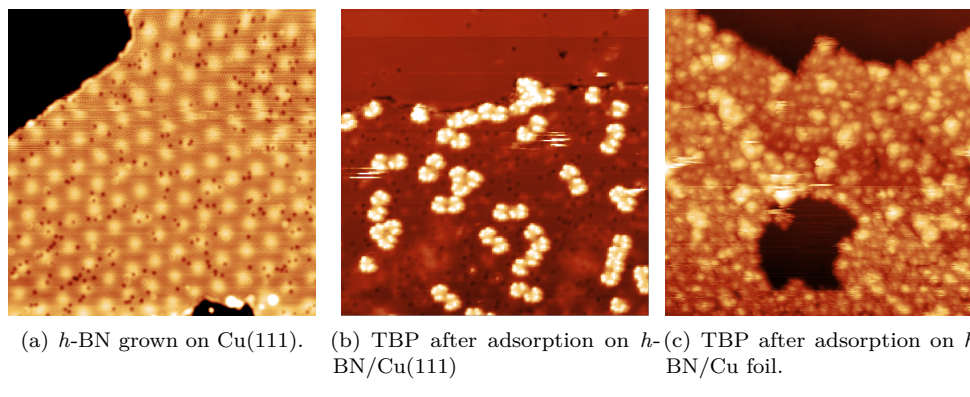


Figure 5.6: STM topographs of *h*-BN grown on copper with subsequent molecular adsorption. (a) shows a *h*-BN layer grown on Cu(111) by CVD. (b) shows the sample after evaporating TBP molecules at RT. (c) shows empty *h*-BN islands grown on the polycrystalline copper foil and molecules on a copper terrace. Scan parameters: (a) $U_b = 2.273\text{ V}$, $I_t = 0.048\text{ nA}$, color scale 0 pm to 100 pm. (b) $U_b = 1.074\text{ V}$, $I_t = 0.033\text{ nA}$, color scale 0 pm to 300 pm. (c) $U_b = 2.585\text{ V}$, $I_t = 0.032\text{ nA}$, color scale 0 pm to 1500 pm. All images are 40 nm wide.

Spectroscopy Some spectroscopy could be achieved that shows different typical features for different areas in the molecule. Note that the spectra were done for molecules sitting on a Ag(100) surface. There is a clear indication, that the macrocycle of the molecule contributes to the broad peak in the dI/dV data at around 1 V, while the nitro groups dominate the spectra at around 600 mV. Look at the corresponding .pptx file for the spectra and the corresponding IGOR-files dimer/quatermer1-2 for the spectra.

5.1.3 on *h*-BN

***h*-BN grown on Cu(111)** Further experiments have been done to investigate the behavior of TBP on *h*-BN. When adsorbed on *h*-BN/Cu(111), molecules show a high mobility that makes the molecules move away from the *h*-BN islands. Some molecules could be resolved at defects or close to the perimeter of the *h*-BN islands. This is in line with other observations for adsorbates ((CITATION)). Adsorption temperatures as low as -170°C have been used to lower the molecules' energy pool, but diffusion to free metal areas occurs and no molecules remain on the *h*-BN surface.

***h*-BN grown on Cu-foil** Molecules adsorb on the BN surface and STM imaging is hard due to molecules that can be moved on the rather 'slippy' surface of the insulating BN. Nevertheless some agglomerations of the molecules leave free BN spots where no molecules are. As the preparation of the BN should result in a closed BN layer on top of the Cu-foil no movement of molecules to free Cu areas should be observed, making these free regions BN regions. Why the molecules are not distributed homogeneously on the BN remains topic to speculation. Spectroscopy has been tried intensively but without

reproducible results. Unlike the adsorption on Ag(100) and Cu(111) no formation of di- and quaterners has been observed.

5.1.4 Conclusion

The driving force for orienting the whole molecule on the surface remains speculative. On Ag(100), neither an orientation of the molecules main axis with respect to the substrate, nor a orientation of butyl-groups along the dense packed substrate rows can be seen - which again favors Cu-substrate interactions as dominant role. When the copper is exchanged with silver to act as substrate, TBP behaves quite different. Although the distribution is homogeneous on the surface, the interaction between molecules look different. While on copper the most abundant binding motif is the head-to-head dimer, this motif does not appear on silver as often as on copper. Two other motifs emerge on silver. The interaction between the butyl-phenyl groups is considered to be van der Waals like [66], stabilizing the conglomerate.

5.2 Double leg functionalization

5.2.1 on Cu(111)

When depositing trans-TBP on Cu(111) at room temperature no long range ordering can be achieved. The molecules arrange rather arbitrarily as can be seen in Figure 5.7(a).

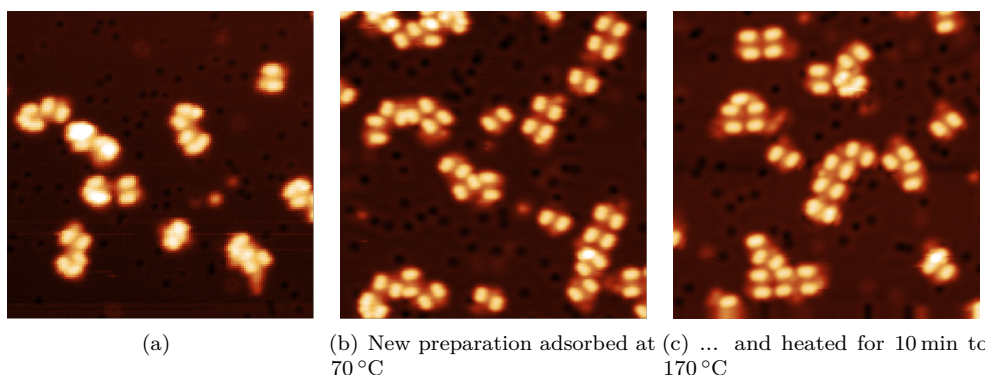


Figure 5.7: Molecules adsorbed on Cu(111) at RT and subsequently annealed to different temperatures. (a) Adsorption at room temperature did not show extended long range order. (b) Adsorption at 70 °C and (c) annealing to 170 °C for 10 min improves the chain length slightly. All images are 40 nm wide. Scan parameters: (a) $U_b = 1.2 \text{ V}$, $I_t = 0.041 \text{ nA}$, (b) $U_b = 0.5 \text{ V}$, $I_t = 0.038 \text{ nA}$, (c) $U_b = 0.522 \text{ V}$, $I_t = 0.021 \text{ nA}$

The molecules tend to connect in a defined angle to its next neighbor, forming different binding motifs. These are predominantly different kind of chain formation (see figure 5.8).

- The molecules are ordered such that they form a straight chain (Figure 5.9(a)).
 - The molecules arrange in chains, but each molecule has an offset of about a half of its width to the next neighbor or the molecules attach in chains, but show a kink.

Figure 5.8(b)

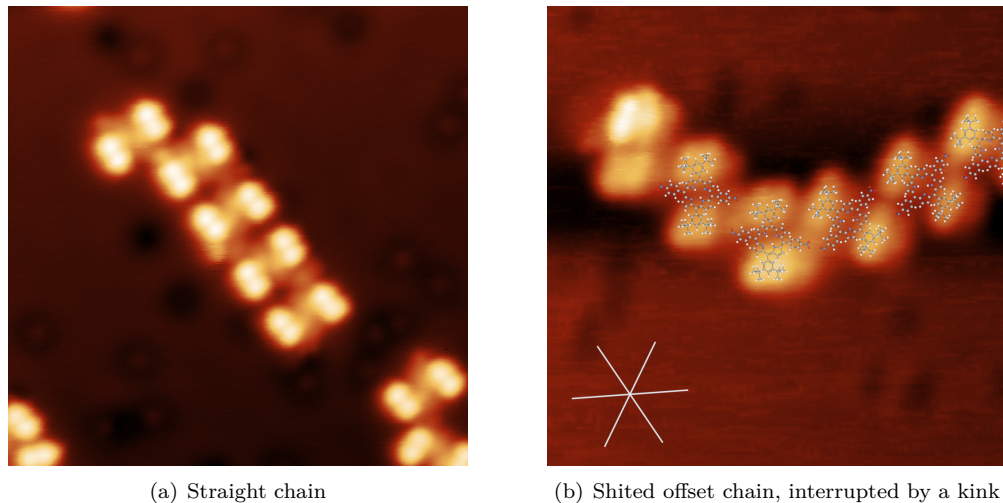


Figure 5.8: All motifs exist at every temperature, although the chain length increases with temperature. It also looks like the chains are getting more offset- and kinked-like chains than at lower temperatures.

During modeling Figure 5.9 several points became clear.

- First consider the even apparent height of the di-tert-butyl groups. It indicates that both groups in a legs have comparable heights and it is likely that the phenyl ring bearing these groups is rotated for an even alignment of the tert-butyl groups with regard to the substrate level.
- Orientation of di-tert-butyl phenyl groups is the same within a single molecule but alternates (by $\approx 10^\circ$) in neighboring molecules in a chain. This is indicated by blue and green lines in Figure 5.9(a), each representing a common orientation.
- Second the minor contrast variations in the central porphine core change as the orientation of the di-tert-butyl-groups. Free base porphine core is likely to adsorb with its axis - formed by opposing nitrogens in the core - aligned parallel to the dense packed crystal direction[124]. In the present case, the molecule is lifted from the substrate by the bulky di-tert-butyl groups. Hence the porphine core interaction with the crystal substrate is considerably lower than in the 2H-P case. Still, every second molecule has the same orientation, while neighboring molecules are rotated by 30° .
- The gap between di-tert-butyl-phenyl groups of neighboring molecules is larger on one side of the chain than on the other and shows a larger apparent height (white arrows in Figure 5.9(a)). Although identification of surface ad-atoms is not straightforward with an STM, they are believed to originate from the copper surface.

The best fitting model consists of molecules with a center-center distance of 1.9(1) nm
Having a closer look to the nitro groups, one recognizes a close proximity of these to each other. Also note the light protrusions in between two adjacent molecules' butyl

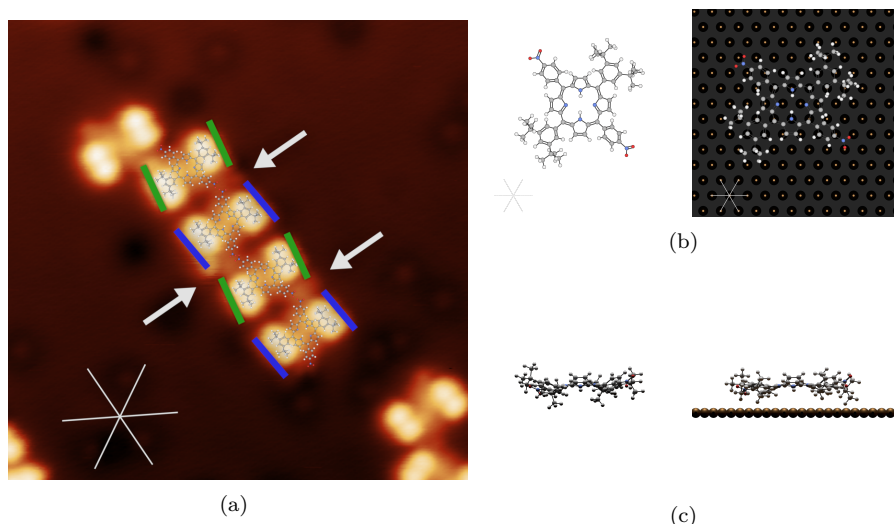


Figure 5.9: Straight chain binding motif on Cu(111). (a) shows an STM image together with the dense packed row indication of the substrate (white lines). Colored bars indicate the rotation of the di-tert-butyl-groups. Arrows point at places where ad-atoms are considered. (b) Top views (6 nm wide) showing the molecules geometry in gas-phase (left) and after adsorption and assembly (right). Although the exact adsorption site is not known, it is considered to be on a bridge site as for 2H-P/Cu(111). (c) Side views of above shown configurations.

groups (adatom?). If the legs are rotated by just 15° , the nitro groups would point to these protrusions. This rotation costs not much energy and is about 25 kJ/permol ((**please cite something, value is for rotated phenyl ring at a porphine core I guess**)). Considering these protrusions as Cu-ad atoms (already occurred in chapter ?? as protrusions in between TPCN chains which may change their position in discrete position in the molecule.) This Cu-ad atom may direct the binding of the nitro groups towards it, making them bend outwards. The position of the copper atom itself may rely on its registry to the substrate - preferring a threefold coordination site as known for copper (**citation**)).

The second motif is a chain motif, too. Orientation of molecular axis and dense packed substrate atom rows are the same and again the di-tert-butyl groups orient along them. The difference is a lateral offset between the molecules to shift each of them by half a molecules width. The center-center distances are 1.9(1) nm. It is harder to quantify a possible orientation of the nitro-phenyl groups, since as well straight as well as bended configurations match the assembly. In this binding motif, stable connections between molecules are most likely due to nitro-phenyl groups pointing to di-tert-butyl groups and therefor stabilizing the assembly.

5.2.2 on Ag(100)

Unit cell When adsorbed on a square (100) silver surface, the molecules interestingly arrange in a trihexagonal tiling (see figure 5.10). The molecules at the perimeter of this island is nicely distinguishable and continuing their regular pattern to the center of the

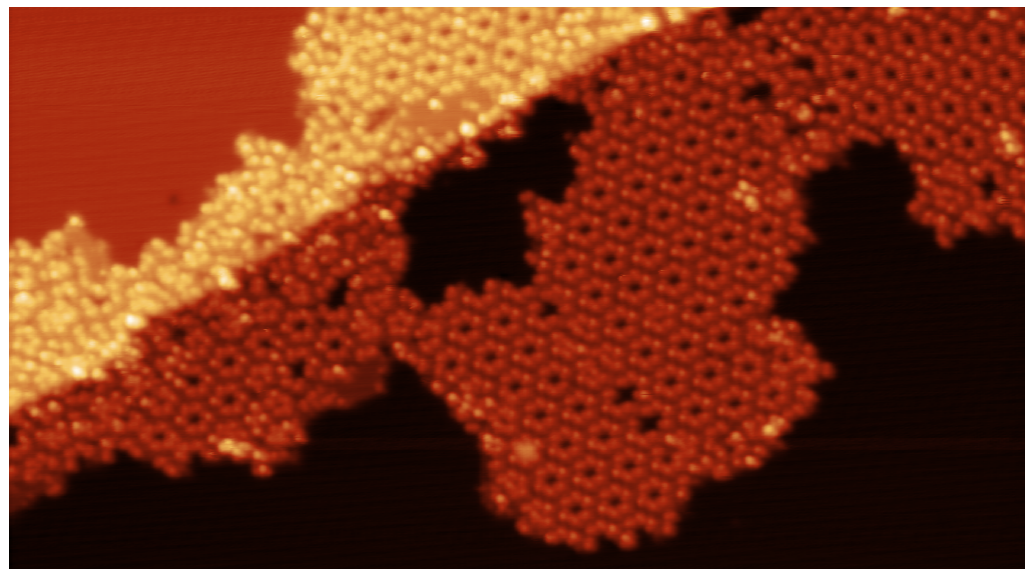
island results in an accurate description of the assembly. The unit cell is determined to be _____ and the hexagonal unit cell is shown in Figure 5.10(b), bearing three molecules.

Molecular orientation The molecules are arranged so that each molecule has one of its di-tert-butyl-groups in one hexagonal pores and the other in the neighboring one. Each pore is made up of six molecules arranged on a hexagon with _____ long edges. Each vertex is occupied by a single molecule, neighboring molecules on the hexagon are rotated by 60°. The pores are created by free space where the di-tert-butyl-groups point towards each other. The nitro-phenyl groups point towards the intermediate space where smaller triangular openings are formed. At their edges the nitro-phenyl groups connect to the neighboring di-tert-butyl groups.

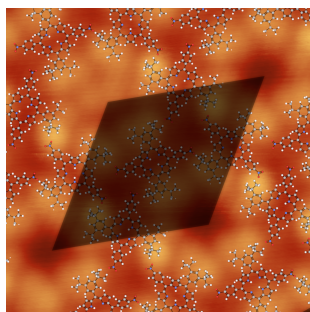
Considering a former orientation calibration on Ag(100) where the direction of the dense packed crystal direction was determined, the orientation with regard to the substrate is given as white lines in Figure 5.10(b): The long and short axis of the unit cell (marked as green cross in (b)) is almost collinear, just differing by less than 10°. Since the calibration was done with another preparation the angle calibration may not be 100 % accurate because the sample was moved in the meantime. That may result in an little angle uncertainty. Please see Figure 2 in chapter 7.1 Appendix for a detailed image.

Contrast within single molecule A closer look to the geometries in high resolution STM data gives clue to the rotation of the di-tert-butyl-groups and is visualized in Figure 5.10(c). Focusing on the STM contrast of a single molecule, one can see that it is dominated by the di-tert-butyl-groups on both sides of the molecule. These look like small triangles in the STM with a single brighter protrusion enclosed by the footprint. The bright protrusion is never on the same side of the triangular footprint thus the di-tert-butyl-groups are believed to be rotated in two different directions - lifting opposite parts of the functional group.

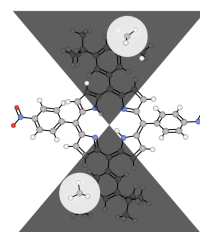
Domain boundaries The observed domain boundaries are imaged in Figure 5.11. On both sides the regular tiling is proceeded, but both are shifted with respect to each other by _____. This offset results in the wrong alignment of molecules from one domain with respect to the other domain and a discontinued growth. The resulting free area at the domain boundary is occupied by molecules from one domain that bear the wrong orientation the proceed the growth of the second domain and vice versa. This can be nicely seen in Figure 5.11(c), where the misalignment of one domain (left) with respect to the other (right) causes two cavities to open up between the two (lower image part). While these two are unoccupied and reveal the substrate, another type of cavity can be formed directly seen on top of the two aforementioned. Here the cavity is filled with a single molecule so that both di-tert-butyl groups interlock with the open cavity. Please note that some of the assembly pores are filled, too. Here the space of the pore prohibits a complete molecule to fit in, the observed adsorbates in the pores are most likely molecular fragments like tert-butyl-groups that were incorporated by the assembly during the island growth.



(a) STM topography of several islands grown next to a step edge. Areas with trihexagonal tiling as well as some domain boundaries are visible.



(b) Hexagonal unit cell with overlaid molecular models.



(c) Enlarged view on the molecules rotated di-tert-butyl-group and highest elements enclosed by brighter circles..

Figure 5.10: Trans-TBP adsorbed on Ag(100) at room temperature. (a) shows a large overview of the assembled molecules. The unit cell constituents are enlarged in (b) where parts of (a) are shown with molecular models overlaid. (c) shows a single molecule crossing a horizontal plain to emphasize high lying part in the molecule that are marked with white circles and will appear brighter in STM. All images recorded with 437 mV, 0.1 nA, color scale 0 pm to 650 pm

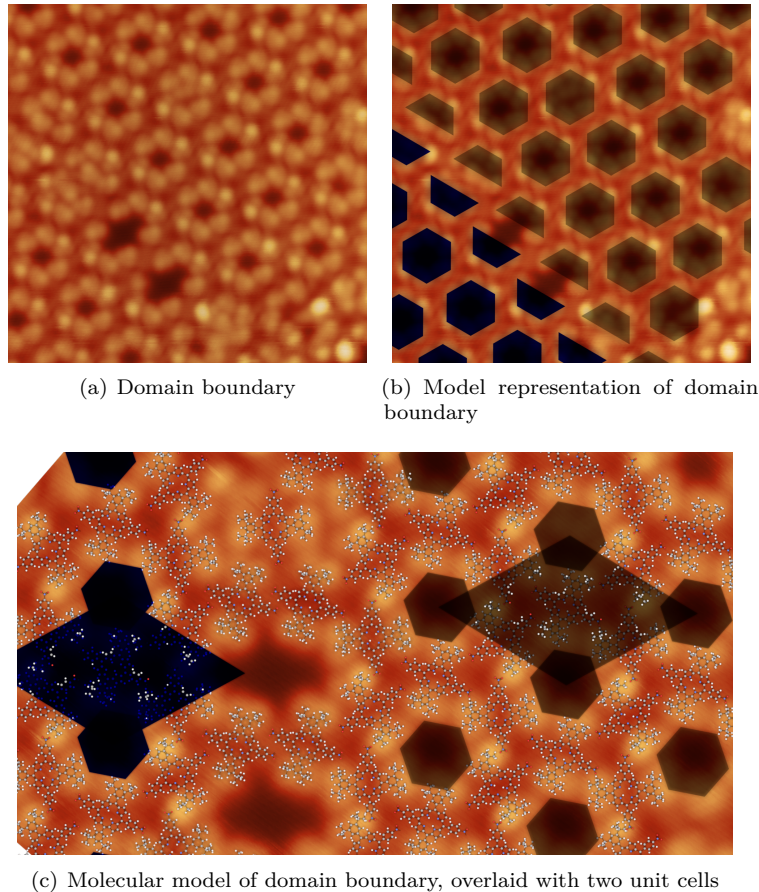


Figure 5.11: Domain boundary of trans-TBP adsorbed on Ag(100) at RT. (a) shows an overview of the domain boundary together with its model representation in (b). The assembly close by is modeled in (c) where parts of (a) are shown and molecular models overlaid. All images recorded with 1.3 V, 0.1 nA, color scale 0 pm to 650 pm

6 Hexabenzocoronene - w/o central borazine core

6.1 Find a nice title!

HBC It is reported that for HBC, no stable second layer of molecules can be found for a strong electron donor like HBC [31].

7 Unsorted

7.1 measurements without clear interpretation

This is intentionally for all nice little things which does not certainly make it into this work: [64]

Index

AFM, 9
Crystal:lattice constants, 19
electrochemical polishing, 22
 chemical reaction, 23
 Used solutions, 27
Gundlach oscillations, 8
molecules
 Coronene, 36
 Helicene, 35
 Pyrene, 34
 TBP, 33
nitro porphin, 34
SEM, 40
STM, 3
 One dimensional tunneling, 4
 Tersoff-Hamann, 5
 WKB, 5
STM:operating mode, 3
STM:resolution, 6
STS
 Barrier Height, 8
 Bias above work function, 8
 Bias below work function, 7
 modulation, 6
 Resolution, 9
XPS, 12
 Anode materials, 12
 Auger process, 13
 binding energies, 14
 chemical surrounding, 13
 Peak shapes, 14
 Physical model, 12
 quantitative analysis, 14

Bibliography

- [1] "OPEN CHEMISTRY DATABASE". Aug. 1, 2018. URL: <https://www.ncbi.nlm.nih.gov/pccompound> (visited on 08/01/2018).
- [2] Florian Albrecht et al. "Direct Identification and Determination of Conformational Response in Adsorbed Individual Nonplanar Molecular Species Using Noncontact Atomic Force Microscopy". In: *Nano Letters* 16.12 (Dec. 14, 2016), pp. 7703–7709. ISSN: 1530-6984, 1530-6992. DOI: 10.1021/acs.nanolett.6b03769. URL: <http://pubs.acs.org/doi/10.1021/acs.nanolett.6b03769> (visited on 08/23/2018).
- [3] Claire Antoine et al. *Alternative Approaches for Nb Superconducting Cavities Surface Treatment (Invited paper)*. Jan. 1999.
- [4] Manfred von Ardenne. "Das Elektronen-Rastermikroskop". In: *Zeitschrift für Physik* 109.9 (Sept. 1938), pp. 553–572. ISSN: 0044-3328. DOI: 10.1007/BF01341584. URL: <http://link.springer.com/article/10.1007/BF01341584> (visited on 04/05/2016).
- [5] W. Auwärter et al. "XPD and STM investigation of hexagonal boron nitride on Ni(111)". In: *Surface Science* 429.1 (June 1999), pp. 229–236. ISSN: 00396028. DOI: 10.1016/S0039-6028(99)00381-7. URL: <http://linkinghub.elsevier.com/retrieve/pii/S0039602899003817> (visited on 10/23/2014).
- [6] Willi Auwärter et al. "Controlled Metalation of Self-Assembled Porphyrin Nanoarrays in Two Dimensions". In: *ChemPhysChem* 8.2 (Feb. 2, 2007), pp. 250–254. ISSN: 14394235, 14397641. DOI: 10.1002/cphc.200600675. URL: <http://doi.wiley.com/10.1002/cphc.200600675> (visited on 08/21/2018).
- [7] Willi Auwärter et al. "Porphyrins at interfaces". In: *Nature Chemistry* 7.2 (Feb. 2015), pp. 105–120. ISSN: 1755-4330. DOI: 10.1038/nchem.2159. URL: <http://www.nature.com/nchem/journal/v7/n2/full/nchem.2159.html> (visited on 11/12/2015).
- [8] Willi Auwärter et al. "Synthesis of One Monolayer of Hexagonal Boron Nitride on Ni(111) from B-Trichloroborazine (ClBNH)₃". In: *Chemistry of Materials* 16.2 (Jan. 2004), pp. 343–345. ISSN: 0897-4756, 1520-5002. DOI: 10.1021/cm034805s. URL: <http://pubs.acs.org/doi/abs/10.1021/cm034805s> (visited on 10/15/2014).
- [9] Alan R. Battersby. "Tetrapyrroles: the pigments of life". In: *Natural Product Reports* 17.6 (2000), pp. 507–526. ISSN: 02650568, 14604752. DOI: 10.1039/b002635m. URL: <http://xlink.rsc.org/?DOI=b002635m> (visited on 08/21/2018).
- [10] R. S. Becker, J. A. Golovchenko, and B. S. Swartzentruber. "Electron interferometry at crystal surfaces". In: *Physical review letters* 55.9 (1985), p. 987. URL: <http://journals.aps.org/prl/abstract/10.1103/PhysRevLett.55.987> (visited on 07/17/2015).
- [11] Wi Hyoung Lee Bin Zhang. "Low-temperature chemical vapor deposition growth of graphene from toluene on electropolished copper foils." In: *ACS nano* 6.3 (2012), pp. 2471–6. ISSN: 1936-086X. DOI: 10.1021/nn204827h.

- [12] G. Binnig et al. “Tunneling Spectroscopy and Inverse Photoemission: Image and Field States”. In: *Physical Review Letters* 55.9 (Aug. 26, 1985), pp. 991–994. DOI: 10.1103/PhysRevLett.55.991. URL: <http://link.aps.org/doi/10.1103/PhysRevLett.55.991> (visited on 07/22/2015).
- [13] Gerd Binnig et al. “7x7 reconstruction on Si (111) resolved in real space”. In: *Physical review letters* 50.2 (1983), p. 120. URL: <http://journals.aps.org/prl/abstract/10.1103/PhysRevLett.50.120> (visited on 07/16/2015).
- [14] Dawn A. Bonnell, ed. *Scanning tunneling microscopy and spectroscopy: theory, techniques, and applications*. New York, N.Y: VCH, 1993. 436 pp. ISBN: 978-0-89573-768-7.
- [15] D. Briggs and J.C. Rivière. “Spectral Interpretation”. In: *Auger and X-ray Photoelectron Spectroscopy*. Ed. by D. Briggs and M.P. Seah. Frankfurt am Main: Otto Salle Verlag GmbH & Co., 1990.
- [16] D. Briggs and M.P. Seah, eds. *Auger and X-ray Photoelectron Spectroscopy*. Frankfurt am Main: Otto Salle Verlag GmbH & Co., 1990.
- [17] Léon Brillouin. “La mécanique ondulatoire de Schrödinger: une méthode générale de resolution par approximations successives”. In: *Comptes Rendus de l'Académie des Sciences* 183 (1926), pp. 24–26.
- [18] Florian Buchner et al. “Diffusion, Rotation, and Surface Chemical Bond of Individual 2 H -Tetraphenylporphyrin Molecules on Cu(111)”. In: *The Journal of Physical Chemistry C* 115.49 (Dec. 15, 2011), pp. 24172–24177. ISSN: 1932-7447, 1932-7455. DOI: 10.1021/jp206675u. URL: <http://pubs.acs.org/doi/10.1021/jp206675u> (visited on 08/16/2018).
- [19] Carsten Busse et al. “Graphene on Ir(111): Physisorption with Chemical Modulation”. In: *Phys. Rev. Lett.* 107.3 (July 2011), p. 036101. DOI: 10.1103/PhysRevLett.107.036101. URL: <http://link.aps.org/doi/10.1103/PhysRevLett.107.036101>.
- [20] CAS DataBase | 7664-38-2. Dec. 11, 2014. URL: http://www.chemicalbook.com/CASEN_7664-38-2.htm (visited on 12/11/2014).
- [21] E. Ćavar et al. “A single h-BN layer on Pt(111)”. In: *Surface Science* 602.9 (May 2008), pp. 1722–1726. ISSN: 00396028. DOI: 10.1016/j.susc.2008.03.008. URL: <http://linkinghub.elsevier.com/retrieve/pii/S0039602808001672> (visited on 08/14/2018).
- [22] Shih-Chieh Chang et al. “Superpolishing for Planarizing Copper Damascene Interconnects”. In: *Electrochemical and Solid-State Letters* 6.5 (Jan. 5, 2003), G72–G74. ISSN: 1099-0062, 1944-8775. DOI: 10.1149/1.1565853. URL: <http://esl.ecsdl.org/content/6/5/G72> (visited on 12/11/2014).
- [23] Shahana Chatterjee et al. “Chemical Vapor Deposition of Boron Nitride Nanosheets on Metallic Substrates via Decaborane/Ammonia Reactions”. In: *Chemistry of Materials* 23.20 (Oct. 25, 2011), pp. 4414–4416. ISSN: 0897-4756. DOI: 10.1021/cm201955v. URL: <http://dx.doi.org/10.1021/cm201955v> (visited on 11/10/2014).
- [24] C. Julian Chen. *Introduction to scanning tunneling microscopy*. 2nd ed. Monographs on the physics and chemistry of materials 64. Oxford ; New York: Oxford University Press, 2008. 423 pp. ISBN: 978-0-19-921150-0.

- [25] F. Cicullo et al. “A Quasi-Free-Standing Single Layer of a B3N3-Doped Nanographene Molecule Deposited on Au(111) Single Crystals”. In: *The Journal of Physical Chemistry C* 120.31 (2016), pp. 17645–17651. DOI: 10.1021/acs.jpcc.6b06237. eprint: <https://doi.org/10.1021/acs.jpcc.6b06237>. URL: <https://doi.org/10.1021/acs.jpcc.6b06237>.
- [26] S. Ciraci, A. Baratoff, and Inder P. Batra. “Tip-sample interaction effects in scanning-tunneling and atomic-force microscopy”. In: *Physical Review B* 41.5 (1990), p. 2763. URL: <http://journals.aps.org/prb/abstract/10.1103/PhysRevB.41.2763> (visited on 07/17/2015).
- [27] Johann Coraux et al. “Growth of graphene on Ir(111)”. In: *New Journal of Physics* 11.2 (2009), p. 023006. URL: <http://stacks.iop.org/1367-2630/11/i=2/a=023006>.
- [28] Martina Corso, Thomas Greber, and Jürg Osterwalder. “h-BN on Pd(110): a tunable system for self-assembled nanostructures?” In: *Surface Science* 577.2 (Mar. 2005), pp. L78–L84. ISSN: 00396028. DOI: 10.1016/j.susc.2005.01.015. URL: <http://linkinghub.elsevier.com/retrieve/pii/S0039602805000531> (visited on 08/14/2018).
- [29] Martina Corso et al. “Boron Nitride Nanomesh”. In: *Science* 303.5655 (2004), pp. 217–220. DOI: 10.1126/science.1091979. URL: <http://www.sciencemag.org/content/303/5655/217.abstract>.
- [30] Andrew G. Crawford et al. “Experimental and Theoretical Studies of the Photophysical Properties of 2- and 2,7-Functionalized Pyrene Derivatives”. In: *Journal of the American Chemical Society* 133.34 (Aug. 31, 2011), pp. 13349–13362. ISSN: 0002-7863. DOI: 10.1021/ja2006862. URL: <http://dx.doi.org/10.1021/ja2006862> (visited on 08/22/2017).
- [31] Steven De Feyter and Frans C. De Schryver. “Two-dimensional supramolecular self-assembly probed by scanning tunneling microscopy”. In: *Chemical Society Reviews* 32.3 (Apr. 24, 2003), pp. 139–150. ISSN: 03060012, 14604744. DOI: 10.1039/b206566p. URL: <http://xlink.rsc.org/?DOI=b206566p> (visited on 08/21/2018).
- [32] Ada Della Pia et al. “Anomalous Coarsening Driven by Reversible Charge Transfer at Metal–Organic Interfaces”. In: *ACS Nano* 8.12 (Dec. 23, 2014), pp. 12356–12364. ISSN: 1936-0851. DOI: 10.1021/nn505063w. URL: <http://dx.doi.org/10.1021/nn505063w> (visited on 02/21/2017).
- [33] G. Deroubaix and P. Marcus. “X-ray photoelectron spectroscopy analysis of copper and zinc oxides and sulphides”. In: *Surface and Interface Analysis* 18.1 (1992), pp. 39–46. ISSN: 1096-9918. DOI: 10.1002/sia.740180107. URL: <http://onlinelibrary.wiley.com/doi/10.1002/sia.740180107/abstract> (visited on 12/15/2014).
- [34] K. Diller et al. “Self-metallation of 2H-tetraphenylporphyrin on Cu(111): an x-ray spectroscopy study”. In: *The Journal of Chemical Physics* 136.1 (Jan. 7, 2012), p. 014705. ISSN: 1089-7690. DOI: 10.1063/1.3674165.
- [35] Katharina Diller et al. “In vacuo interfacial tetrapyrrole metallation”. In: *Chemical Society Reviews* 45.6 (2016), pp. 1629–1656. ISSN: 0306-0012, 1460-4744. DOI: 10.1039/C5CS00207A. URL: <http://xlink.rsc.org/?DOI=C5CS00207A> (visited on 08/21/2018).

- [36] P. A. M. Dirac. “On the Theory of Quantum Mechanics”. In: *Proceedings of the Royal Society A: Mathematical, Physical and Engineering Sciences* 112.762 (Oct. 1, 1926), pp. 661–677. ISSN: 1364-5021, 1471-2946. DOI: 10.1098/rspa.1926.0133. URL: <http://rspa.royalsocietypublishing.org/cgi/doi/10.1098/rspa.1926.0133> (visited on 08/23/2018).
- [37] *Dislocation theory*. Oct. 27, 2015. URL: http://eng.sut.ac.th/metal/images/stories/pdf/05_Dislocation_theory.pdf (visited on 10/27/2015).
- [38] Stefanie Ditze et al. “Activation Energy for the Self-Metalation Reaction of 2H-Tetr phenylporphyrin on Cu(111)”. In: *Angewandte Chemie International Edition* 51.43 (Oct. 22, 2012), pp. 10898–10901. ISSN: 1521-3773. DOI: 10.1002/anie.201205464. URL: <http://onlinelibrary.wiley.com/doi/10.1002/anie.201205464/abstract> (visited on 11/05/2014).
- [39] Stefanie Ditze et al. “On the Energetics of Conformational Switching of Molecules at and Close to Room Temperature”. In: *Journal of the American Chemical Society* 136.4 (Jan. 29, 2014), pp. 1609–1616. ISSN: 0002-7863. DOI: 10.1021/ja411884p. URL: <http://dx.doi.org/10.1021/ja411884p> (visited on 11/12/2015).
- [40] Jacopo Dosso et al. “Synthesis and Optoelectronic Properties of Hexa-*peri*-hexabenzoborazinocoronene”. In: *Angewandte Chemie* 129.16 (Apr. 10, 2017), pp. 4554–4558. ISSN: 00448249. DOI: 10.1002/ange.201700907. URL: <http://doi.wiley.com/10.1002/ange.201700907> (visited on 08/16/2018).
- [41] D. Ecija et al. “Dynamics and thermal stability of surface-confined metal-organic chains”. In: *Surface Science* 643 (Jan. 2016), pp. 91–97. ISSN: 00396028. DOI: 10.1016/j.susc.2015.08.013. URL: <http://linkinghub.elsevier.com/retrieve/pii/S0039602815002332> (visited on 08/21/2018).
- [42] D. M. Eigler et al. “Imaging Xe with a low-temperature scanning tunneling microscope”. In: *Physical Review Letters* 66.9 (Mar. 4, 1991), pp. 1189–1192. ISSN: 0031-9007. DOI: 10.1103/PhysRevLett.66.1189. URL: <https://link.aps.org/doi/10.1103/PhysRevLett.66.1189> (visited on 08/23/2018).
- [43] Gerhard Ertl and J. Kuppers. *Low Energy Electrons and Surface Chemistry*. Auflage: 2 Sub. Weinheim, Federal Republic of Germany ; Deerfield Beach, FL, USA: Vch Pub, Mar. 1986. ISBN: 9780895730657.
- [44] R.M. Feenstra, Joseph A. Stroscio, and A.P. Fein. “Tunneling spectroscopy of the Si(111)2 Å“ 1 surface”. In: *Surface Science* 181.1 (Mar. 1987), pp. 295–306. ISSN: 00396028. DOI: 10.1016/0039-6028(87)90170-1. URL: <http://linkinghub.elsevier.com/retrieve/pii/0039602887901701> (visited on 07/17/2015).
- [45] Xing Feng et al. “Functionalization of Pyrene To Prepare Luminescent Materials-Typical Examples of Synthetic Methodology”. In: *Chemistry - A European Journal* 22.34 (Aug. 16, 2016), pp. 11898–11916. ISSN: 09476539. DOI: 10.1002/chem.201600465. URL: <http://doi.wiley.com/10.1002/chem.201600465> (visited on 01/04/2018).
- [46] E. Fermi. “Zur Quantelung des idealen einatomigen Gases”. In: *Zeitschrift für Physik* 36.11 (Nov. 1926), pp. 902–912. ISSN: 1434-6001, 1434-601X. DOI: 10.1007/BF01400221. URL: <http://link.springer.com/10.1007/BF01400221> (visited on 08/23/2018).

- [47] Manuela Garnica. "Electron acceptor molecules deposited on epitaxial graphene studied by means of low temperature scanning tunneling microscopy / spectroscopy". PhD thesis. Madrid: Universidad Autonoma de Madrid, July 1, 2013. 138 pp.
- [48] Jaime Gómez Díaz et al. "Hexagonal boron nitride on transition metal surfaces". In: *Theoretical Chemistry Accounts* 132.4 (Apr. 2013). ISSN: 1432-881X, 1432-2234. DOI: 10.1007/s00214-013-1350-z. URL: <http://link.springer.com/10.1007/s00214-013-1350-z> (visited on 10/23/2014).
- [49] Rubén González-Moreno et al. "Following the Metalation Process of Protoporphyrin IX with Metal Substrate Atoms at Room Temperature". In: *The Journal of Physical Chemistry C* 115.14 (Apr. 14, 2011), pp. 6849–6854. ISSN: 1932-7447, 1932-7455. DOI: 10.1021/jp200533a. URL: <http://pubs.acs.org/doi/10.1021/jp200533a> (visited on 08/16/2018).
- [50] Andrii Goriachko et al. "Self-Assembly of a Hexagonal Boron Nitride Nanomesh on Ru(0001)". In: *Langmuir* 23.6 (2007). STM, pp. 2928–2931. DOI: 10.1021/la062990t. URL: <http://pubs.acs.org/doi/abs/10.1021/la062990t>.
- [51] Elin Gränäs et al. "Oxygen Intercalation under Graphene on Ir(111): Energetics, Kinetics, and the Role of Graphene Edges". In: *ACS Nano* 6.11 (Nov. 27, 2012), pp. 9951–9963. ISSN: 1936-0851, 1936-086X. DOI: 10.1021/nn303548z. URL: <http://pubs.acs.org/doi/abs/10.1021/nn303548z> (visited on 10/15/2014).
- [52] *Graphene Supermarket :: Boron Nitride (BN) :: Single layer h-BN (Boron Nitride) film grown on copper foil: 2" x 1"*. Dec. 11, 2014. URL: <https://graphene-supermarket.com/Single-layer-h-BN-Boron-Nitride-film-grown-in-copper-foil-2-x-1.html> (visited on 12/11/2014).
- [53] L. Gross et al. "The Chemical Structure of a Molecule Resolved by Atomic Force Microscopy". In: *Science* 325.5944 (Aug. 28, 2009), pp. 1110–1114. ISSN: 0036-8075, 1095-9203. DOI: 10.1126/science.1176210. URL: <http://www.sciencemag.org/cgi/doi/10.1126/science.1176210> (visited on 05/25/2018).
- [54] K. H. Gundlach. "Zur berechnung des tunnelstroms durch eine trapezförmige potentialstufe". In: *Solid-State Electronics* 9.10 (Oct. 1966), pp. 949–957. ISSN: 0038-1101. DOI: 10.1016/0038-1101(66)90071-2. URL: <http://www.sciencedirect.com/science/article/pii/0038110166900712> (visited on 07/22/2015).
- [55] Ning Guo et al. "Controllable growth of triangular hexagonal boron nitride domains on copper foils by an improved low-pressure chemical vapor deposition method". In: *Nanotechnology* 23.41 (Oct. 19, 2012), p. 415605. ISSN: 0957-4484, 1361-6528. DOI: 10.1088/0957-4484/23/41/415605. URL: <http://stacks.iop.org/0957-4484/23/i=41/a=415605?key=crossref.113b515178c834c75ca332235bf20bf1> (visited on 10/15/2014).
- [56] Tongwei Han, Ying Luo, and Chengyuan Wang. "Effects of temperature and strain rate on the mechanical properties of hexagonal boron nitride nanosheets". In: *Journal of Physics D: Applied Physics* 47.2 (2014), p. 025303. URL: <http://stacks.iop.org/0022-3727/47/i=2/a=025303>.
- [57] Paul K. Hansma, ed. *Tunneling spectroscopy: capabilities, applications, and new techniques*. New York: Plenum Press, 1982. 493 pp. ISBN: 978-0-306-41070-3.

- [58] Sam Haq et al. “Clean Coupling of Unfunctionalized Porphyrins at Surfaces To Give Highly Oriented Organometallic Oligomers”. In: *Journal of the American Chemical Society* 133.31 (Aug. 10, 2011), pp. 12031–12039. ISSN: 0002-7863, 1520-5126. DOI: 10.1021/ja201389u. URL: <http://pubs.acs.org/doi/abs/10.1021/ja201389u> (visited on 08/16/2018).
- [59] Yuanqin He. “Bottom-up Construction and Direct Characterization of Porphyrin- and Graphene-based Nanostructures”. PhD thesis. München: Technische Universität München, June 19, 2017. 147 pp. URL: <http://nbn-resolving.de/urn/resolver.pl?urn=nbn:de:bvb:91-diss-20170720-1362063-1-5>.
- [60] Daniel Heim et al. “Self-Assembly of Flexible One-Dimensional Coordination Polymers on Metal Surfaces”. In: *Journal of the American Chemical Society* 132.19 (May 19, 2010), pp. 6783–6790. ISSN: 0002-7863. DOI: 10.1021/ja1010527. URL: <http://dx.doi.org/10.1021/ja1010527> (visited on 04/14/2016).
- [61] Daniel Heim et al. “Surface-Assisted Assembly of Discrete Porphyrin-Based Cyclic Supramolecules”. In: *Nano Letters* 10.1 (Jan. 13, 2010), pp. 122–128. ISSN: 1530-6984. DOI: 10.1021/nl9029994. URL: <http://dx.doi.org/10.1021/nl9029994> (visited on 04/14/2016).
- [62] B. L. Henke, E. M. Gullikson, and J. C. Davis. “X-Ray Interactions: Photoabsorption, Scattering, Transmission, and Reflection at $E = 50\text{--}30,000 \text{ eV}$, $Z = 1\text{--}92$ ”. In: *Atomic Data and Nuclear Data Tables* 54.2 (July 1993), pp. 181–342. ISSN: 0092-640X. DOI: 10.1006/adnd.1993.1013. URL: <http://www.sciencedirect.com/science/article/pii/S0092640X83710132> (visited on 12/05/2014).
- [63] Klaus Hermann. “Periodic overlayers and moire patterns: theoretical studies of geometric properties”. In: *Journal of Physics: Condensed Matter* 24.31 (2012), p. 314210. ISSN: 0953-8984. DOI: 10.1088/0953-8984/24/31/314210. URL: <http://stacks.iop.org/0953-8984/24/i=31/a=314210> (visited on 10/27/2015).
- [64] H. Hertz. “Ueber einen Einfluss des ultravioletten Lichtes auf die electrische Entladung”. In: *Annalen der Physik* 267.8 (1887), pp. 983–1000. ISSN: 1521-3889. DOI: 10.1002/andp.18872670827. URL: <http://onlinelibrary.wiley.com/doi/10.1002/andp.18872670827/abstract> (visited on 01/12/2015).
- [65] “HyperChem(TM) Professional 7.51, Hypercube, Inc., 1115 NW 4th Street, Gainesville, Florida 32601, USA.”
- [66] Cristian Iacovita et al. “Controlling the Dimensionality and Structure of Supramolecular Porphyrin Assemblies by their Functional Substituents: Dimers, Chains, and Close-Packed 2D Assemblies”. In: *Chemistry - A European Journal* 18.46 (Nov. 12, 2012), pp. 14610–14613. ISSN: 09476539. DOI: 10.1002/chem.201201037. URL: <http://doi.wiley.com/10.1002/chem.201201037> (visited on 07/13/2015).
- [67] Ariel Ismach et al. “Toward the Controlled Synthesis of Hexagonal Boron Nitride Films”. In: *ACS Nano* 6.7 (July 24, 2012), pp. 6378–6385. ISSN: 1936-0851. DOI: 10.1021/nn301940k. URL: <http://dx.doi.org/10.1021/nn301940k> (visited on 11/10/2014).
- [68] J. F. Jia et al. “Variation of the local work function at steps on metal surfaces studied with STM”. In: *Physical Review B* 58.3 (July 15, 1998), pp. 1193–1196. DOI: 10.1103/PhysRevB.58.1193. URL: <http://link.aps.org/doi/10.1103/PhysRevB.58.1193> (visited on 07/22/2015).

- [69] Zhang Jian-Min, Ma Fei, and Xu Ke-Wei. "Calculation of the surface energy of fcc metals with modified embedded-atom method". In: *Chinese Physics* 13.7 (2004), p. 1082. ISSN: 1009-1963. DOI: 10.1088/1009-1963/13/7/020. URL: <http://stacks.iop.org/1009-1963/13/i=7/a=020> (visited on 11/12/2015).
- [70] Huo Jinshan. "Electrochemical planarization of copper for microelectronic applications". In: (2004). URL: <http://digitalcommons.ohsu.edu/cgi/viewcontent.cgi?article=1208&context=etd> (visited on 12/12/2014).
- [71] J. E. Jones. "On the Determination of Molecular Fields. II. From the Equation of State of a Gas". In: *Proceedings of the Royal Society A: Mathematical, Physical and Engineering Sciences* 106.738 (Oct. 1, 1924), pp. 463–477. ISSN: 1364-5021, 1471-2946. DOI: 10.1098/rspa.1924.0082. URL: <http://rspa.royalsocietypublishing.org/cgi/doi/10.1098/rspa.1924.0082> (visited on 08/23/2018).
- [72] William L. Jorgensen and Lionel Salem. "*The Organic Chemist's Book of Orbitals*". New York: Academic Press, 1973. ISBN: 0-12-390250-9.
- [73] Sushobhan Joshi et al. "Boron Nitride on Cu(111): An Electronically Corrugated Monolayer". In: *Nano Letters* 12.11 (2012), pp. 5821–5828. DOI: 10.1021/nl303170m. URL: <http://pubs.acs.org/doi/abs/10.1021/nl303170m>.
- [74] Kazuaki Kato and Hans-Jörg Schneider. "Dispersive Effects in Chemomechanical Reactions with Polyallylamine-Derived Hydrogels". In: *European Journal of Organic Chemistry* 2008.8 (Mar. 1, 2008), pp. 1378–1382. ISSN: 1099-0690. DOI: 10.1002/ejoc.200700850. URL: <http://onlinelibrary.wiley.com/doi/10.1002/ejoc.200700850/abstract> (visited on 04/14/2016).
- [75] Shigeki Kawai et al. "Atomically controlled substitutional boron-doping of graphene nanoribbons". In: *Nature Communications* 6.1 (Dec. 2015). ISSN: 2041-1723. DOI: 10.1038/ncomms9098. URL: <http://www.nature.com/articles/ncomms9098> (visited on 05/28/2018).
- [76] Shigeki Kawai et al. "Multiple heteroatom substitution to graphene nanoribbon". In: *Science Advances* 4.4 (Apr. 2018), eaar7181. ISSN: 2375-2548. DOI: 10.1126/sciadv.aar7181. URL: <http://advances.sciencemag.org/lookup/doi/10.1126/sciadv.aar7181> (visited on 05/28/2018).
- [77] Z. H. Khan and B. N. Khanna. "Electronic absorption spectra of pyrene and its monopositive ion". In: *The Journal of Chemical Physics* 59.6 (Sept. 15, 1973), pp. 3015–3019. ISSN: 0021-9606, 1089-7690. DOI: 10.1063/1.1680437. URL: <http://scitation.aip.org/content/aip/journal/jcp/59/6/10.1063/1.1680437> (visited on 07/29/2016).
- [78] Piran R. Kidambi et al. "In Situ Observations during Chemical Vapor Deposition of Hexagonal Boron Nitride on Polycrystalline Copper". In: *Chemistry of Materials* 26.22 (2014), pp. 6380–6392. ISSN: 0897-4756. DOI: 10.1021/cm502603n. URL: <http://dx.doi.org/10.1021/cm502603n> (visited on 12/15/2014).
- [79] Ki Kang Kim et al. "Synthesis and Characterization of Hexagonal Boron Nitride Film as a Dielectric Layer for Graphene Devices". In: *ACS Nano* 6.10 (Oct. 23, 2012), pp. 8583–8590. ISSN: 1936-0851, 1936-086X. DOI: 10.1021/nn301675f. URL: <http://pubs.acs.org/doi/abs/10.1021/nn301675f> (visited on 12/01/2014).

- [80] Ki Kang Kim et al. “Synthesis of Monolayer Hexagonal Boron Nitride on Cu Foil Using Chemical Vapor Deposition”. In: *Nano Letters* 12.1 (Jan. 11, 2012), pp. 161–166. ISSN: 1530-6984. DOI: 10.1021/nl203249a. URL: <http://dx.doi.org/10.1021/nl203249a> (visited on 11/10/2014).
- [81] Katsuyoshi Kobayashi. “Simulation of scanning tunneling microscope image based on electronic states of surface/tip system”. In: *Journal of Vacuum Science & Technology A: Vacuum, Surfaces, and Films* 8.1 (Jan. 1990), p. 170. ISSN: 07342101. DOI: 10.1116/1.577057. URL: <http://scitation.aip.org/content/avs/journal/jvsta/8/1/10.1116/1.577057> (visited on 07/17/2015).
- [82] H. A. Kramers. “Wellenmechanik und halbzahlige Quantisierung”. In: *Zeitschrift für Physik* 39.10 (Oct. 1926), pp. 828–840. ISSN: 1434-6001, 1434-601X. DOI: 10.1007/BF01451751. URL: <http://link.springer.com/10.1007/BF01451751> (visited on 08/23/2018).
- [83] Matthias Krieg et al. “Construction of an Internally B3N3-Doped Nanographene Molecule”. In: *Angewandte Chemie International Edition* 54.28 (), pp. 8284–8286. DOI: 10.1002/anie.201412165. eprint: <https://onlinelibrary.wiley.com/doi/pdf/10.1002/anie.201412165>. URL: <https://onlinelibrary.wiley.com/doi/abs/10.1002/anie.201412165>.
- [84] Ryohei Kurata et al. “Diarylarnino- and Diarylboryl-Substituted Donor–Acceptor Pyrene Derivatives: Influence of Substitution Pattern on Their Photophysical Properties”. In: *The Journal of Organic Chemistry* 82.10 (May 19, 2017), pp. 5111–5121. ISSN: 0022-3263. DOI: 10.1021/acs.joc.7b00315. URL: <http://dx.doi.org/10.1021/acs.joc.7b00315> (visited on 08/22/2017).
- [85] N. D. Lang. “Theory of Single-Atom Imaging in the Scanning Tunneling Microscope”. In: *Physical Review Letters* 56.11 (Mar. 17, 1986), pp. 1164–1167. ISSN: 0031-9007. DOI: 10.1103/PhysRevLett.56.1164. URL: <https://link.aps.org/doi/10.1103/PhysRevLett.56.1164> (visited on 08/23/2018).
- [86] D. Lawunmi and M. C. Payne. “Theoretical investigation of the scanning tunnelling microscope image of graphite”. In: *Journal of Physics: Condensed Matter* 2.16 (1990), p. 3811. URL: <http://iopscience.iop.org/0953-8984/2/16/011> (visited on 07/17/2015).
- [87] Kang Hyuck Lee et al. “Large-Scale Synthesis of High-Quality Hexagonal Boron Nitride Nanosheets for Large-Area Graphene Electronics”. In: *Nano Letters* 12.2 (Feb. 8, 2012), pp. 714–718. ISSN: 1530-6984. DOI: 10.1021/nl203635v. URL: <http://dx.doi.org/10.1021/nl203635v> (visited on 11/10/2014).
- [88] Yeon Ok Lee et al. “Enhanced Electrogenerated Chemiluminescence of Phenylethynylpyrene Derivatives: Use of Weakly Electron-Donating Group as a Substituent”. In: *The Journal of Organic Chemistry* 77.24 (Dec. 21, 2012), pp. 11007–11013. ISSN: 0022-3263. DOI: 10.1021/jo3010974. URL: <http://dx.doi.org/10.1021/jo3010974> (visited on 08/22/2017).
- [89] Qiucheng Li et al. “Grain Boundary Structures and Electronic Properties of Hexagonal Boron Nitride on Cu(111)”. In: *Nano Letters* 15.9 (Sept. 9, 2015), pp. 5804–5810. ISSN: 1530-6984. DOI: 10.1021/acs.nanolett.5b01852. URL: <http://dx.doi.org/10.1021/acs.nanolett.5b01852> (visited on 05/03/2017).

- [90] L. Lilje et al. “Improved surface treatment of the superconducting TESLA cavities”. In: *Nuclear Instruments and Methods in Physics Research Section A: Accelerators, Spectrometers, Detectors and Associated Equipment* 516.2 (2004), pp. 213–227. ISSN: 0168-9002. DOI: <https://doi.org/10.1016/j.nima.2003.08.116>. URL: <http://www.sciencedirect.com/science/article/pii/S0168900203024318>.
- [91] C. L. Lin et al. “Manifestation of Work Function Difference in High Order Gundlach Oscillation”. In: *Physical Review Letters* 99.21 (Nov. 20, 2007), p. 216103. DOI: 10.1103/PhysRevLett.99.216103. URL: <http://link.aps.org/doi/10.1103/PhysRevLett.99.216103> (visited on 07/22/2015).
- [92] Qianqian Liu et al. “Oxygen chemisorption-induced surface phase transitions on Cu(110)”. In: *Surface Science* 627 (Sept. 2014), pp. 75–84. ISSN: 0039-6028. DOI: 10.1016/j.susc.2014.04.017. URL: <http://www.sciencedirect.com/science/article/pii/S0039602814001174> (visited on 11/12/2015).
- [93] Ch. Loppacher et al. “Direct Determination of the Energy Required to Operate a Single Molecule Switch”. In: *Physical Review Letters* 90.6 (Feb. 14, 2003). ISSN: 0031-9007, 1079-7114. DOI: 10.1103/PhysRevLett.90.066107. URL: <https://link.aps.org/doi/10.1103/PhysRevLett.90.066107> (visited on 08/15/2018).
- [94] Samir Lounis. “Theory of Scanning Tunneling Microscopy”. In: *arXiv:1404.0961 [cond-mat]* (Apr. 3, 2014). arXiv: 1404.0961. URL: <http://arxiv.org/abs/1404.0961> (visited on 08/09/2018).
- [95] Zhengtang Luo et al. “Effect of Substrate Roughness and Feedstock Concentration on Growth of Wafer-Scale Graphene at Atmospheric Pressure”. In: *Chemistry of Materials* 23.6 (Mar. 22, 2011), pp. 1441–1447. ISSN: 0897-4756, 1520-5002. DOI: 10.1021/cm1028854. URL: <http://pubs.acs.org/doi/abs/10.1021/cm1028854> (visited on 12/09/2014).
- [96] William P. Lustig et al. “Metal–organic frameworks: functional luminescent and photonic materials for sensing applications”. In: *Chem. Soc. Rev.* 46 (11 2017), pp. 3242–3285. DOI: 10.1039/C6CS00930A. URL: <http://dx.doi.org/10.1039/C6CS00930A>.
- [97] Chuanxu Ma et al. “Interplay between intercalated oxygen superstructures and monolayer h -BN on Cu(100)”. In: *Physical Review B* 94.6 (Aug. 18, 2016). ISSN: 2469-9950, 2469-9969. DOI: 10.1103/PhysRevB.94.064106. URL: <https://link.aps.org/doi/10.1103/PhysRevB.94.064106> (visited on 08/10/2018).
- [98] Hajime Maeda et al. “Alkynylpyrenes as Improved Pyrene-Based Biomolecular Probes with the Advantages of High Fluorescence Quantum Yields and Long Absorption/Emission Wavelengths”. In: *Chemistry - A European Journal* 12.3 (Jan. 11, 2006), pp. 824–831. ISSN: 1521-3765. DOI: 10.1002/chem.200500638. URL: <http://onlinelibrary.wiley.com/doi/10.1002/chem.200500638/abstract> (visited on 07/12/2017).
- [99] *MaTecK*. Aug. 10, 2018. URL: <https://mateck.com/info/metal-single-crystals.html> (visited on 08/10/2018).
- [100] Manfred Matena et al. “Aggregation and Contingent Metal/Surface Reactivity of 1,3,8,10-Tetraazaperopyrrene (TAPP) on Cu(111)”. In: *Chemistry – A European Journal* 16.7 (Feb. 15, 2010), pp. 2079–2091. ISSN: 1521-3765. DOI: 10.1002/chem.200902596. URL: <http://onlinelibrary.wiley.com/doi/10.1002/chem.200902596/abstract> (visited on 02/22/2017).

- [101] Puneet Mishra et al. “Current-Driven Supramolecular Motor with In Situ Surface Chiral Directionality Switching”. In: *Nano Letters* 15.7 (July 8, 2015), pp. 4793–4798. ISSN: 1530-6984, 1530-6992. DOI: 10.1021/acs.nanolett.5b01908. URL: <http://pubs.acs.org/doi/abs/10.1021/acs.nanolett.5b01908> (visited on 07/13/2015).
- [102] Francesca Moresco et al. “Conformational Changes of Single Molecules Induced by Scanning Tunneling Microscopy Manipulation: A Route to Molecular Switching”. In: *Physical Review Letters* 86.4 (Jan. 22, 2001), pp. 672–675. DOI: 10.1103/PhysRevLett.86.672. URL: <http://link.aps.org/doi/10.1103/PhysRevLett.86.672> (visited on 11/12/2015).
- [103] M. Morscher et al. “Formation of single layer h-BN on Pd(111)”. In: *Surface Science* 600.16 (2006), pp. 3280–3284. ISSN: 0039-6028. DOI: <http://dx.doi.org/10.1016/j.susc.2006.06.016>. URL: <http://www.sciencedirect.com/science/article/pii/S0039602806007266>.
- [104] Bohayra Mortazavi and Yves Rémond. “Investigation of tensile response and thermal conductivity of boron-nitride nanosheets using molecular dynamics simulations”. In: *Physica E: Low-dimensional Systems and Nanostructures* 44.9 (2012), pp. 1846–1852. ISSN: 1386-9477. DOI: <http://dx.doi.org/10.1016/j.physe.2012.05.007>. URL: <http://www.sciencedirect.com/science/article/pii/S1386947712001804>.
- [105] Frank Müller, Klaus Stöwe, and Hermann Sachdev. “Symmetry versus Comensurability: Epitaxial Growth of Hexagonal Boron Nitride on Pt(111) From B-Trichloroborazine (ClBNH)₃”. In: *Chemistry of Materials* 17.13 (2005), pp. 3464–3467. DOI: 10.1021/cm048629e. URL: <http://pubs.acs.org/doi/abs/10.1021/cm048629e>.
- [106] Frank Müller et al. “Epitaxial growth of hexagonal boron nitride on Ag(111)”. In: *Phys. Rev. B* 82.11 (Sept. 2010), p. 113406. DOI: 10.1103/PhysRevB.82.113406. URL: <http://link.aps.org/doi/10.1103/PhysRevB.82.113406>.
- [107] Alpha T N'Diaye et al. “Structure of epitaxial graphene on Ir(111)”. In: *New Journal of Physics* 10.4 (Apr. 18, 2008), p. 043033. ISSN: 1367-2630. DOI: 10.1088/1367-2630/10/4/043033. URL: <http://stacks.iop.org/1367-2630/10/i=4/a=043033?key=crossref.0e41254297199ed913e0eb6bd000151a> (visited on 10/15/2014).
- [108] A. Nagashima et al. “Electronic Structure of Monolayer Hexagonal Boron Nitride Physisorbed on Metal Surfaces”. In: *Phys. Rev. Lett.* 75.21 (Nov. 1995), pp. 3918–3921. DOI: 10.1103/PhysRevLett.75.3918. URL: <http://link.aps.org/doi/10.1103/PhysRevLett.75.3918>.
- [109] Melvin S. Newman and Daniel Lednicer. “The Synthesis and Resolution of Hexahelicene”. In: *Journal of the American Chemical Society* 78.18 (Sept. 1, 1956), pp. 4765–4770. ISSN: 0002-7863. DOI: 10.1021/ja01599a060. URL: <http://dx.doi.org/10.1021/ja01599a060> (visited on 06/01/2016).
- [110] Fabrizio Orlando et al. “Epitaxial Growth of Hexagonal Boron Nitride on Ir(111)”. In: *The Journal of Physical Chemistry C* 116.1 (2012), pp. 157–164. DOI: 10.1021/jp207571n. URL: <http://pubs.acs.org/doi/abs/10.1021/jp207571n>.

- [111] V. Palmieri et al. “Besides the standard Niobium bath chemical polishing”. In: 10 th W orkshop on RF Su percondutivity. Tsukuba , Japan, 2001. URL: <https://accelconf.web.cern.ch/accelconf/srf01/papers/pr016.pdf> (visited on 08/11/2018).
- [112] W. Paszkowicz et al. “Lattice parameters and anisotropic thermal expansion of hexagonal boron nitride in the \$10-297.5\text{ }\text{\textdegree}\text{K}\$ temperature range”. In: *Applied Physics A* 75.3 (2002), pp. 431–435. ISSN: 0947-8396. DOI: 10.1007/s003390100999. URL: <http://dx.doi.org/10.1007/s003390100999>.
- [113] Niko Pavliček and Leo Gross. “Generation, manipulation and characterization of molecules by atomic force microscopy”. In: *Nature Reviews Chemistry* 1 (Jan. 11, 2017), p. 0005. URL: <http://dx.doi.org/10.1038/s41570-016-0005>.
- [114] Qing Peng, Wei Ji, and Suvranu De. “Mechanical properties of the hexagonal boron nitride monolayer: Ab initio study”. In: *Computational Materials Science* 56.0 (2012), pp. 11–17. ISSN: 0927-0256. DOI: <http://dx.doi.org/10.1016/j.commatsci.2011.12.029>. URL: <http://www.sciencedirect.com/science/article/pii/S0927025611006902>.
- [115] Tuan Anh Pham et al. “Comparing Ullmann Coupling on Noble Metal Surfaces: On-Surface Polymerization of 1,3,6,8-Tetrabromopyrene on Cu(111) and Au(111)”. In: *Chemistry – A European Journal* 22.17 (Apr. 18, 2016), pp. 5937–5944. ISSN: 1521-3765. DOI: 10.1002/chem.201504946. URL: <http://onlinelibrary.wiley.com/doi/10.1002/chem.201504946/abstract> (visited on 02/21/2017).
- [116] Tuan Anh Pham et al. “Heat-induced formation of one-dimensional coordination polymers on Au(111): an STM study”. In: *Chemical Communications* 51.77 (2015), pp. 14473–14476. ISSN: 1359-7345, 1364-548X. DOI: 10.1039/C5CC04940G. URL: <http://xlink.rsc.org/?DOI=C5CC04940G> (visited on 08/21/2018).
- [117] Tuan Anh Pham et al. “Self-assembly of pyrene derivatives on Au(111): substituent effects on intermolecular interactions”. In: 50.91 (Oct. 21, 2014), pp. 14089–14092. ISSN: 1364-548X. DOI: 10.1039/C4CC02753A. URL: <http://pubs.rsc.org/en/content/articlelanding/2014/cc/c4cc02753a> (visited on 02/21/2017).
- [118] A. B. Preobrajenski et al. “Monolayer h-BN on lattice-mismatched metal surfaces: On the formation of the nanomesh”. In: *Chemical Physics Letters* 446.1 (2007), pp. 119–123. ISSN: 0009-2614. DOI: 10.1016/j.cplett.2007.08.028. URL: <http://www.sciencedirect.com/science/article/pii/S0009261407010998>.
- [119] A.B. Preobrajenski, A.S. Vinogradov, and N. Mårtensson. “Monolayer of h-BN chemisorbed on Cu(111) and Ni(111): The role of the transition metal 3d states”. In: *Surface Science* 582.1 (May 2005), pp. 21–30. ISSN: 00396028. DOI: 10.1016/j.susc.2005.02.047. URL: <http://linkinghub.elsevier.com/retrieve/pii/S0039602805002426> (visited on 10/28/2014).
- [120] Paweł Przychodzeń et al. “Supramolecular coordination networks based on octacyanometalates: From structure to function”. In: *Coordination Chemistry Reviews*. 20th International Conference on Coordination and Bioinorganic Chemistry 250.17 (Sept. 2006), pp. 2234–2260. ISSN: 0010-8545. DOI: 10.1016/j.ccr.2006.01.026. URL: <http://www.sciencedirect.com/science/article/pii/S0010854506000348> (visited on 08/26/2016).

- [121] Andreas Riemann. “Ionic Insulators on Vicinal Metal Surfaces”. PhD thesis. Freie Universität Berlin, Freie Universität Berlin, Germany, 2002. URL: http://edocs.fu-berlin.de/diss/receive/FUDISS_thesis_00000000587 (visited on 07/27/2015).
- [122] J.C. Rivière. “Instrumentation”. In: *Auger and X-ray Photoelectron Spectroscopy*. Ed. by D. Briggs and M.P. Seah. Frankfurt am Main: Otto Salle Verlag GmbH & Co., 1990.
- [123] Geoffrey Rojas et al. “Self-Assembly and Properties of Nonmetalated Tetraphenyl-Porphyrin on Metal Substrates”. In: *The Journal of Physical Chemistry C* 114.20 (May 27, 2010), pp. 9408–9415. ISSN: 1932-7447, 1932-7455. DOI: 10.1021/jp1012957. URL: <http://pubs.acs.org/doi/10.1021/jp1012957> (visited on 08/16/2018).
- [124] Geoffrey Rojas et al. “Surface state engineering of molecule–molecule interactions”. In: *Physical Chemistry Chemical Physics* 14.14 (2012), p. 4971. ISSN: 1463-9076, 1463-9084. DOI: 10.1039/c2cp40254h. URL: <http://xlink.rsc.org/?DOI=c2cp40254h> (visited on 08/29/2018).
- [125] Tanglaw Roman and Axel Groß. “Periodic Density-Functional Calculations on Work-Function Change Induced by Adsorption of Halogens on Cu(111)”. In: *Physical Review Letters* 110.15 (Apr. 12, 2013). ISSN: 0031-9007, 1079-7114. DOI: 10.1103/PhysRevLett.110.156804. URL: <https://link.aps.org/doi/10.1103/PhysRevLett.110.156804> (visited on 08/14/2018).
- [126] Silvan Roth et al. “Chemical Vapor Deposition and Characterization of Aligned and Incommensurate Graphene/Hexagonal Boron Nitride Heterostack on Cu(111)”. In: *Nano Letters* 13.6 (June 12, 2013), pp. 2668–2675. ISSN: 1530-6984, 1530-6992. DOI: 10.1021/nl400815w. URL: <http://pubs.acs.org/doi/abs/10.1021/nl400815w> (visited on 10/28/2014).
- [127] P. Sautet and C. Joachim. “Interpretation of STM images: copper-phthalocyanine on copper”. In: *Surface Science* 271.3 (Jan. 1992), pp. 387–394. ISSN: 00396028. DOI: 10.1016/0039-6028(92)90902-I. URL: <http://linkinghub.elsevier.com/retrieve/pii/003960289290902I> (visited on 07/13/2015).
- [128] *Schematic of qPlus sensor*. 2013. URL: https://en.wikipedia.org/wiki/Non-contact_atomic_force_microscopy#/media/File:QPlusSchematic.svg (visited on 08/10/2018).
- [129] U. Schlickum et al. “Metal-Organic Honeycomb Nanomeshes with Tunable Cavity Size”. In: *Nano Letters* 7.12 (Dec. 1, 2007), pp. 3813–3817. ISSN: 1530-6984. DOI: 10.1021/nl072466m. URL: <http://dx.doi.org/10.1021/nl072466m> (visited on 08/26/2016).
- [130] E Schulz et al. “Engineering solutions for the electropolishing of multi-cell superconducting accelerator structures”. In: (Aug. 2018).
- [131] Fabian Schulz et al. “Elemental Identification by Combining Atomic Force Microscopy and Kelvin Probe Force Microscopy”. In: *ACS Nano* (May 25, 2018). ISSN: 1936-0851, 1936-086X. DOI: 10.1021/acsnano.7b08997. URL: <http://pubs.acs.org/doi/10.1021/acsnano.7b08997> (visited on 06/01/2018).
- [132] Fabian Schulz et al. “Epitaxial hexagonal boron nitride on Ir (111): A work function template”. In: *arXiv preprint arXiv:1404.7371* (2014). URL: <http://arxiv.org/abs/1404.7371> (visited on 10/15/2014).

- [133] Michael Schunack. "Scanning Tunneling Microscopy Studies of Organic Molecules on Metal Surfaces". PhD thesis. Denmark: University of Aarhus. 180 pp.
- [134] Martin Schwarz. "Assembly and Characterization of Hybrid Nanomaterials on Noble Metal Surfaces". PhD thesis. München: Technische Universität München, June 12, 2018. 240 pp. URL: <https://mediatum.ub.tum.de/doc/1436091/1436091.pdf>.
- [135] Martin Schwarz et al. "Corrugation in the Weakly Interacting Hexagonal-BN/Cu(111) System: Structure Determination by Combining Noncontact Atomic Force Microscopy and X-ray Standing Waves". In: *ACS Nano* 11.9 (Sept. 26, 2017), pp. 9151–9161. ISSN: 1936-0851, 1936-086X. DOI: 10.1021/acsnano.7b04022. URL: <http://pubs.acs.org/doi/10.1021/acsnano.7b04022> (visited on 07/20/2018).
- [136] Gene Siegel et al. "Heterogeneous Pyrolysis: A Route for Epitaxial Growth of hBN Atomic Layers on Copper Using Separate Boron and Nitrogen Precursors". In: *Nano Letters* 17.4 (Apr. 12, 2017), pp. 2404–2413. ISSN: 1530-6984, 1530-6992. DOI: 10.1021/acs.nanolett.6b05409. URL: <http://pubs.acs.org/doi/10.1021/acs.nanolett.6b05409> (visited on 08/14/2018).
- [137] K. A. Simonov et al. "Controllable oxidation of h-BN monolayer on Ir(111) studied by core-level spectroscopies". In: *Surface Science* 606.3 (2012), pp. 564–570. ISSN: 0039-6028. DOI: <http://dx.doi.org/10.1016/j.susc.2011.11.031>. URL: <http://www.sciencedirect.com/science/article/pii/S003960281100464X>.
- [138] Matt Stables et al. "Report on the Current Surface Characterisation Research Project for the UKRF Cavity Development Programme". In: (Aug. 2018). URL: https://www.researchgate.net/publication/237827266_Report_on_the_Current_Surface_Characterisation_Research_Project_for_the_UKRF_Cavity_Development_Programme.
- [139] M. Stark et al. "Massive conformational changes during thermally induced self-metalation of 2H-tetrakis-(3,5-di-tert-butyl)-phenylporphyrin on Cu(111)". In: *Chemical Communications* 50.71 (July 14, 2014), p. 10225. ISSN: 1359-7345, 1364-548X. DOI: 10.1039/C4CC03708A. URL: <http://xlink.rsc.org/?DOI=C4CC03708A> (visited on 11/12/2015).
- [140] J. Tersoff. "Role of tip electronic structure in scanning tunneling microscope images". In: *Physical Review B* 41.2 (1990), p. 1235. URL: <http://journals.aps.org/prb/abstract/10.1103/PhysRevB.41.1235> (visited on 07/17/2015).
- [141] J. Tersoff and D. R. Hamann. "Theory of the scanning tunneling microscope". In: *Physical Review B* 31.2 (Jan. 15, 1985), pp. 805–813. ISSN: 0163-1829. DOI: 10.1103/PhysRevB.31.805. URL: <https://link.aps.org/doi/10.1103/PhysRevB.31.805> (visited on 08/23/2018).
- [142] *The Bartynski Group*. 2006. URL: <http://www.physics.rutgers.edu/Bartgroup/STM.htm> (visited on 08/10/2018).
- [143] *The Nobel Prize in Physics 1921*. Jan. 15, 2015. URL: http://www.nobelprize.org/nobel_prizes/physics/laureates/1921/index.html (visited on 01/12/2015).
- [144] M. Topsakal, E. Aktürk, and S. Ciraci. "First-principles study of two- and one-dimensional honeycomb structures of boron nitride". In: *Phys. Rev. B* 79.11 (Mar. 2009), p. 115442. DOI: 10.1103/PhysRevB.79.115442. URL: <http://link.aps.org/doi/10.1103/PhysRevB.79.115442>.

- [145] R. M. Tromp, R. J. Hamers, and J. E. Demuth. “Atomic and electronic contributions to Si (111)-(7x7) scanning-tunneling-microscopy images”. In: *Physical Review B* 34.2 (1986), p. 1388. URL: <http://journals.aps.org/prb/abstract/10.1103/PhysRevB.34.1388> (visited on 07/16/2015).
- [146] D. M. Turley and L. E. Samuels. “The nature of mechanically polished surfaces of copper”. In: *Metallography* 14.4 (1981), pp. 275–294. ISSN: 0026-0800. DOI: [https://doi.org/10.1016/0026-0800\(81\)90001-X](https://doi.org/10.1016/0026-0800(81)90001-X). URL: <http://www.sciencedirect.com/science/article/pii/002608008190001X>.
- [147] José Ignacio Urgel Tendero. “Two-dimensional lanthanide-directed metal-organic networks at surfaces”. PhD thesis. München: Technische Universität München, Dec. 17, 2015. 161 pp. URL: <http://nbn-resolving.de/urn/resolver.pl?urn=nbn:de:bvb:91-diss-20160311-1286634-1-7>.
- [148] Jose I. Urgel et al. “Controlling Coordination Reactions and Assembly on a Cu(111) Supported Boron Nitride Monolayer”. In: *Journal of the American Chemical Society* 137.7 (Feb. 25, 2015), pp. 2420–2423. ISSN: 0002-7863, 1520-5126. DOI: [10.1021/ja511611r](https://doi.org/10.1021/ja511611r). URL: <http://pubs.acs.org/doi/abs/10.1021/ja511611r> (visited on 09/09/2015).
- [149] E. Vander Donckt et al. “Fluorescence of the helicenes”. In: *Chemical Physics Letters* 2.6 (Oct. 1968), pp. 409–410. ISSN: 00092614. DOI: [10.1016/0009-2614\(68\)80041-7](https://doi.org/10.1016/0009-2614(68)80041-7). URL: <http://linkinghub.elsevier.com/retrieve/pii/0009261468800417> (visited on 01/22/2018).
- [150] C. D. Wanger et al. *Handbook of X-ray Photoelectron Spectroscopy*. Vol. 3. Perkin-Elmer Corp., 1979. 190 pp. URL: <http://onlinelibrary.wiley.com/doi/10.1002/sia.740030412/abstract> (visited on 12/15/2014).
- [151] Gregor Wentzel. “Eine Verallgemeinerung der Quantenbedingungen für die Zwecke der Wellenmechanik”. In: *Zeitschrift für Physik* 38.6 (June 1926), pp. 518–529. ISSN: 1434-6001, 1434-601X. DOI: [10.1007/BF01397171](https://doi.org/10.1007/BF01397171). URL: <http://link.springer.com/10.1007/BF01397171> (visited on 08/23/2018).
- [152] Alissa Wiengarten. “Scanning tunneling microscopy investigation of structure and electronic properties of surface-confined tetracyclic species”. PhD thesis. München: Technische Universität München, July 21, 2015. 134 pp. URL: <http://nbn-resolving.de/urn/resolver.pl?urn=nbn:de:bvb:91-diss-20150723-1256606-1-5>.
- [153] Yaping Wu et al. “Effects of thermally-induced changes of Cu grains on domain structure and electrical performance of CVD-grown graphene”. In: *Nanoscale* 8.2 (Dec. 23, 2015), pp. 930–937. ISSN: 2040-3372. DOI: [10.1039/C5NR06195D](https://doi.org/10.1039/C5NR06195D). URL: <http://pubs.rsc.org/en/content/articlelanding/2016/nr/c5nr06195d> (visited on 04/05/2016).
- [154] *X-ray Generation in XPS*. Sept. 21, 2015. URL: http://xpssimplified.com/xray_generation.php (visited on 09/21/2015).
- [155] Takashi Yokoyama et al. “Selective assembly on a surface of supramolecular aggregates with controlled size and shape”. In: *Nature* 413 (Oct. 11, 2001), p. 619. URL: <http://dx.doi.org/10.1038/35098059>.

- [156] Dmitry Y Zemlyanov et al. “Versatile technique for assessing thickness of 2D layered materials by XPS”. In: *Nanotechnology* 29.11 (Mar. 16, 2018), p. 115705. ISSN: 0957-4484, 1361-6528. DOI: 10.1088/1361-6528/aaa6ef. URL: <http://stacks.iop.org/0957-4484/29/i=11/a=115705?key=crossref.c55893e7cb47891c5800779a12eb31ed> (visited on 08/10/2018).
- [157] H. G. Zhang et al. “Assembly of iron phthalocyanine and pentacene molecules on a graphene monolayer grown on Ru(0001)”. In: *Physical Review B* 84.24 (Dec. 19, 2011), p. 245436. DOI: 10.1103/PhysRevB.84.245436. URL: <https://link.aps.org/doi/10.1103/PhysRevB.84.245436> (visited on 05/03/2017).

Appendix

First Backmatter stuff.

Ordered areas Only a single ordered area of TBP on Ag(100) was found, but its structure could not be resolved properly due to tip issues (compare figure 1). Its unit cell looks hexagonal with roughly 1.7 nm period.

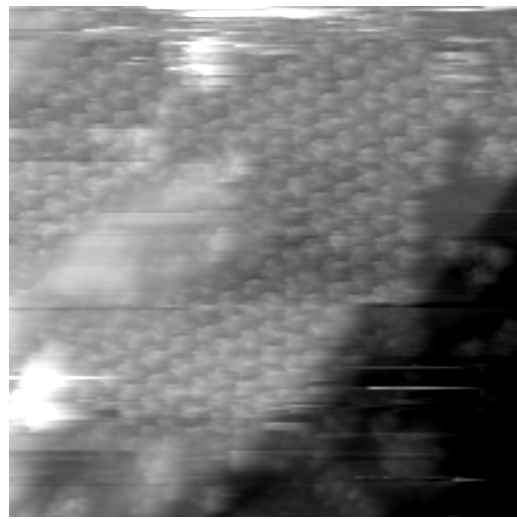


Figure 1: TBP on Ag(100) showing some ordering

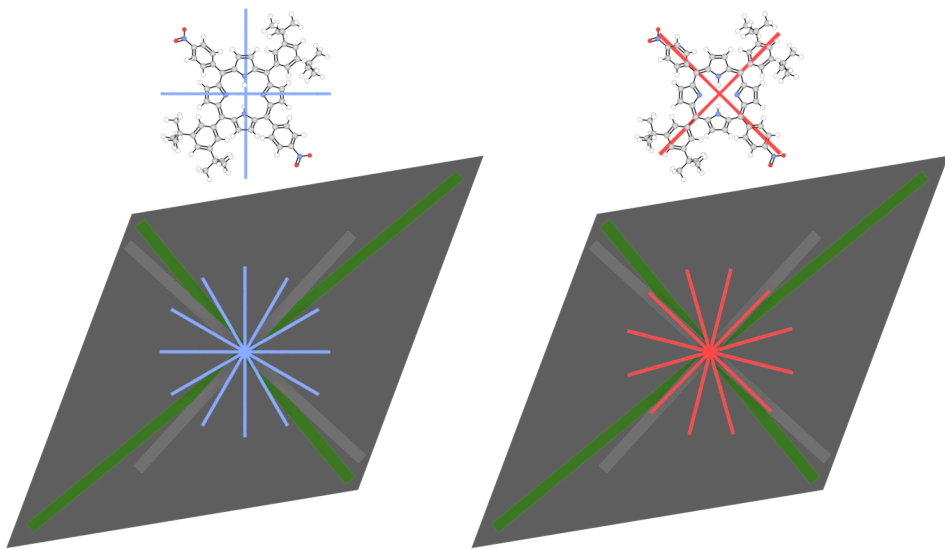


Figure 2: Symmetry relations between TBP molecule and Ag(100) crystal substrate. The same molecular model is highlighted in two different ways, emphasizing the two molecular axis (red/blue). Since the assembly is made up of three different orientations, the three rotated axis sets are shown. The assemblies derived unit cell is shown as shaded background with short and long symmetry axis highlighted in green. The crystal orientation from another preparation on the same single crystal is shown in grey.

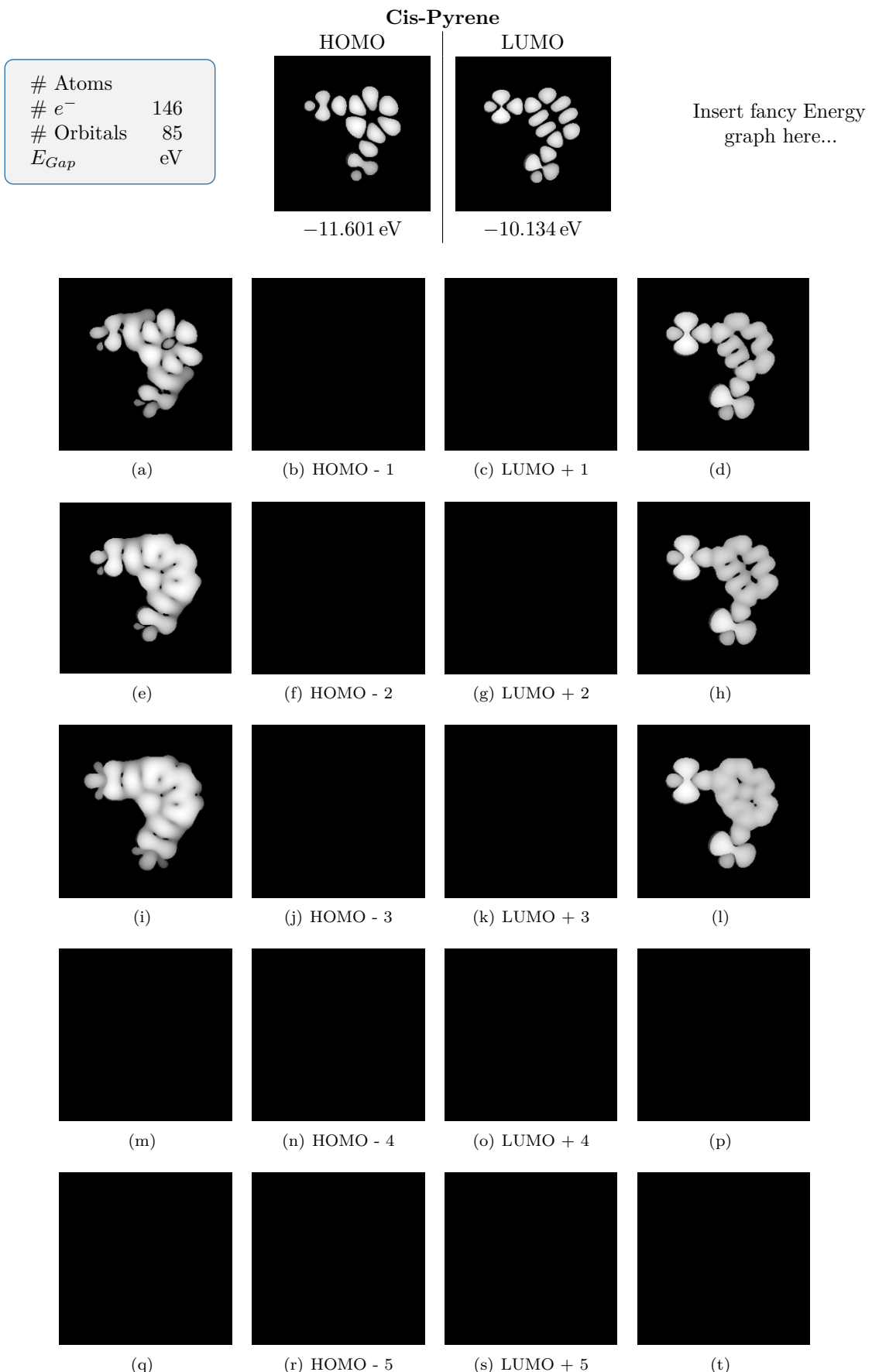


Figure 3: EHT calculated molecular orbitals. HOMO and LUMO states together with five neighboring states (shown in the same column). Inner two columns show HOMO & LUMO states. Outer columns show integration of states as STM image estimation if all states to E_F were contributing equally. Images are 2.5 nm wide

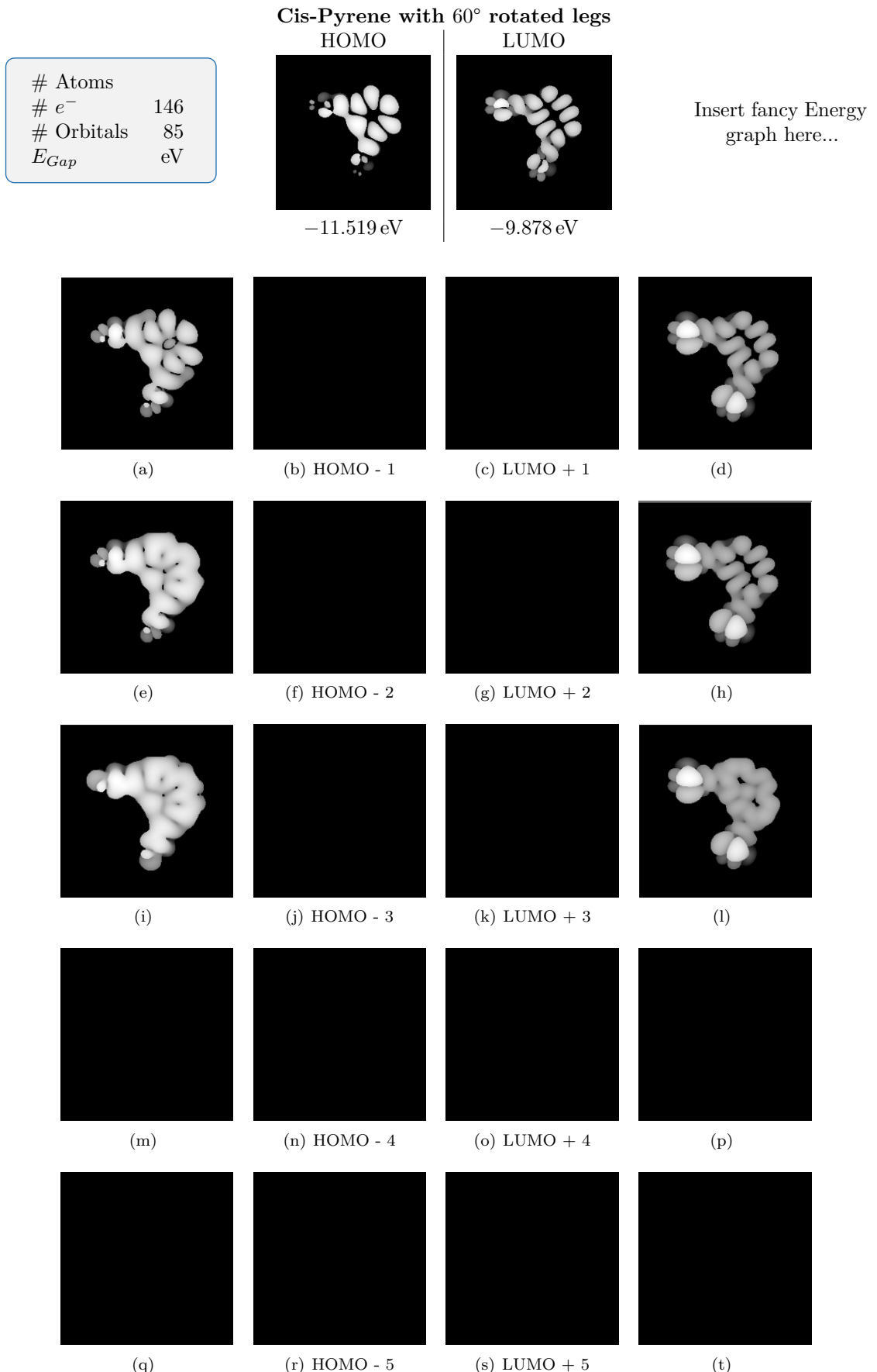


Figure 4: EHT calculated molecular orbitals. HOMO and LUMO states together with five neighboring states (shown in the same column). Inner two columns show HOMO & LUMO states. Outer columns show integration of states as STM image estimation if all states to E_F were contributing equally. Images are 2.5 nm wide

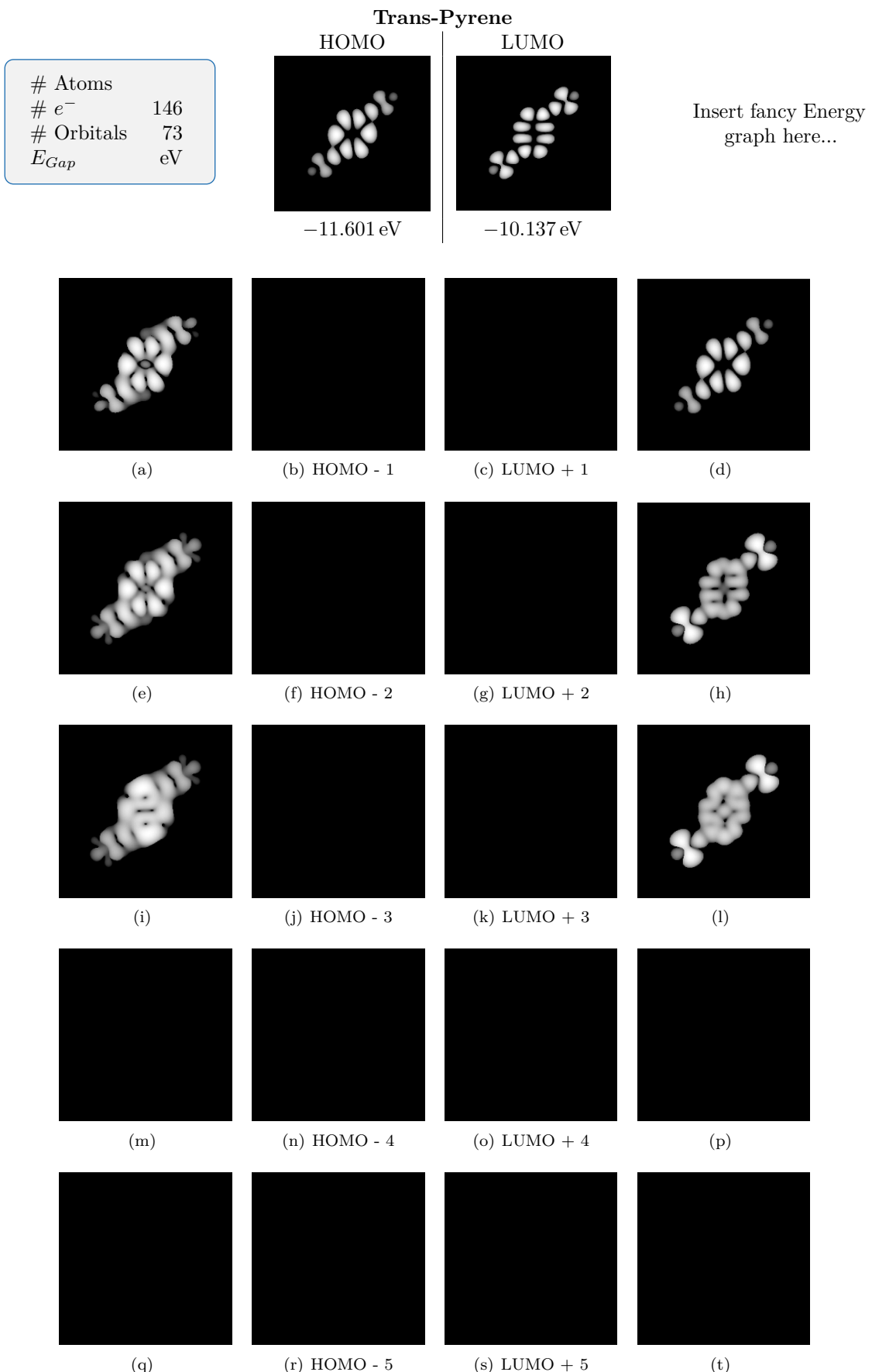


Figure 5: EHT calculated molecular orbitals. HOMO and LUMO states together with five neighboring states (shown in the same column). Inner two columns show HOMO & LUMO states. Outer columns show integration of states as STM image estimation if all states to E_F were contributing equally.

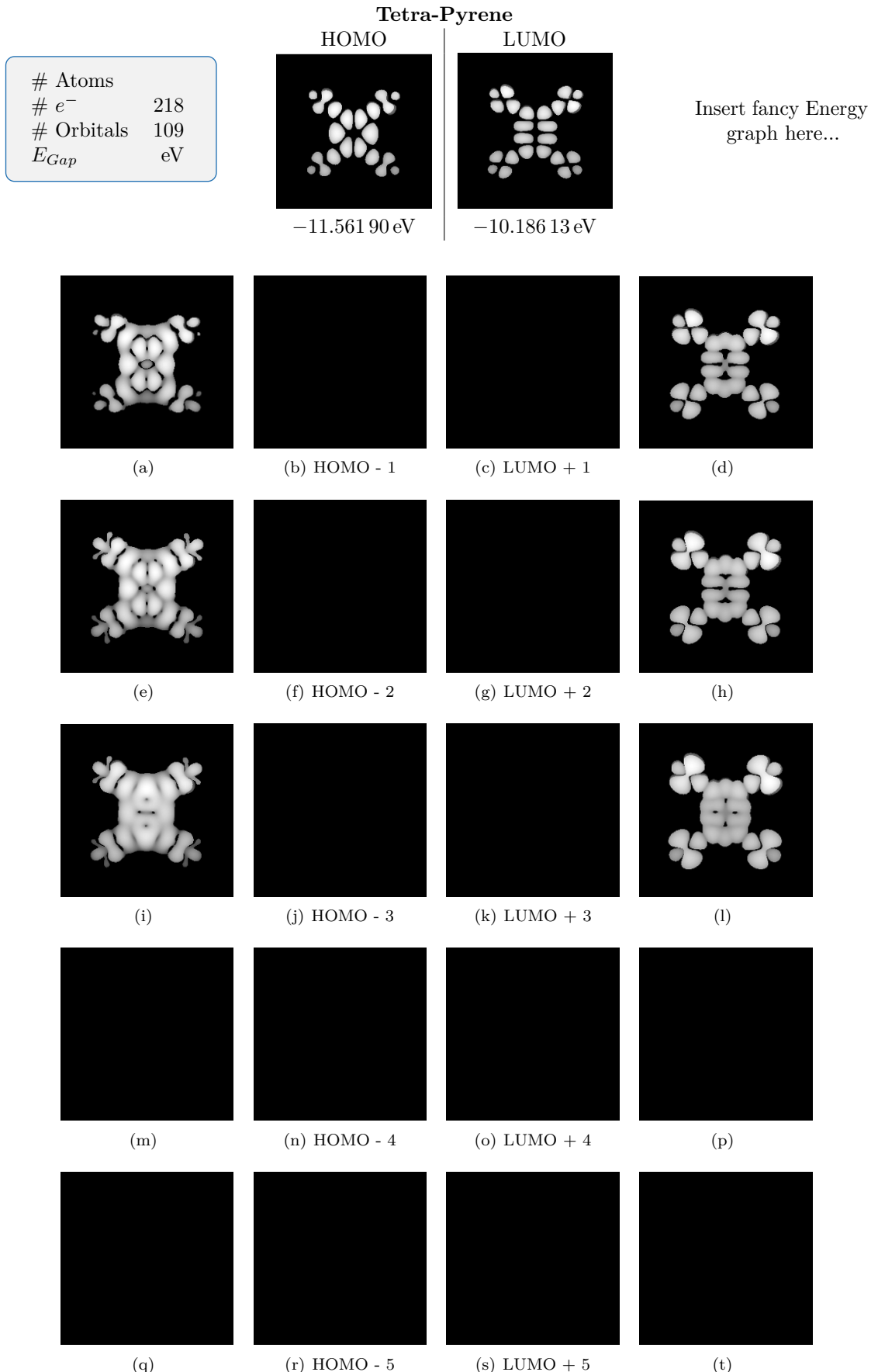


Figure 6: EHT calculated molecular orbitals. HOMO and LUMO states together with five neighboring states (shown in the same column). Inner two columns show HOMO & LUMO states. Outer columns show integration of states as STM image estimation if all states to E_F were contributing equally.